

ABSTRACT

Title of Document: STUDIES OF SPECTRAL MODIFICATION IN
INTENSE LASER PULSE-PLASMA
INTERACTIONS

Wenxi Zhu, Doctor of Philosophy, 2013

Directed By: Professor Thomas M. Antonsen Jr., Physics

Laser pulses propagating through plasma undergo spectral broadening through local energy exchange with driven plasma waves. During propagation, a high power laser pulse drives large amplitude plasma waves, depleting the pulse energy. At the same time, the large amplitude plasma wave provides a dynamic dielectric response that leads to spectral shifting. The loss of laser pulse energy and the approximate conservation of laser pulse action imply that spectral red-shifts accompany the depletion. Here we examine the spectral shift and broadening, energy depletion, and action conservation of nonlinear laser pulses using the modified paraxial solver in WAKE. For pulses causing complete cavitation, large wavenumber shifts and action decay are observed at the distance where 40-50% of the pulse energy is depleted, consistent with theoretical prediction.

A tenuous plasma, enveloped, full wave solver was further implemented and compared to the modified paraxial solver through studying the University of Maryland laser-plasma system. The full wave solver has the advantage of better predicting the dispersion relation and eliminating the problematic divergence in the dispersion of the

modified paraxial solver as wavenumber approaches zero, which is important especially when considering long wavelength generation.

Numerical analysis of the two propagation algorithms has been conducted via monitoring conservation laws. For large spectral shifts, numerical damping and convection of radiation out of the simulation domain result in action decay. Implementing a higher order evaluation of numerical derivatives and smaller spatial step have reduced numerical damping.

Spectral red-shifting of high power laser pulses propagating through underdense plasma channel can be a source of ultrashort mid-infrared (MIR) radiation. Parametric dependence of MIR generation on laser pulse power, initial pulse duration, and plasma density is investigated through characteristic wavenumber estimates and simulations.

STUDIES OF SPECTRAL MODIFICATION IN INTENSE LASER PULSE-
PLASMA INTERACTIONS

By

Wenxi Zhu

Thesis submitted to the Faculty of the Graduate School of the
University of Maryland, College Park, in partial fulfillment
of the requirements for the degree of
Doctor of Philosophy
2013

Advisory Committee:
Professor Thomas M. Antonsen Jr., Chair
Professor Adil B. Hassam
Professor Ki-Yong Kim
Professor Rami A. Kishek
Professor Phillip A. Sprangle

© Copyright by
Wenxi Zhu
2013

Dedication

Dedicated to my parents.

Acknowledgements

For a girl pursuing her PhD and starting a new life in a different country, there are so many people she wants to thank to.

I appreciate my parents for always giving me a strong support on pursuing what I like. We haven't seen each other for years, but we talk regularly on the phone. They always encourage me and help me out of any difficulty or confusion. It is always a comfort to know that there is an unconditional support, and there is home. I appreciate for their patience and time. They are always my friends and tutors.

I appreciate Dr. Antonsen for helping, advising and inspiring me a lot. It seems that I can always learn something from him by talking with him. He is the person that I respect and admire a lot since I took his electrodynamics class in my second year of graduate school. He can always explain things in an easy and clear way, even for a difficult Jackson's problem. And his intelligence and experience make him come up with ideas quickly. During some of our discussions of theoretical problems, there were many times that we got stuck, then he stood up and went outside for a little while, and he always came back soon with a solution. It has been a magic to me.

Like other professors in physics, I can feel his passion for science. From taking the classes and talking with him, I can feel how much he likes his work. He told me a few times that he couldn't sleep well during the night because he was bothered by research problems. That has had a great impact on me, because sometimes I got frustrated from work, even from my life, and I had even thought of giving up, but Dr. Antonsen's interest and passion in science reminded me of my original strong interest and determination in

studying physics. He is a mentor who not only teaches me physics, but also teaches me how to move on in a complicated situation.

I appreciate John for his great help on my project research in the field of laser and plasma physics. My research work might take much longer if without his help. He taught me a lot and corrected the wrong way I did in my research from time to time. I didn't know anything about MATLAB when I started my project. He taught me many details of using MATLAB, as well as WAKE. I even improved a lot of my written and spoken English through discussing with him. I am grateful to him for spending a lot of time helping me.

I want to thank Dr. Gregory Nusinovich for his help on my first project on microcrack study in the field of accelerator physics. For the first half year of my graduate research, he guided me on to the track of scientific research. I can always ask him about references because he knows a lot in his field and could memorize a lot of references, like a live 'Wiki'. He is strict in work but very kind and approachable in life.

I appreciate the committee professors: Dr. Thomas Antonsen, Dr. Adil Hassam, Dr. Ki-Yong Kim, Dr. Rami Kishek and Dr. Phillip Sprangle (alphabetically) for being so kind to spend their precious hours to listen to my PhD work.

I would like to thank Luke, Thomas, Chenlong, Tak Chu, Andy, Dmytro and Oleksandr for the precious months and years we spent together in AVW 3326 and ERF 1202C. I will never forget our group BBQs.

I want to thank all other of my friends for bringing such colorful life to me in Maryland.

I want to thank UMD and especially physics department and IREAP. They not only gave me admission to study for my degree, but also provided excellent education and excellent academic environment, with so many brilliant professors and scientists dedicated to their work and so many smart people I can learn from. It is an unforgettable land for me to start to be independent and be strong.

Table of Contents

Dedication	ii
Acknowledgements	iii
Table of Contents	vi
List of Tables	viii
List of Figures	ix
Chapter1: Introduction	1
1.1 Optical Guiding in the Laser Wakefield Accelerators (LWFA) and Spectral Modification in the Plasma Channels	1
1.1.1 The Laser Wakefield Accelerators (LWFA) and recent progress.....	1
1.1.2 Plasma Wave Driver: the Ponderomotive Force.....	2
1.1.3 Laser Guiding.....	4
1.1.4 Spectral Modification.....	4
1.1.5 Mid-Infrared Generation from Spectral Broadening	5
1.2 Models and Numerical Approaches	6
1.2.1 The Particle-in-Cell (PIC) Method	6
1.2.2 The Quasistatic Approximation (QSA) and Envelope Approximation	6
1.2.3 The Enveloped Full Wave Equation (FWE) and the Modified Paraxial Equation (MPE)	8
1.2.4 Numerical Implementation of PIC Simulations.....	11
1.2.5 The Code WAKE.....	13
1.3 Structure of the Thesis	13
Chapter 2: The Enveloped Wave Equation and Observation of Spectral Modifications in the Laser Wakefield Simulations	15
2.1 Introduction.....	15
2.2 Spectral Modification and Its Simulation Model in WAKE.....	17
2.3 Simulations	23
2.3.1. 2006 LBNL Experiments	24
2.3.2. Pulse Compression Experiments.....	26
2.3.3. 1D Regime Simulations	27
2.4 Conclusion	28
Chapter 3: Analysis of Conservation Laws and the Numerical Schemes in WAKE.....	43
3.1 Introduction.....	43
3.2 Full Wave Equation (FWE) and Modified Paraxial Equation (MPE)	44
3.2.1 Numerical dispersion relations and laser pulse group velocities from FWE and MPE	44
3.2.2 Conservation laws of FWE and MPE	46

3.3 Simulations and Comparison of FWE and MPE using UMD Parameters	47
3.4 Analysis of the Numerical Scheme in WAKE and Non-Conservation of Action ..	48
3.4.1. Numerical Scheme for MPE with Three-Point Fitting and Action Decay	48
3.4.2. Numerical Scheme for FWE with Higher-Order-Fitting and Action Decay ..	53
3.4.3. Conclusions of Numerical Schemes and Action Decay	55
3.5 Conclusions	55
3.6 Appendix 1: Conservation Laws.....	56
3.7 Appendix 2: Four-Point-Fitting Scheme.....	57
Chapter4: Pulsed Mid-infrared Radiation from Spectral Broadening in Laser Wakefield Simulations.....	73
4.1 Introduction.....	73
4.2 Plasma Response and Propagation Model	75
4.3 Spectral Shifting in Tenuous Plasma	76
4.4 Simulation Results	79
4.4.1. Observation of MIR	79
4.4.2. Parametric Dependence of MIR Energy Generation	80
4.5 Conclusions	83
4.6 Appendix: Scaling of the Characteristic Wavenumber Shift.....	83
Chapter5: Summaries	95
Bibliography.....	97

List of Tables

Table 2.1 Parameters for the three cases simulated.

Table 3.1 UMD laser-plasma system parameters.

List of Figures

Figure 2.1 Laser pulse of duration τ_p travelling through a plasma to the left. Plasma density n increases at the front of the pulse, decreases in the middle and increases again at the back, resulting blue shift, red shift and blue shift again from front to back.

Figure 2.2 Comparison of actual group velocity (red) and the approximate group velocity (blue) as functions of k_z . Plasma wave numbers in two propagation directions are denoted by dashed lines.

Figure 2.3 Local spectral shift δk falls into the weak $|\delta k| \sim k_p$, marginal $|\delta k + k_0| \gg k_p$ and strong $|\delta k + k_0| \sim k_p$ ranges.

Figure 2.4 (a) Radially averaged pulse intensity profile as a function of (z, ξ) for continuous propagation distance $z=0-12\text{mm}$. (b) Pulse intensities as functions of ξ at distances $z=0$ (red), 2.4 (light blue), 3.6 (purple) and 4.8mm (blue). $k_0\Delta\xi = 0.16$ and $\omega_p\Delta t = 0.18$ were applied in WAKE; running time 100 hrs, 1 cpu.

Figure 2.5 Energy (red) and action (green) as functions of propagation distance z . Four moments of interest are denoted by dashed lines: $z=0, 2.4, 3.6$ and 4.8mm .

Figure 2.6 (a)-(e) Densities in the (r, ξ) frame at $z=0, 2.4, 3.6, 4.8$ and 8mm from left to right. (f)-(j) Wigner distributions as a function of (k, ξ) at $z=0, 2.4, 3.6, 4.8$ and 8mm from left to right.

Figure 2.7 (a) Spectral intensity as a function of (z, k) for continuous distance $z=0-12\text{mm}$. (b) Spectral intensities at distances $z=0$ (red), 2.4 (light blue), 3.6 (purple) and 4.8mm (blue).

Figure 2.8 (a) Local frequency shift as a function of (z, ξ) for distance $z=0-12\text{mm}$. (b) Local frequency shifts as functions of ξ at distances $z=0$ (red), 2.4 (light blue), 3.6 (purple) and 4.8mm (blue).

Figure 2.9 (a) Pulse profiles and the Wigner distributions at the background for four experimental cases: gas jet lengths $l=0, 4, 6$ and 8.5 mm from left to right. (b) Energy ratio (red, left axis) and relative action change (green, right axis) as functions jet length l from WAKE. (c) Pulse intensity as a function of (l, ξ) in continuous distance $l=0- 8.5$ mm from WAKE. (d) Pulse profiles for four jet lengths $l=0$ (red), 4 (light blue), 6 (purple) and 8.5 mm (blue) from WAKE.

Figure 2.10 (a) is the pulse field intensity as a function of $(\omega_p t, \xi)$, averaged over r ; (b) is the spectrum intensity as a function of $(\omega_p t, k/k_0)$, integrated over r . $k_0 \Delta \xi = 0.14$, $\omega_p \Delta t = 0.2$ were applied, propagation time $\omega_p t = 4000$.

Figure 2.11 (a) Laser energy E (red, left axis), the mean wavenumber $\langle k \rangle$ computed from the first moment of the laser vector potential (blue, left axis), and the relative change in the wave action W (green, right axis) from the 1D explicit simulation. (b) Energy E (red, right axis) and action W (green, right axis) from the WAKE simulation. $k_0 \Delta \xi = 0.14$, $\omega_p \Delta t = 0.2$ were applied and propagation time $\omega_p t = 4000$.

Figure 2.12 Wigner distributions as functions of $(k/k_0, \xi)$ at propagation time $\omega_p t = 0, 2270, 3000$ from left to right.

Figure 3.1 Normalized frequency, $\omega/k_0 c$, as a function of normalized wavenumber k/k_0 from theory (black) and the MPE solver (red) and FWE solver (blue) with a resolution $k_0 \Delta \xi = 0.28$ and a time step $\omega_p \Delta t = 0.54$. Here we have taken $\omega_p = 1.17 \times 10^{14} \text{ rad/s}$, $k_0 = 7.8 \times 10^4 \text{ rad/cm}$ and $k_{\perp} = 8 \times 10^2 \text{ rad/cm}$.

Figure 3.2 Comparison of group velocity v_g as a function of normalized wavenumber k/k_0 from theory (black) and the MPE solver (red) and FWE solver (blue) with a resolution $k_0 \Delta \xi = 0.28$ and a time step $\omega_p \Delta t = 0.54$. Here we have taken $\omega_p = 1.17 \times 10^{14} \text{ rad/s}$, $k_0 = 7.8 \times 10^4 \text{ rad/cm}$ and $k_{\perp} = 8 \times 10^2 \text{ rad/cm}$.

Figure 3.3 Radially averaged laser fields as a function of propagation time or distance z and ξ from FWE (a) and MPE (b) models respectively.

Figure 3.4 (a) Pulse intensities as functions of ξ at distances $z=0$ (red), 3.7 (purple), 5.5 (blue), 7.4 (green) and 8.6mm (orange). $k_0\Delta\xi = 0.14$ and $\omega_p\Delta t = 0.09$ were applied in WAKE; running time 1.5 hrs, 1 cpu. (b) Radially averaged pulse intensity profile as a function of (z, ξ) for continuous propagation distance $z=0-12.3$ mm.

Figure 3.5 (a) Spectral intensity as a function of (z, k) for continuous distance $z=0-12.3$ mm from the full wave equation (FWE). (b) Spectral intensity from modified paraxial equation (MPE). (c) Spectral intensity Turbowave (2D planar geometry).

Figure 3.6 (a)-(e) Pulse profiles as a function of (r, ξ) at $z=0, 3.7, 5.5, 7.4$ and 8.6 mm. from left to right.

Figure 3.7 (a)-(e) Wigner distributions as a function of (k, ξ) at $z=0, 3.7, 5.5, 7.4$ and 8.6 mm. from left to right.

Figure 3.8 Energy (red for FWE, purple for MPE) and action (dark green for FWE and light green for MPE) as functions of propagation distance z .

Figure 3.9 δk_r (a) and δk_i (b) of the ‘numerical operator’ $\hat{\delta k}$ as functions of $\delta k / k_0$, for both red shifts $\delta k / k_0 < 0$ and blue shifts $\delta k / k_0 > 0$. The orange curves represent the case $k_0\Delta\xi = 0.56$, reds represent $k_0\Delta\xi = 0.28$, blues represent $k_0\Delta\xi = 0.14$, and blacks represent $k_0\Delta\xi = 0.07$.

Figure 3.10 (a) $|\lambda|^n = |e^{-i\delta\omega\Delta t}|^n$ as a function of $\delta k/k_0$ with $1/k_0 c\Delta t = 0.25$ but different values of $\Delta\xi$ denoted by different colors for both red shift $\delta k/k_0 < 0$ and blue shift $\delta k/k_0 > 0$. The orange curve is for the case $k_0\Delta\xi = 0.56$, red is $k_0\Delta\xi = 0.28$, blue is $k_0\Delta\xi = 0.14$, and black is $k_0\Delta\xi = 0.07$. (b) Action versus time produced by WAKE with $k_0\Delta\xi = 0.28$ (red) and $k_0\Delta\xi = 0.14$ (blue) simulating the 1D explicit simulation case.

Figure 3.11 (a) $|A_N/A_0|^2$ as a function of $\delta k/k_0$ with $1/k_0 c\Delta t = 0.028$ but different values of $\Delta\xi$ denoted by different colors for both red shift $\delta k/k_0 < 0$ and blue shift $\delta k/k_0 > 0$. The orange curve is for the case $k_0\Delta\xi = 0.56$, red is $k_0\Delta\xi = 0.28$, blue is $k_0\Delta\xi = 0.14$, and black is $k_0\Delta\xi = 0.07$. (b) Action versus time produced by WAKE with $k_0\Delta\xi = 0.28$ (red) and $k_0\Delta\xi = 0.14$ (blue) simulating the UMD laser-plasma system.

Figure 3.12 (a) $|A_N/A_0|^2$ as a function of $\delta k/k_0$ with $1/k_0 c\Delta t = 0.028$ and $k_0\Delta\xi = 0.14$ for 3-point fitting method (dashed curve) and 4-point fitting method (solid curve). (b) Action versus time produced by WAKE with $k_0\Delta\xi = 0.14$ for 3-point and 4-point fitting methods simulating the UMD laser-plasma system.

Figure 4.1 Top: laser intensity and electron density as functions of channel radius r and ξ at propagation distances of $z = 0.0$, left, and 4.9 mm, right. Bottom: Wigner distributions

of the laser pulse as a function of normalized wavenumber and ξ at the same propagation distances.

Figure 4.2 Characteristic wavenumber $\langle k \rangle / k_0$ as a function of distance z for initial pulse powers of 17, 40 and 60 TW, represented by red, blue and black respectively. The inset shows a comparison with linear theory (dashed lines) for each case.

Figure 4.3 Spectral energy density of a pulse propagating in a plasma channel as a function of k/k_0 at distances $z=0, 2.5, 4.9$ and 7.9 mm, represented by the red, grey, dark grey and black lines respectively; spectral energy density for a pulse propagating through a uniform plasma (no channel) is represented by the blue curve. The red arrow indicates where $\lambda=4.7 \mu\text{m}$.

Figure 4.4 Cumulative energy as a function of k/k_0 at distances $z=0, 2.5, 4.9$ and 7.9 mm, represented by the red, grey, dark grey and black curves respectively; cumulative energy for the no channel case at $z=7.9$ mm represented by the blue curve. The red arrow indicates there are 15mJ of cumulative energy at $\lambda=4.7 \mu\text{m}$.

Figure 4.5 (a) Retrieved profile of the filtered mid-ir pulse ($0 < k < 0.2k_0$) radially averaged intensity as a function of (z, ξ) . (b)(c) Filtered mid-ir pulse ($0 < k < 0.2k_0$) as a function of (r, ξ) at distances $z=7.9$ and 8.4 mm.

Figure 4.6 (a) Cumulative energy at largest characteristic wavenumber shift as a function of k/k_0 for initial powers $P=40\text{TW}$ for the channeled (black, solid) and non-channeled (black, dashed) cases and 17TW for the channeled (grey, solid) and non-channeled (grey, dashed) cases. (b) Mid-ir generation efficiency as a function of initial pulse power for $\lambda \geq 6 \mu\text{m}$, $\lambda \geq 4 \mu\text{m}$ and $\lambda \geq 2 \mu\text{m}$.

Figure 4.7 MIR conversion efficiency in the ranges $\lambda \geq 6\mu\text{m}$, $\lambda \geq 4\mu\text{m}$ and $\lambda \geq 2\mu\text{m}$ as a function of initial temporal FWHM. The upper and lower dashed lines show the effect of negative and positive chirp respectively.

Figure 4.8 MIR conversion efficiency in the ranges $\lambda \geq 6 \mu\text{m}$, $\lambda \geq 4 \mu\text{m}$ and $\lambda \geq 2 \mu\text{m}$ as a function of on-axis plasma density.

Figure 4.9 Fractional difference in cumulative energies resulting from FWE and MPE approaches $((U_{\text{cFWE}} - U_{\text{cMPE}})/U_{\text{cFWE}})$ as a function of k/k_0 for a 30fs, 40 TW pulse propagating in a plasma channel.

Chapter 1: Introduction

1.1 Optical Guiding in the Laser Wakefield Accelerators (LWFA) and Spectral Modification in the Plasma Channels

Recent advances in Laser Wakefield Acceleration (LWFA) [1] have stimulated the study of ultra intense laser pulse propagation in plasmas. In LWFA, which is just one type of plasma based particle accelerator, a single, short ($\leq 1ps$), high intensity ($\geq 10^{17}W/cm^2$) laser pulse propagates through an underdense plasma exciting plasma waves. Charged particles are then accelerated in the electric field of the plasma waves [1-3]. The acceleration process is most effective when the laser intensity is high and the plasma is strongly perturbed. There are then numerous nonlinear processes affecting the laser propagation. These include: pulse compression, self-focusing, pulse refraction, spectral broadening and shifting, pump depletion and plasma cavitation. This thesis will explore these effects with an emphasis on modeling and understanding the evolution of the pulse spectrum.

1.1.1 The Laser Wakefield Accelerators (LWFA) and recent progress

Laser Wakefield Accelerator is considered as an option for the next generation of accelerators because it can produce large accelerating gradients 1GV/cm which are far in excess of that produced in conventional accelerators. In conventional accelerators the maximum accelerating gradient is limited to the range 20MV/m due to breakdown on the metal structure. In a LWFA the accelerating medium is plasma, which is already broken down.

Recent experiments in LWFAs [4] have made great progress and have demonstrated a promising way to build high energy colliders with compact size and less cost [5-7]. Initial experiments in the so called self modulated regime were performed by A. Modena et al. in 1995. Self modulation is a process in which a single long laser pulse breaks up into a train of short

pulses with duration approximately the same as the plasma period. This drives large amplitude plasma waves and the accelerating energy gain achieved in 1995 experiment was in the range of 100 MeV. But, the beam quality was poor in this case in that the spread in energy was comparable to the mean energy.

More recent progress in experiments has used high intensity shorter pulses (50 fs). Because the pulse duration was matched to the plasma period and because the pulse intensity was higher than in previous experiments, a regime was entered in which the electron plasma was cavitating following the laser pulse. This is often referred to as the blow-out, caviation, or bubble regime [8-10]. In this regime, a portion of plasma electrons can be trapped and accelerated to high energy. In the experiments this produced nearly monoenergetic electron beams [11-17].

Recently, there has been more exciting progress in experiments. A significant achievement is 1 GeV energy gain within a centimeter-scale distance at the Lawrence Berkeley National Lab (LBNL) in 2006 [18,19]. This was followed by more recent accomplishments of > 2Gev energy gain using the Texas Pettawatt laser and > 3GeV energy gain from GIST, Korea [20]. With such high electric gradient the plasma acceleration field can be several orders of magnitude stronger than that of conventional radio-frequency (RF) accelerators (10~20MV/m).

Many recent efforts of improving beam quality have been focused on methods of initial trapping of electrons from the background plasmas in the plasma waves and triggered trapping and injection of electron beams [21]. New facilities for the next generation of experiment are under construction such as CILEX [22] and BELLA [23].

1.1.2 Plasma Wave Driver: the Ponderomotive Force

During the laser pulse propagation, the electrons interact with the radiation electric fields in two ways. They quiver at the high frequency of the laser field, and then respond on the time scale of the plasma waves to the low frequency ponderomotive potential [24-26]. Through this low frequency force the plasma wake fields are generated.

To understand the origin of the ponderomotive force, consider the plasma (electron) fluid momentum equation of motion

$$\frac{d\vec{p}}{dt} = -e(\vec{E} + \frac{\vec{v} \times \vec{B}}{c}), \quad (1.1)$$

where e , \vec{v} and \vec{p} are the charge, velocity and momentum of a particle, $\vec{E} = -\partial\vec{A}/c\partial t$ and $\vec{B} = \vec{\nabla} \times \vec{A}$ are electric and magnetic fields of the laser.

In the weak field limit, the momentum can be written as the sum of a rapidly oscillating response to the laser electric force \vec{p}_q and a slowly varying response $\delta\vec{p}$ that is second order in the laser field, $\vec{p} = \vec{p}_q + \delta\vec{p}$. The rapidly varying component satisfies

$$\partial\vec{p}_q / \partial t = -e\vec{E}. \quad (1.2)$$

And introducing the vector potential is found to satisfy $\vec{p}_q = e\vec{A}/c$. The second order momentum is determined by

$$\begin{aligned} d\delta\vec{p} / dt &= -[(\vec{p}_q / m) \cdot \nabla] \vec{p}_q - \vec{p}_q \times (c\nabla \times \vec{a}) \\ &= -mc^2 \nabla |\vec{a}|^2 / 2 \end{aligned}, \quad (1.3)$$

where $\vec{a} = e\vec{A}/mc^2 = \vec{p}_q/mc$ is the dimensionless vector potential. Generally the weak field limit is defined by $|\vec{a}| \ll 1$. The ponderomotive force is the time average of the right hand side of (1.3), and is related to gradient of the laser pulse intensity,

$$\vec{F}_p = -mc^2 \nabla \langle |\vec{a}|^2 \rangle_t / 2 \sim -\nabla I, \quad (1.4)$$

where $\langle \rangle_t$ denotes the time average. In the strong field limit when particles are relativistic, the ponderomotive force takes the form [26]

$$\vec{F}_{pr} = -(mc^2/\bar{\gamma}) \nabla \langle |\vec{a}|^2 \rangle_t / 2, \quad (1.5)$$

where $\bar{\gamma} = [1 + (\langle |\vec{p} \rangle_t|^2 / m^2 c^2 + \langle |\vec{a}|^2 \rangle_t)]^{1/2}$ is the time averaged relativistic factor and $\langle |\vec{p} \rangle_t$ is the momentum averaged over time.

1.1.3 Laser Guiding

To extend the interaction length, laser pulse guiding is desired. Guiding requires a high index of refraction on axis than off axis. The laser pulse can be guided in two different ways. The pulse can be self-guided due to the relativistic decrease in quiver velocity with intensities increased. The critical power for relativistic self-guiding is $P_c = 17(\omega / \omega_p)^2 GW$, where ω_p is the plasma frequency. At higher powers, $P > P_c$, the pulse creates its own guiding structure by radially expelling electrons and varying the index of refraction [4,27-30]. At lower powers, $P < P_c$, pre-formed plasma channels with lower density on axis than off can guide the laser pulse [31-33].

A typical set up that is mainly considered in our study is the utilization of a Ti-Sapphire ($\lambda = 800$ nm) to generate ultrashort pulses (FWHM > 20 fs) [34]. The ultrashort pulse is amplified using chirped pulse amplification (CPA) in which the pulse is stretched out temporally before amplification and compressed back after being amplified to reach to a high peak power pulse with the same pulse duration as the original one [35,36]. The plasma structure used in this study is a cylindrical symmetric guiding channel usually filled with pre-ionized Helium or Nitrogen (or a combination of the two) or Argon. The plasma density varies parabolically with radius $n = n_0(1 + r^2 / r_{ch}^2)$, where r_{ch} parameterizes the channel radius. The laser spot size w is ‘matched’ to the channel $w = \sqrt[4]{8} \sqrt{r_{ch} c / \omega_p}$ so that it is properly guided. We have studied different initial laser pulse power cases in the context of this thesis, so that different extent of nonlinear behavior of the pulse and the corresponding spectral evolution can be studied.

1.1.4 Spectral Modification

The nonlinear process of plasma wave excitation leads to modification of the laser pulse spectrum [37-39]. The laser pulse drives a plasma wave through the ponderomotive force.

Plasma electrons are pushed forward at the pulse front, repelled laterally in the body of the pulse, and converge on axis one plasma period later. As a result, the electron density increases at the front, decreases in the middle and can increase again at the back of the pulse. The temporal density variations of the plasma wave provide a dynamic dielectric response that modifies the pulse spectrum [38,40-42]: the spectrum blue-shifts where the electron density rises in time and red-shifts where the electron density falls in time. Both red and blue shifts of the pulse were observed in previous studies [43-46]. For pulse durations commensurate with the plasma period, red-shifting dominates the spectral evolution as the body of the pulse sits in a region of falling electron density. As we will see, it is expected, based on conservation of wave action (to be defined), that the laser pulse frequency will be down shifted by an amount comparable to the initial frequency as the laser pulse loses energy comparable to its initial energy.

1.1.5 Mid-Infrared Generation from Spectral Broadening

The red-shifting can lead to a broadband spectrum extending well into the mid-infrared (MIR), wavelengths ranging from 2 to 20 microns, and whose properties are determined by those of the initial pulse and the plasma through which it propagates [47]. The extent of spectral shifting depends on the temporal gradient in the electron density and the distance over which the gradient is sustained. The conversion to MIR thus relies critically on increasing and maintaining the ponderomotive force [24-26].

Because of the spectral proximity of MIR to the natural frequencies associated with many important molecular vibrational transitions and two atmospheric transmission windows of 3-5 μm and 8-13 μm , a tunable MIR source could be applied to probe fundamental physical processes in liquids and materials or induce time-dependent structural changes in biological assemblies [47,48]. We investigate the generation of MIR from our simulations and investigation of parametric dependence of conversion from optical to MIR energy in underdense plasmas in Chap.4.

1.2 Models and Numerical Approaches

1.2.1 The Particle-in-Cell (PIC) Method

Theoretical study of laser pulse spectral evolution requires physical models that self-consistently treat the propagation of the pulse, and the excitation of plasma waves. One of the most comprehensive simulation approaches is the Particle-in-Cell (PIC) method [49,50]. The PIC method treats electrons and ions as individual particles that move through the simulation domain according to the relativistic equations of motion, Eq. (1.1). Particles interact with electromagnetic fields self-consistently. Quantities such as particle charge and current densities are accumulated on a grid, based on the position and velocities of the simulation particles, and serve as sources in the full system of Maxwell's equations. Typically the number of simulation particles is much less than the actual number of particles. Thus, when computing charge and current densities, each simulation particle (or macro particle) represents a number of actual particles.

The PIC approach resolves all time scales down to the laser period, and thus is computationally expensive [39,51-54]. Parallel programming tools have been developed for the demanding computation needs of PIC simulations [55,56]. Further, a more efficient many-core architecture: Graphic Processing Units has evolved for the general-purpose parallel programming, in which memory is shared by thousands of concurrent threads [57,58]. The fully explicit, multi-dimensional and relativistic PIC code OSIRIS [59-61], Vorpil [62] and a more recent 'jasmine' [63] have implemented the GPU architecture.

1.2.2 The Quasistatic Approximation (QSA) and Envelope Approximation

While the comprehensive approach solves the full system of Maxwell's equations on all time scales, there are techniques that have been developed to speed up simulations of the laser-driven and plasma-driven accelerators by many orders of magnitude. Due to the disparity of the length scales between laser wavelength and plasma wavelength, reduced models such as the

Lorentz-boosted Frame method [64] and the Ponderomotive Guiding Center method [65,66] are used to speed up calculations.

The Lorentz boosted frame method solves the full set of Maxwell's equations and the relativistic equations of motion in a reference frame moving with respect to the plasma in which the Lorentz shifted plasma and laser frequencies are comparable. The ponderomotive guiding center method uses the separation of motion described by Eqs. (1.1-1.5).

The quasistatic approximation (QSA) is often associated with the Ponderomotive Guiding Center method [26]. It assumes that the laser deformation and its wakefield variation is very small during the time in which a plasma particle transits through the laser pulse. That is, the laser pulse duration is much smaller than the pulse evolution time [67]. This allows separation of timescales of the electromagnetic field of the driver determined by Maxwell's equations and the evolution of plasma particles determined by the equation of motion with the ponderomotive force. Larger time steps are applied to solve the evolution of the electromagnetic fields of the laser and numerical efficiency is achieved. The quasistatic approximation only applies to low energy particles, which are not fast enough to be travelling with the laser pulse. For particles that are trapped, accelerated and travelling with the speed comparable to the speed of light, QSA breaks down. In the study of this thesis, we only consider the lower energy particles, i.e. those that are not trapped and accelerated. Our study will be based on numerical simulations using the 2D QSA code WAKE [26], which is described later in this chapter. Quick-PIC is a 3D PIC code that also applies QSA to model particle or laser beam driven wakefield acceleration [68].

Because of the separation of time scales, electrons respond to the pulse in two different ways as mentioned earlier: there is a high frequency response giving rise to currents that modify the laser pulse and low frequency response through the ponderomotive force driving the plasma waves. The plasma period and pulse duration are assumed to be comparable. For this separation of time scales to be valid, it is required that the plasma be tenuous, $\omega_p^2 \ll \omega_0^2$, where ω_p is the

plasma frequency $\omega_p = (4\pi q^2 n / m)^{1/2}$ with n being the plasma density, and q being the charge of the plasma particle. The contribution of the plasma to the dielectric constant is thus small, so that the shape of the laser pulse evolves slowly as it propagates.

There are further approximations that lead to greater numerical efficiency. A common approach, motivated by the slow variation of the pulse shape together with the separation in time scales between the laser oscillation period and the plasma wave period and laser pulse duration, is to treat the laser pulse in the envelope approximation. The time structure of the laser pulse can be separated into high frequency oscillations within the pulse modulated by a slowly varying envelope. The plasma motion can be separated into a rapid quiver motion and a slowly varying ponderomotive motion as discussed previously. The plasma density responds to the ponderomotive force, which depends only on the pulse envelope. In this case it is not necessary to resolve the laser period or wavelength.

A common representation of the laser vector potential field \vec{A} for a linearly polarized wave is to write the transverse component as an envelope \hat{A}_\perp modulating a plane wave traveling at the speed of light [26]

$$\tilde{A}_\perp = \hat{A}_\perp(\vec{x}_\perp, \xi, t) e^{-ik_0 \xi} + c.c., \quad (1.6)$$

where $k_0 = \omega_0 / c$ is the laser central wave number, and in a moving window $(\vec{x}_\perp, \xi = ct - z, t)$ system \vec{x}_\perp represents the transverse direction, $\xi = ct - z$ measures the distance back from the head of the pulse. In this approach, changes in the laser frequency are manifested in more rapid variations of the laser pulse envelope.

1.2.3 The Enveloped Full Wave Equation (FWE) and the Modified Paraxial Equation (MPE)

The envelope approximation leads to consideration of an approximate wave equation. The modified paraxial equation (MPE) has been used in WAKE, and in this thesis we introduce the

enveloped full wave equation (FWE), which will be shown to possess advantages over MPE. To illustrate these, we insert the transverse vector potential Eq. (1.6) into Maxwell's equations in the Lorentz gauge for the fast varying field components, assuming the fast plasma current is determined by the ponderomotive guiding center model, and further assuming the fast electric field is divergence free ($\nabla \cdot \vec{A} \simeq 0$). The resulting enveloped full wave equation (FWE) is

$$\left[\frac{2}{c} \frac{\partial}{\partial t} \left(ik_0 - \frac{\partial}{\partial \xi} \right) - \frac{1}{c^2} \frac{\partial^2}{\partial t^2} + \nabla_{\perp}^2 \right] \hat{A} = \frac{4\pi e^2}{m_e c^2} \left\langle \frac{\bar{n}_e}{\bar{\gamma}} \right\rangle \hat{A}, \quad (1.7)$$

where \bar{n}_e and $\bar{\gamma}$ are the time averaged electron density and relativistic factor, and the angular bracket signifies that an average over an ensemble of particles that stream through the plasma wake generated by the laser pulse is to be taken.

In the slowly varying envelope approximation the derivatives with respect to time - t are considered to be small. The modified paraxial equation (MPE) takes the form

$$\left[\frac{2}{c} \frac{\partial}{\partial t} \left(ik_0 - \frac{\partial}{\partial \xi} \right) + \nabla_{\perp}^2 \right] \hat{A} = \frac{4\pi q^2}{mc^2} \left\langle \frac{\bar{n}}{\bar{\gamma}} \right\rangle \hat{A}, \quad (1.8)$$

where we have dropped $\partial^2 \hat{A} / \partial^2 t$ from the full wave equation (1.7), which is valid under the condition

$$\left| \left(ik_0 - \frac{\partial}{\partial \xi} \right) \hat{A} \right| \gg \left| \frac{\partial \hat{A}}{c \partial t} \right|. \quad (1.9)$$

The paraxial equation makes the further approximation that the derivative with respect to ξ in (1.8) can be ignored. However, important physics is lost when this is done. In particular, the mixed $\xi - t$ derivative is maintained to account for the lowering of the group velocity due to the plasma and transverse variation. Also, this term is needed to describe the depletion of energy from the laser pulse [26]. Equation (1.8) is thus accurate so long as (1.9) is valid. This still allows treatment of cases in which there are significant changes in the spectrum, $\partial / \partial \xi \sim k_0$.

The MPE does preclude treatment of the case in which components of the spectrum are shifted to zero wavenumber. At large spectral shift, when wavenumber variation δk is comparable to the laser central wavenumber k_0 , $\delta k \sim k_0$ and (1.9) is not satisfied, the theoretical dispersion relation for the MPE deviates significantly from that of the FWE (theoretical FWE, Fig. 2.2). In particular the group velocity diverges at small wavenumber.

The differences in dispersion between the MPE and FWE lead to differences in the predicted spectrum. As the spectral shift becomes large, the group velocities in both cases decrease and the low k portions of the pulse fall behind the main pulse (Fig. 2.4). In the moving frame of the simulations the low- k components leave the simulation domain. The MPE model has a lower group velocity than that of the FWE for the same spectral shift (Fig. 3.1). Thus the low- k components of the laser pulse fall behind the main pulse faster for the MPE than from the FWE case (Fig. 3.3).

There is another method, the unidirectional pulse propagation equation (UPPE) [69], that attempts to overcome the computational expense of full Maxwell's equation solvers [70], while still treating pulses with broad spectra. The UPPE is a pseudo-spectral solution of the wave equation in which propagation in one direction is treated. In the UPPE the wave equation is solved in the frequency domain, while the medium's nonlinear response is solved in the time domain. This requires two fast Fourier Transforms per time step. Thus, the UPPE is inherently slower than Finite Difference Time Domain (FDTD). The UPPE encompasses the envelop models described by (1.7) and (1.8). Further, it allows one to describe situation where the linear dielectric response is an arbitrary function of frequency. However, because it is inherently slower than FDTD it is not the methods of choice for laser-plasma interaction.

1.2.4 Numerical Implementation of PIC Simulations

In conventional particle-in-cell (PIC) simulations, Maxwell's equations are usually solved using an explicit finite difference time domain (FDTD) method [71]. In this approach the electric and magnetic fields are defined along the edges of two interleaved cubic grids (known as the Yee grid). The electric and magnetic fields are also defined at staggered times. Thus, the curl of one field, the electric field say, can be computed and used to determine new values of the other field, in this case the magnetic field, a half time step later. This approach, while very simple, has limitations that will now be described. Since the code WAKE uses the vector potential we will illustrate the limitations as they would apply to solutions of the wave equation in the Lorentz gauge,

$$\frac{\partial^2 \tilde{A}}{\partial t^2} - c^2 \nabla^2 \tilde{A} = 0. \quad (1.10)$$

An explicit numerical solution to this equation involves approximating all derivatives by centered finite differences. For example, the differencing for the second order time and space derivatives are evaluated by $[\partial^2 A / \partial t^2]_{i,j} = (A_{i+1,j} - 2A_{i,j} + A_{i-1,j}) / \Delta t^2$ and $[\partial^2 A / \partial x_q^2]_{i,j} = (A_{i,j+1} - 2A_{i,j} + A_{i,j-1}) / \Delta x_q^2$, where i is the time index, j is the spacial index, and $q=1, 2$ and 3 represents the spatial dimensions ($x_1=x$, $x_2=y$ and $x_3=z$). Substituting a plane wave vector potential of the form $\tilde{A} = A_0 e^{i\vec{k}\cdot\vec{z} - i\omega t}$, where A_0 is the amplitude of the wave, and k and ω are the wavenumber and frequency. Eq. (1.10) yields

$$A_0 e^{i\vec{k}\cdot\vec{z} - i\omega t} \left(\frac{e^{-i\omega\Delta t} + e^{i\omega\Delta t} - 2}{c^2 \Delta t^2} \right) = A_0 e^{i\vec{k}\cdot\vec{z} - i\omega t} \sum_{q=1}^3 \left(\frac{e^{ik_q x_q} + e^{-ik_q x_q} - 2}{\Delta x_q^2} \right), \quad (1.11)$$

or

$$\left[\frac{1}{c\Delta t} \sin\left(\frac{\omega\Delta t}{2}\right) \right]^2 = \sum_{q=1}^3 \left[\frac{1}{\Delta x_q} \sin\left(\frac{k_q \Delta x_q}{2}\right) \right]^2. \quad (1.12)$$

Equation (1.12) is the numerical dispersion relation for the FDTD wave equation. Note that when $\Delta t \rightarrow 0$ and $\Delta x_q \rightarrow 0$, $\sin^2(\omega\Delta t/2)/\Delta t^2 \rightarrow \omega^2$ and $\sin^2(k_q\Delta x_q/2)/\Delta x_q^2 \rightarrow k_q^2$.

Comparing (1.12) with the real electromagnetic wave propagating dispersion relation

$$\omega^2 / c^2 = \sum_{q=1}^3 k_q^2, \quad (1.13)$$

one can conclude that numerical dispersion relation approaches the actual dispersion when time and space grids are very small.

However, there are limitations of this standard explicit FDTD method. First, there is a condition, the Courant–Friedrichs–Lewy condition (CFL condition) [72,73], which gives a limitation to the time step size in order for the solution to be stable. In the 1D case of Eq (1.12), for real ω ,

$$\sin^2\left(\frac{\omega\Delta t}{2}\right) = \left(\frac{c\Delta t}{\Delta x}\right)^2 \sin^2\left(\frac{k\Delta x}{2}\right) \leq 1. \quad (1.14)$$

If (1.14) is not satisfied ω is complex and numerical solutions grow exponentially in time. Condition (1.14) can be described as follows. In order for every k value to satisfy this inequality, $(c\Delta t/\Delta x) \leq 1$ must be satisfied. In the 3D case, this condition can be generalized as

$$(c\Delta t)^2 \sum_{q=1}^3 \left(\frac{1}{\Delta x_q}\right)^2 \leq 1. \quad (1.15)$$

Thus, in simulations that spatially resolve the laser pulse wavelength $\Delta x_q \ll \lambda$, the time step must be much smaller than the laser period.

A second limitation to the FDTD-PIC approach is that, when the time and space grids are finite, the numerical wave speed that is determined by (1.12) is slower than the speed of light for wave lengths close to the grid size. Thus, when high-energy particles are being simulated, their speed can exceed the phase velocity of waves supported by the grid as described by (1.12). This results in non-physical radiation called numerical Cerenkov radiation [74], which can invalidate

the PIC simulation results. However, use of the envelope approximation in the moving frame allows us to apply the explicit FDTD method to the Full Wave Equation (FWE) (1.7) and Modified Paraxial Equation (MPE) (1.8) and avoid these limitations. The numerical dispersion relations for these equations are to be discussed in Chap. 3.

1.2.5 The Code WAKE

The code WAKE is used exclusively in our study. It is a fully relativistic, nonlinear, kinetic simulation tool for modeling the propagation of short laser pulses in underdense plasmas. WAKE is a two dimensional code, using a cylindrically symmetric coordinate system and a moving window frame ($\xi=ct-z$, t). Using these simplifications, WAKE solves an envelope equation for the time evolution of the pulse in one transverse and one longitudinal dimension. WAKE employs the particle-in-cell method, but utilizes the disparity of time scales, the QSA, and envelope approximation to significantly reduce computational times [26].

In the original version of WAKE, the modified paraxial equation is solved, which includes corrections of order ω_p / ω_0 to the group velocity. However, for red-shifts comparable to the laser central wavenumber, the dispersion predicted from the MPE in WAKE is not accurate [38]. We have successfully implemented a tenuous plasma full wave equation (FWE) in WAKE extending the modified paraxial equation (MPE) implemented before. We then compare solutions of the two equations for cases in which there is strong spectral shifting. It is found out that the enveloped equations are capable of simulating those regimes as long as spatial and temporal resolution is sufficient and as long as numerical damping is held to a sufficiently low level.

1.3 Structure of the Thesis

The structure of this thesis is as follows. Chapter 2 describes the effects of the plasma's index of refraction on spectral evolution as a laser pulse prorogates in a preformed plasma. Then

the modified paraxial equation (MPE) is introduced with discussions of the approximations applied in this model. Conservation laws are discussed and the amount of spectral shifting as the pulse energy depletes is estimated in various ways. WAKE simulations of three cases are then presented: the 2006 LBNL experiments [18], pulse compression experiments reported by J. Schreiber, *et al.*'s [75], and simulations to compare with the a 1D simulation of Shadwick, *et al.* [41].

Chapter 3 compares the modified paraxial equation (MPE) with the full wave equation (FWE) and their conservation laws. The advantage of FWE over MPE is described through analysis of dispersion relations and group velocities. Simulation results using the FWE in the code WAKE for the UMD parameters are presented and action decay is emphasized. Analysis of the numerical schemes and numerical dispersion relation in WAKE and their effect on the non-conservation of action is then discussed. It is found that higher spatial resolution and higher order numerical differencing yield better conserved action from simulations.

Chapter 4 describes the generation of MIR radiation for parameters relevant to the University of Maryland laser system. The wave action conservation and pulse energy depletion are used to characterize the average spectral shifting. The parametric dependence of MIR energy on laser pulse power, pulse length, and plasma density are further examined to generalize our conclusion of the tunability of the MIR generation.

Chapter 5 gives the summaries of this thesis.

Chapter 2: The Enveloped Wave Equation and Observation of Spectral Modifications in the Laser Wakefield Simulations

2.1 Introduction

Laser wakefield accelerators (LWFAs) are plasma based accelerators in which a single, short, high intensity laser pulse propagates through an underdense plasma exciting a plasma wave whose longitudinal electric field can accelerate particles [1-3]. Recent progress (reviewed in Ref. 26) in the development of LWFAs includes the demonstration of nearly monoenergetic electron beams [11-17], and energy gains in the range of 1 GeV [18,19]. New facilities for the next generation of experiment are under construction [23].

In LWFAs the nonlinear process of plasma wave excitation leads to modification of the laser pulse spectrum. The laser pulse drives a plasma wave when the pulse duration is comparable to the plasma frequency. The laser pulse thus propagates in a region of temporarily varying plasma density and this causes the laser pulse spectrum to evolve. The primary effect is that the laser pulse frequency decreases (red shift) as the pulse loses energy. However, both red and blue shifts of the pulse were observed in previous studies [43-46]. As we will see, it is expected based on conservation of wave action (to be defined) that the laser pulse frequency will be down shifted by an amount comparable to the initial frequency as the laser pulse loses all its energy.

Theoretical study of laser pulse spectral evolution requires physical models that self-consistently treat the propagation of the pulse, and the excitation of plasma waves. The most comprehensive simulation approach is the particle in cell (PIC) method. In this approach the full system of Maxwell's equations are solved on a spatial grid. The plasma is treated as an ensemble of particles that obeys the relativistic equations of motion with the full Lorenz force. Particle charge and current densities are accumulated on the grid and serve as sources in Maxwell's equations. The PIC approach resolves all time scales down to the laser period, and thus is

computationally expensive [39,51-54]. There are also reduced models that make approximations that lead to greater numerical efficiency. A common approach, motivated by the separation in time scales between the laser oscillation period and the plasma wave period and laser pulse duration, is to treat the laser pulse in the envelope approximation. This leads to consideration of the paraxial wave equation. In this approach, changes in the laser frequency are manifested in more rapid variations of the laser pulse envelope. At some point the envelope approximation breaks down. A goal of this study is to investigate this process.

Our study will be based on numerical simulations using the code WAKE [26]. WAKE is a fully relativistic, nonlinear, kinetic simulation tool for modeling the propagation of short laser pulses in underdense plasmas. WAKE is a moving window, particle-in-cell simulation, but utilizes the disparity of time scales to significantly reduce computational times. The time structure of the laser pulse can be separated into high frequency oscillations within the pulse modulated by a slowly varying envelope. Because of this separation of time scales, electrons respond to the pulse two different ways. First, there is a high frequency response that gives rise to currents that modify the laser pulse. Second, there is a low frequency response through the ponderomotive force, which is proportional to the gradient of the laser pulse intensity, $F_p \sim -\nabla I$, and which drives the plasma wave. The plasma period and pulse duration are assumed to be comparable. For this separation of time scales to be valid, it is required that the plasma be tenuous, $\omega_p^2 \ll \omega_0^2$ where ω_p is the plasma frequency, and $\omega_p = (4\pi q^2 n / m)^{1/2}$ is the plasma frequency with n being the plasma density, and q and m being the charge and mass of an electron respectively, and ω_0 is the central frequency of the laser pulse. Using these simplifications, WAKE solves an envelope equation for the time evolution of the pulse in one transverse and one longitudinal dimension. In particular, the modified paraxial equation is solved, which includes to corrections of order ω_p / ω_0 to the group velocity and allows for evaluation of changes temporal changes in

the pulse intensity. Finally, because the plasma is tenuous the evolution of the laser envelope is slow compared to the transit time of electrons through the pulse. Consequently, the field solver for the laser pulse does not need to be updated after every particle time step.

The organization of this chapter is as follows. Section 2.2 describes the influence of the plasma dynamics on the evolution of the spectrum, and provides estimates for the magnitude of spectral changes based on conservation laws. The modified paraxial equation is introduced and its expected regimes of validity are discussed. Diagnostics for characterizing the change in the pulse spectrum are also introduced. Section 2.3 presents simulations of three different cases. These include simulations on the 2006 LBNL experiments [18], pulse compression experiments reported by J. Schreiber, *et al.*'s [75], and simulations to compare with the a 1D simulation of Shadwick, *et al.* [41]. Finally, in Sec. 2.4 we present our conclusions.

2.2 Spectral Modification and Its Simulation Model in WAKE

A laser pulse of duration τ_p is traveling through plasma from right to left as shown in Fig. 2.1. Plasma particles are pushed forward at the pulse front (left) and then outward by the ponderomotive force of the pulse. One plasma period later, the electrons converge on axis. As a result, the plasma density n increases at the front, decreases in the middle and increases again at the back of the pulse. We use a coordinate frame (ξ, t) co-moving with the laser pulse where $\xi = ct - z$ measures the distance back from the head of the pulse. With this choice of coordinates, due to the slow evolution of the laser pulse, the electron density depends on space and time mainly through its dependence on the frame variable ξ .

The space and time dependence of the plasma frequency leads to changes in the frequency and wave number of the laser pulse. The dispersion relation for a light wave propagating in plasma is

$$\omega = \pm \sqrt{|c\vec{k}|^2 + \omega_p^2(t, z) / \gamma}, \quad (2.1)$$

where ω is the laser local frequency; ω_p is the plasma frequency; \vec{k} is the wave number, for positive k_z ($k_z = \hat{z} \cdot \vec{k}$), the plus and minus signs represent forward and backward propagating modes respectively. We are interested in the forward propagation mode in the thesis because our enveloped models neglect all backscatter. As a wavepacket propagates in the time and space varying medium its position and wave number change according to Hamilton's equations with the frequency (2.1) acting as the Hamiltonian. Consequently, due to the time and space dependence of the medium, the wavenumber of the wave packet changes as it propagates according to $\frac{dk}{dz} = \frac{dk/dt}{dz/dt} = -\frac{\partial\omega/\partial z}{\partial\omega/\partial k}$. Performing the indicated differentiations on Eq. (2.1) and considering the forward propagation gives:

$$\frac{dk}{dz} = \frac{1}{2c(\omega^2 - \omega_p^2/\gamma)^{1/2}} \frac{\partial(\omega_p^2/\gamma)}{\partial\xi} \sim \frac{\partial(n/\gamma)}{\partial\xi}, \quad (2.2)$$

where on the right hand side we have used the fact that the plasma density is mainly a function of the frame coordinate. Thus, the local wavenumber shift δk with respect to the laser pulse central wavenumber $k_0 = \omega_0/c$ is proportional to the gradient of the electron density $\partial(n/\gamma)/\partial\xi$ along ξ , and is positive (blue shift) at the pulse front, negative (red shift) in the middle and positive (blue shift) again at the back. As a result, the pulse spectrum broadens.

In the blowout regime the pulse completely expels the background electrons magnifying this effect. In particular, $\partial(n/\gamma)/\partial\xi \sim -n_0/c\tau_p$, which upon using $\omega \gg \omega_p$, provides the following scaling for δk

$$\delta k \simeq (k_p z) \frac{k_p}{\omega_0 \tau_p}, \quad (2.3)$$

where z is the characteristic propagation distance. Setting $\delta k / k \sim 1$ gives the characteristic distance z_s for which the wavenumber shift is comparable to the central wavenumber k_0 :

$$z_s \sim \tau_p c \frac{\omega_0^2}{\omega_p^2}. \quad (2.4)$$

This estimate can also be made on the basis of action conservation as will be discussed.

A frequently used model for the evolution of the laser pulse is based on the so called envelope approximation described in Sec. 1.2.2: the transverse component of the laser vector potential for a linearly polarized wave can be written as an envelope \hat{A} modulating a plane wave traveling at the speed of light, Eq. (1.6). Substituting (1.6) into Maxwell's Equations results in the wave equation or the enveloped full wave equation (FWE), Eq. (1.7). In the slowly varying envelope approximation the derivatives with respect to time - t are considered to be small. The modified paraxial equation (MPE) takes the form as Eq. (1.8).

The range of validity of the paraxial equation can be explored by comparing the approximate and exact dispersion relations. The dispersion relation for the modified paraxial equation predicts an axial group velocity

$$\frac{v_g(k_z)}{c} = 1 - \frac{1}{2} \left(\frac{k_\perp^2 + \omega_p^2 / c^2}{k_z^2} \right), \quad (2.5)$$

whereas the unapproximated group velocity from the full wave equation (1.7) is

$$\frac{v_g(k_z)}{c} = \frac{k_z}{(k_z^2 + k_\perp^2 + \omega_p^2 / c^2)^{1/2}}. \quad (2.6)$$

This implies that the modified paraxial equation is valid when $k_\perp^2, \omega_p^2 / c^2 \ll k_z^2$. Figure 2.2 shows a comparison of Eqs. (2.5) and (2.6) with $\omega_p = 1.17 \times 10^{14} \text{ rad / s}$ and $k_\perp = 8 \times 10^2 \text{ rad / cm}$. The red curve is the group velocity predicted by the MPE which handles only forward propagating waves from Eq. (2.5). The blue curve is the group velocity predicted

by the FWE as a function of k_z for the backward and forward propagation directions represented by the negative and positive k_z axes respectively from Eq. (2.6). The dotted line shows the value of k_z equal to $k_p = \omega_p / c$. The two expressions coincide when $k_z^2 \gg k_\perp^2, \omega_p^2 / c^2$.

From a numerical standpoint the local wavenumber shift can be loosely described by three ranges (Fig. 2.3). For weak wavenumber shifts, $|\delta k| \sim k_p = \omega_p / c$, the time step used for representing the laser pulse need only resolve the plasma frequency. For strong red shifts $|k_0 + \delta k| \sim k_p$, the dispersion relation, Eq. (2.5), is no longer valid and the full wave equation is needed. Finally, for marginal wavenumber shifts $|\delta k + k_0| \gg k_p$, the modified paraxial equation is still valid, and two approaches can be taken to improve accuracy. One can decrease the grid size in ξ to better resolve the scale $k_0 + \delta k$, but this may result in extended simulation times, eliminating one of the strengths of the modified paraxial equation. Alternatively one can introduce a ‘super envelope’ [66]

$$\hat{A} = \hat{A}(\vec{x}_\perp, \xi, t) e^{i\phi(\xi)}, \quad (2.7)$$

where the phase $\phi(\xi, t)$ is specified such that the super envelope \hat{A} remains relatively slowly varying in ξ . The super envelope then satisfies a wave equation that has additional spatially varying terms compared with both Eq. (1.7) and Eq. (1.8), making it complicated computationally.

$$i \frac{2}{c} \left[\frac{\partial}{\partial t} \left(\hat{A} \frac{\partial \phi}{\partial \xi} \right) + \left(ik_0 + \frac{\partial}{\partial \xi} + i \frac{\partial \phi}{\partial \xi} \right) \hat{A} \frac{\partial \phi}{\partial t} \right] + \left[\frac{2}{c} \frac{\partial}{\partial t} \left(ik_0 - \frac{\partial}{\partial \xi} \right) + \nabla_\perp^2 \right] \hat{A} = \frac{4\pi q^2}{mc^2} \left\langle \frac{\bar{n}}{\gamma} \right\rangle \hat{A}. \quad (2.8)$$

Further, it is not guaranteed that a phase $\phi(\xi, t)$ can be found that will keep the super envelope smooth. An example of this will be illustrated in the next section when we consider Wigner plots. There we will find that wave density with different values of wavenumber can occupy the same location. We note also that the envelope phase should also be taken to depend on transverse

coordinate, and this would introduce even more spatially dependent terms in Eq. (2.8). Thus, the most straightforward approach is to simply increase the resolution in ξ .

The relation between wavenumber shift and pulse energy can also be estimated by considering the wave action. First, we note that Eq. (1.8) identically conserves wave action [26], defined as,

$$I_L = \text{Re} \left\{ \int \frac{d^2 x_\perp d\xi}{2\pi c} \hat{A}^* (k_0 + i \frac{\partial}{\partial \xi}) \hat{A} \right\} \sim \frac{U_L}{\langle k \rangle}. \quad (2.9)$$

The quantity, $\langle k \rangle$, is the mean wavenumber, and the pulse energy given by,

$$U_L = \int \frac{d^2 x_\perp d\xi}{2\pi} \left| (k_0 + i \frac{\partial}{\partial \xi}) \hat{A} \right|^2 \quad (2.10)$$

is depleted through driving plasma waves. More detailed description of conservation laws is presented in Sec. 3.6 Appendix 1. As a consequence of (2.9) the mean laser pulse wavenumber must decrease with energy to maintain action conservation. Locally, however, there can still be blue shifts if the pulse length is longer than the plasma period. In this situation the pulse experiences a positive ξ derivative in the index of refraction and the plasma wave can return energy to the electromagnetic wave. Later in chapter we will see that the implementation of Eq. (1.8) fails to conserve action when wave number shifts are large, and part of investigation is devoted to this effect.

The pulse depletion length z_{dp} characterizes the distance over which the pulse energy depletes by 100% or $\delta U_L / U_L \sim 1$. Because the action is conserved, and is approximately proportional to $U_L / \langle k \rangle$ [26], $\delta U_L / U_L \sim 1$ implies $\delta k / k \sim 1 \sim (z_s / c)(\omega_p^2 / \omega^2 \tau_p)$. This is the same condition presented in Eq. (2.4). The rate of energy deposition and the rate of mean laser wavelength shift can also be shown to be equal in the 1D nonlinear regime by 2009 Shadwick et

al. simulatins [41] with the adiabatic invariant of wave action. As an aside, we note that in the blowout regime z_{dp} has the same scaling as the dephasing length [42].

We examine the spectral variation of the laser pulse using three methods. The most direct method is Fourier spectral analysis of the pulse envelope. The spectrum of the envelope is obtained by Fourier transform with respect to the frame coordinate ξ ,

$$\bar{A}(\vec{x}_\perp, \delta k, t) = \int \hat{A}(\vec{x}_\perp, \xi, t) e^{i\delta k \xi} d\xi. \quad (2.11)$$

We note that the transform with respect to the transverse direction has not been taken, so that the quantity \bar{A} still depends on transverse coordinate. The Fourier transform with respect to ξ provides the nonlocal spectrum of the laser pulse; that is to say it cannot distinguish wavenumber shifts at different points ξ within the pulse. While this function is useful for determining the global wavenumber shifts with time, other quantities can give information that is local in ξ .

One quantity that provides a measure of the local wavenumber shift is the Wigner distribution [76,77]. The Wigner distribution for the envelope is defined as

$$W(\delta k, \xi, t) = \frac{1}{2\pi} \int_{-\infty}^{\infty} \hat{A}(\vec{x}_\perp, \xi + \frac{1}{2}\xi', t) \hat{A}^*(\vec{x}_\perp, \xi - \frac{1}{2}\xi', t) e^{i\delta k \xi'} d\xi'. \quad (2.12)$$

The function W can be understood to be similar to a density in $(\delta k, \xi)$ space for the complex laser field. The Wigner distribution is complex, so it is not strictly speaking a density. However, it has the desirable features that

$$\int d\xi W(\delta k, \xi, t) = \frac{|\bar{A}(\delta k, t)|^2}{2\pi}, \quad (2.13a)$$

and

$$\int d(\delta k) W(\delta k, \xi, t) = |\hat{A}(\xi, t)|^2. \quad (2.13b)$$

That is, projections of the Wigner function onto the space or wavenumber axes provide the density in the complementary variable. We will make plots of the real part of the Wigner function that illustrate local changes in the pulse spectrum.

A third method to characterize local wavenumber shifts is to calculate the rate of the phase change of the pulse envelope. We calculate this wavenumber shift, $\overline{\delta k} = -\partial\phi/\partial\xi$, by considering the ‘super envelope’ of A defined in (2.7). Differentiating Eq. (2.7) with respect to ξ and multiplying by \hat{A}^* we find

$$\hat{A}^* \frac{\partial \hat{A}}{\partial \xi} = \hat{A}^* \frac{\partial \hat{A}}{\partial \xi} + i \frac{\partial \phi}{\partial \xi} |\hat{A}|^2. \quad (2.14)$$

The second term in Eq. (2.14) represents the local wavenumber change. Here we consider the weighted average of $\partial\phi/\partial\xi$ over r or $\overline{\delta k} = -\overline{\partial\phi/\partial\xi}$ which can be expressed as

$$\overline{\delta k}(\xi, z) = -\left(\int_0^{r_{\max}} d^2r \operatorname{Im}[\hat{A}^* \frac{\partial \hat{A}}{\partial \xi}] \right) / \left(\int_0^{r_{\max}} d^2r |\hat{A}|^2 \right). \quad (2.15)$$

Definition (2.15) is problematic in regions of ξ where the pulse envelope is small, and where as a consequence $\overline{\delta k}$ is the ratio of two vanishingly small numbers. To eliminate this problem, we simply add a small constant to the denominator of Eq. (2.15), which forces the wavenumber to vanish in these regions, and leaves the wavenumber shifts in regions of large field unchanged.

2.3 Simulations

We simulate the laser pulse propagation and examine the spectral variation of the laser pulse in three situations using WAKE: the 2006 LBNL experiments [18], the 2010 pulse compression experiments of Schreiber *et al.* [75], and the parameters considered in the 2009 1D explicit full wave equation simulations of Shadwick *et al.* [41]. A table of the parameters used in simulating the three cases is shown below.

2.3.1. 2006 LBNL Experiments

We first consider the LWFA parameters of the 2006 LBNL experiments: a 40 TW laser pulse of energy 1.6 J, wave length $\lambda_0 = 810 \text{ nm}$, spot size $w = 2.5 \times 10^{-3} \text{ cm}$, and duration $\tau_p = 80 \text{ fs}$ propagating through a plasma channel with electron density $n_0 = 4.3 \times 10^{18} \text{ cm}^{-3}$. From our previous estimate of z_S given by Eq. (2.4), we find $z_S \sim 5 \text{ mm}$, corresponding to approximately two Rayleigh lengths ($z_R = \omega_0 w^2 / 2c \simeq 2.4 \text{ mm}$).

To characterize the behavior of the pulse profile we examine the energy, action and spectra. The radially averaged pulse profiles as a function of propagation distance z (Here we have introduced the propagation distance $z = ct$ to replace the time variable appearing in Eq. (1.8).) and longitudinal coordinate ξ are shown in Fig. 2.4 (a). The initial tilt of the profile shows the pulse sliding backwards as the linear group velocity is less than c . During the first 5 mm of propagation the pulse undergoes compression resulting in an enhancement of the intensity. As the portion of the pulse in the falling density redshifts, the group velocity decreases and the front and middle region of the pulse coalesce leading to pulse compression. After about 5 mm, local regions of the pulse begin to fall back in the frame consistent with even a lower local group velocity. Late in time the pulse has become heavily depleted as show in Fig. 2.5, in which the energy U and action I_L are plotted as functions of propagation distance z . Energy has depleted about 75% during the whole simulation process (12mm). Action is conserved until $z = 4 \text{ mm}$ at which point it drops continuously by 58% by the end of simulation. Further analysis shows that numerical dissipation of the modified paraxial equation results in the decay of action, and is examined in Chap 3.

Figure 2.4 (b) shows lineouts of the pulse profile at four different propagation distances. The variation of the pulse duration and intensity is demonstrated clearly. An interesting feature is the rapid oscillation in the pulse profile, which we note is sufficiently resolved by our step size in ξ .

The oscillations have a wavelength $\delta\lambda \sim 1 \mu m$ and appear after the laser pulse has reached maximum compression: 3.6 mm (purple) and 4.8 mm (blue) for example. As the portion of the pulse redshifts, it slows down and moves backwards through the center of the pulse. Thus, at the same point in space there are (at least) two wavenumbers resulting in a local beating. The wavelength of $\delta\lambda \sim 1 \mu m$ implies that $\delta k = 2\pi / \delta\lambda \sim 0.8k_0$. This is verified in the Wigner distributions that we consider next.

In Fig. 2.6, the real parts of the Wigner distributions evaluated at $r=0$ are shown as a function of k and ξ at five distances $z = 0, 2.4, 3.6, 4.8$ and 8 mm from left to right. For each distribution the corresponding electron density is also plotted correspondingly. In Fig. 2.6 (h) and (i), we see that there are two peaks at different k -values in the Wigner function for values of ξ corresponding to where the modulations appear in Fig. 2.4 (b). (The presence of multiple peaks in the Wigner distribution shows that the envelope cannot be made smooth by introducing a phase as shown in Eq. (2.7). The separation between these peaks is roughly $\delta k \sim 0.8k_0$, which agrees well with the beat wavelength $\delta\lambda$. As the propagation distance increases, the wavenumber shifts (red shift especially) become larger, and the magnitude of the shift can reach up to 80 to 90% of the central frequency. This indicates that the approximations used for the modified paraxial approximation have locally broken down. It can also be seen that red shift occurs when the density decreases at $\xi = 50 \sim 70 \text{ fs}$ in Figs. 2.6 (b-e). However, a portion begins to blue shift (curved shape at the bottom of Fig. 2.6 (i)) when the density increases at $\xi \sim 150 \text{ fs}$ (Fig. 2.6 (d)). This portion again red shifts when the density starts to decrease again at $\xi = 150 \sim 170 \text{ fs}$ (Fig. 2.6 (e) and (j)).

The global spectrum (Fourier transform) is shown as a false color image in the k - z plane in Fig. 2.7 (a), while lineouts of the spectrum at selected propagation distances are shown in Fig. 2.7 (b). Initially, the spectrum is red shifted (mostly) and broadened as the pulse propagates.

Further, during this phase it develops several peaks. At distances from $z = 3.6-4.8 \text{ mm}$ a large peak appears near $k \sim 0 \ll k_0$ or $|\delta k| = |k - k_0| \sim k_0$, (bright spot at middle left in Fig. 2.7 (a) and blue line in Fig. 2.7 (b)). This is the strong shift case discussed in Fig. 2.3 and is also the point at which action conservation fails (see Fig. 2.5). For later times when the energy has been heavily depleted, there is no further shift in the spectrum.

The local wavenumber shift can be calculated directly from Eq. (2.15) and results for $\overline{\delta k}$ are shown in Fig. 2.8 (a) as false color images in the $\xi - z$ plane, and as lineouts at four instances, $z=0, 2.4, 3.6$ and 4.8 mm , in Fig. 2.8 (b). Comparing these images with the pulse intensity images in Fig. 2.4 (a), we note the blue shift occurs both at the front and back of the pulse while the red shift occurs in the middle, in agreement with the discussion in Sec. 2.2.

2.3.2. Pulse Compression Experiments

We now consider the parameters of the Schreiber *et al.* [75] pulse compression experiment: a laser power of 200 TW , normalized amplitude $a_0 = 3.0$, wavelength $\lambda_0 = 800 \text{ nm}$, duration $\tau_p = 45 \text{ fs}$ and a spot sizes of $w_0 = 22.0 \text{ }\mu\text{m}$ FWHM propagating in a uniform density plasma with $n = 2.3 \times 10^{18} \text{ cm}^{-3}$. Four cases with plasma lengths of $l=0, 4, 6$ and 8.5 mm were compared with the experimental results shown in Fig. 2.9 (a). Fig. 2.9 (a) are Wigner distributions and temporal intensities of the fields for gas jet lengths $l=0, 4, 6$ and 8.5 mm from left to right. Fig. 2.9 (b-d) are simulation results showing: energy and action plots as functions of jet length l , pulse intensity as a function of l and ξ and pulse profiles as functions of ξ at four propagation lengths $l=0, 4, 6$ and 8.5 mm denoted by different colors respectively.

The experiments showed the following phenomena from Fig. 2.9 (a): for the shortest length $l=4 \text{ mm}$, the pulse steepened faster at the back and the total pulse length is reduced; for longer length $l=6 \text{ mm}$, the pulse front is also depleted; for $l=8.5 \text{ mm}$ the pulse duration is reduced from

45 fs to 27 fs FWHM. These can be compared with Fig. 2.9 (d). Fig. 2.9 (d) shows that at $l=4$ mm the back of the pulse steepens and the pulse duration reduces, while at $l=6$ mm the pulse front depletes too and at $l=8.5$ mm the pulse duration decreases to 20~30 fs FWHM. Besides, similar to the simulation results of the LBNL experiments, both Fig. 2.9 (c) and (d) show that pulse is compressed and intensity increases up till $l=7$ mm before it decays due to energy depletion; small oscillations are also observed at the pulse tail at later times, $l=6, 8.5$ mm for example. Fig. 2.9 (b) demonstrates that the energy depletes by around 65% by the end, and action starts to decrease at around $l=6$ mm, and at $l=8.5$ mm it decreases by 45%.

2.3.3. 1D Regime Simulations

Finally, we simulated parameters corresponding to a case considered by Shadwick et al. [41], in which 1D simulations of energy depletion and spectral modification were studied. The purpose of the comparison is twofold: to examine the effects of two dimensionality on the results obtained in Ref. 41, and at the same time to compare the results of WAKE, which uses the MPE, with those of a code that solves the full 1D wave equation. The case of $a_0 = 1$, was examined. To reduce the effect of pulse diffraction, we used a plasma channel with a parabolic radial profile density yielding a matched spot size of $w = 8.3 \mu\text{m}$. The remaining parameters were as follows: a laser power of 2.2 TW wavelength of $\lambda_0 = 810$ nm, and duration $\tau_p = 55.5$ fs propagating in a channel with an on axis electron density of $4.3 \times 10^{18} \text{ cm}^{-3}$ over a distance of 1 cm. In order to ensure the propagation is 1D, the laser power should be less than the critical power for self-focusing [25], $P_{cr} = 17(\omega / \omega_p)^2 \text{ GW}$. For the parameters considered we find $P / P_{cr} \sim 1/3$.

The pulse profile as a function of t and ξ is shown in Fig. 2.10 (a), and the spectrum as a function of t and k is shown in Fig. 2.10 (b). These are very similar to the corresponding images for the LNBL case shown in Fig. 2.4 (a) and Fig. 2.7 (a). The energy and action as a

function of propagation distance from the 1D simulations of Shadwick *et al.* appear in Fig. 2.11 (a) with the WAKE results appearing in Fig. 2.11 (b) for comparison. In the full Maxwell's equations solution for the pulse propagation presented by Shadwick *et al.* action is only an approximate conserved quantity. Thus, the decay in action in Fig. 2.11 (a) is expected. The energy depletion of both simulations are comparable up to $\omega_p t \sim 2270$, at which point the numerical damping in WAKE (discussed in the next section) becomes noticeable as the action begins to drop appreciably in Fig. 2.11 (b). By the end of the simulation, $\omega_p t = 4000$, the action in WAKE has dropped by around 2.5%, much more than that from the 1D simulation (around 0.6%).

Figure 2.12 shows the Wigner distributions at times $\omega_p t = 0, 2270, 3000$ respectively. It can be seen from Fig. 2.11 (b) that the wave action starts to decrease dramatically at about $\omega_p t = 2270$. Comparing with the spectrum Fig. 2.10 (b), we see a large wavenumber shift (up to $\sim 0.6k_0$) appearing at this time. Fig. 2.12 also shows that the frequency is red shifted during the process and reaches to $\sim 0.6k_0$ by the time $\omega_p t = 2270$.

2.4 Conclusion

We have studied the spectral broadening of intense laser pulses propagating in plasma for parameters relevant to Laser Wake Field Acceleration. The studies were carried out using the two-dimensional, paraxial simulation code WAKE, which makes a number of approximations that enable efficient calculation. Several measures of spectral modification were considered including the Fourier spectrum, the rate of change of the envelope phase, and the Wigner function. Simulations of the 2006 LBNL experiments, the recent pulse compression experiments of Schreiber, *et al.*, and the explicit one dimensional simulations of Shadwick, *et al.* were performed. Results of the simulations verified that spectra were substantially modified for all three cases, and

that the spectral changes and energy depletion were consistent with action conservation. For pulses causing complete cavitation large wavenumber shifts, $\delta k / k_0 = .80$, are observed for propagation to a distance where 40%-50% of the pulse energy is depleted, consistent with previous estimates from conservation laws. The extended paraxial equation conserves action up to this distance. Action subsequently decays due to numerical damping and laser propagation out of the simulation domain. Analysis was conducted for the numerical propagation algorithm and numerical schemes in the next chapter and provided insight into the observed action decay for large wavenumber shifts.

Table 2.1 Parameters for the three cases simulated.

	P (TW)	a_0	τ_p (fs)	w (μm)	n_0 (10^{18} cm^{-3})	length (mm)
LBNL	40	0.7	80	25	4.3	12
Schreiber <i>et al.</i>	200	3.0	45	22	2.3	8.5
Shadwick <i>et al.</i>	2.2	1.0	55.5	8.3	4.3	10

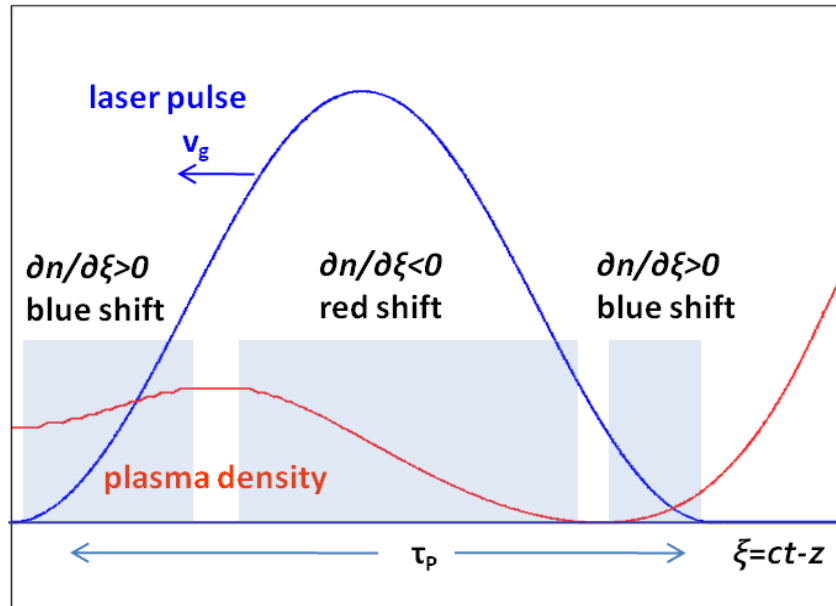


Figure 2.1 Laser pulse of duration τ_p travelling through a plasma to the left. Plasma density n increases at the front of the pulse, decreases in the middle and increases again at the back, resulting blue shift, red shift and blue shift again from front to back.

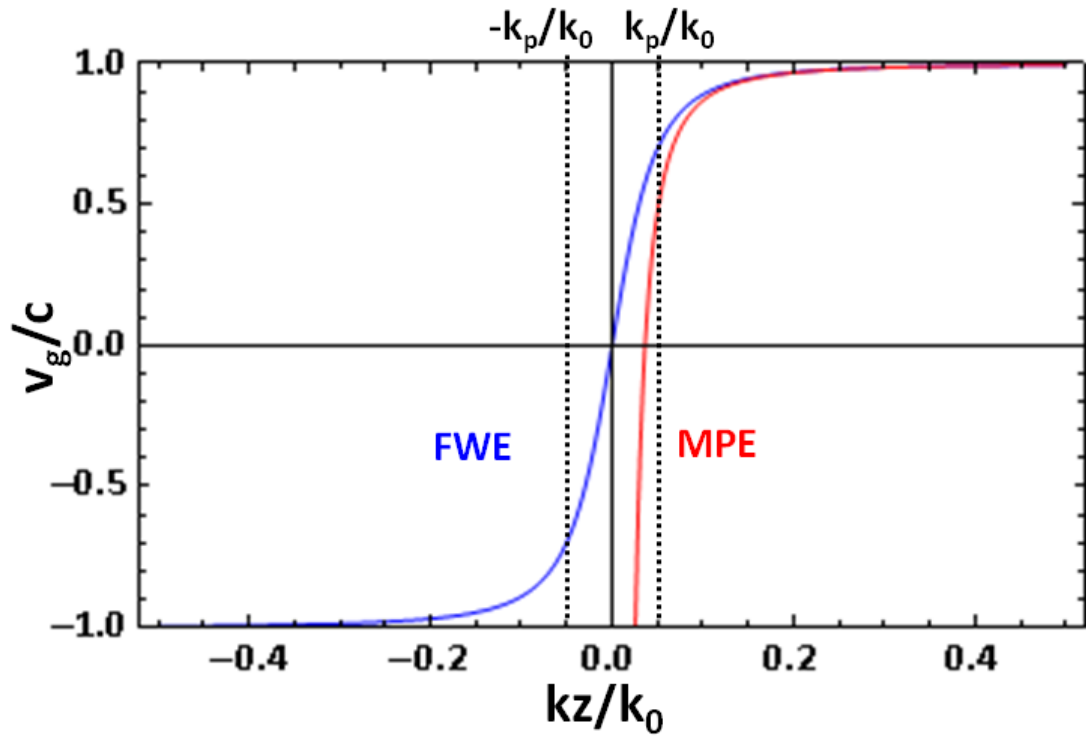


Figure 2.2 Comparison of actual group velocity (blue) and the approximate group velocity (red) as functions of k_z . Plasma wave numbers in two propagation directions are denoted by dashed lines.



Figure 2.3 Local spectral shift δk falls into the weak $|\delta k| \sim k_p$, marginal $|\delta k + k_0| \gg k_p$ and strong $|\delta k + k_0| \sim k_p$ ranges.

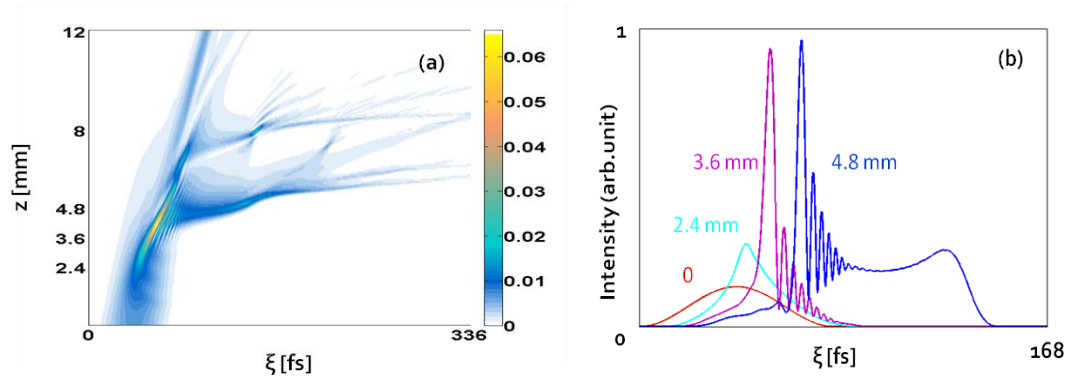


Figure 2.4 (a) Radially averaged pulse intensity profile as a function of (z, ξ) for continuous propagation distance $z=0-12mm$. (b) Pulse intensities as functions of ξ at distances $z=0$ (red), 2.4 (light blue), 3.6 (purple) and 4.8mm (blue). $k_0\Delta\xi = 0.16$ and $\omega_p\Delta t = 0.18$ were applied in WAKE; running time 100 hrs, 1 cpu.

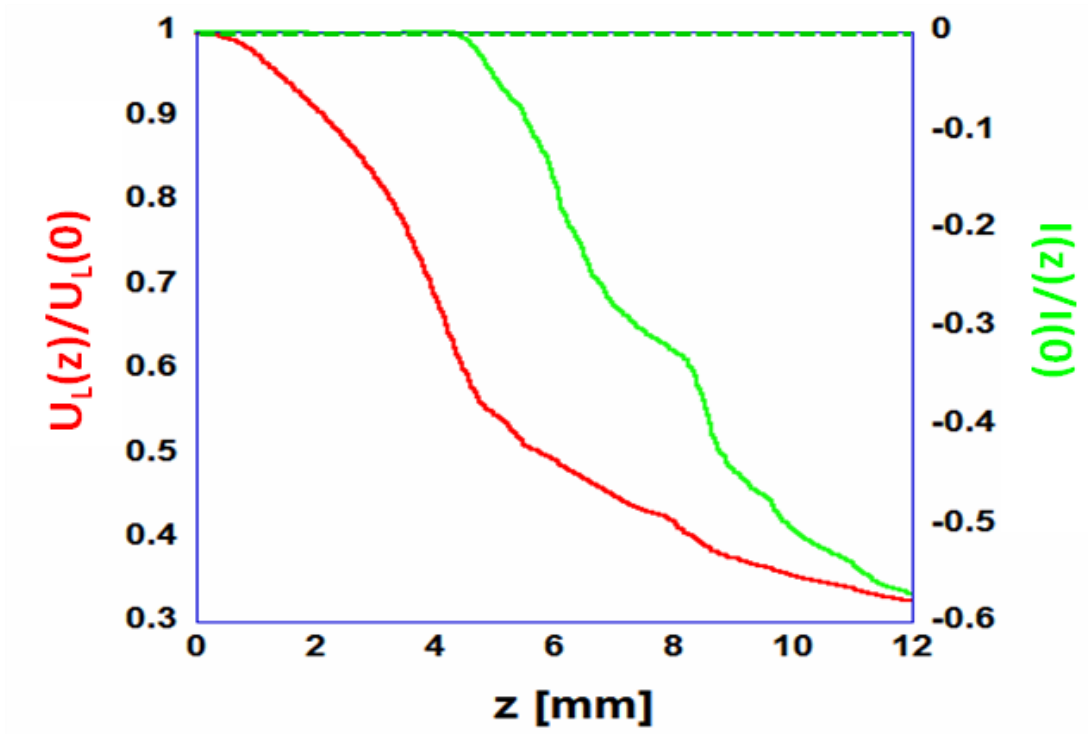


Figure 2.5 Energy (red) and action (green) as functions of propagation distance z . Four moments of interest are denoted by dashed lines: $z=0, 2.4, 3.6$ and 4.8 mm.

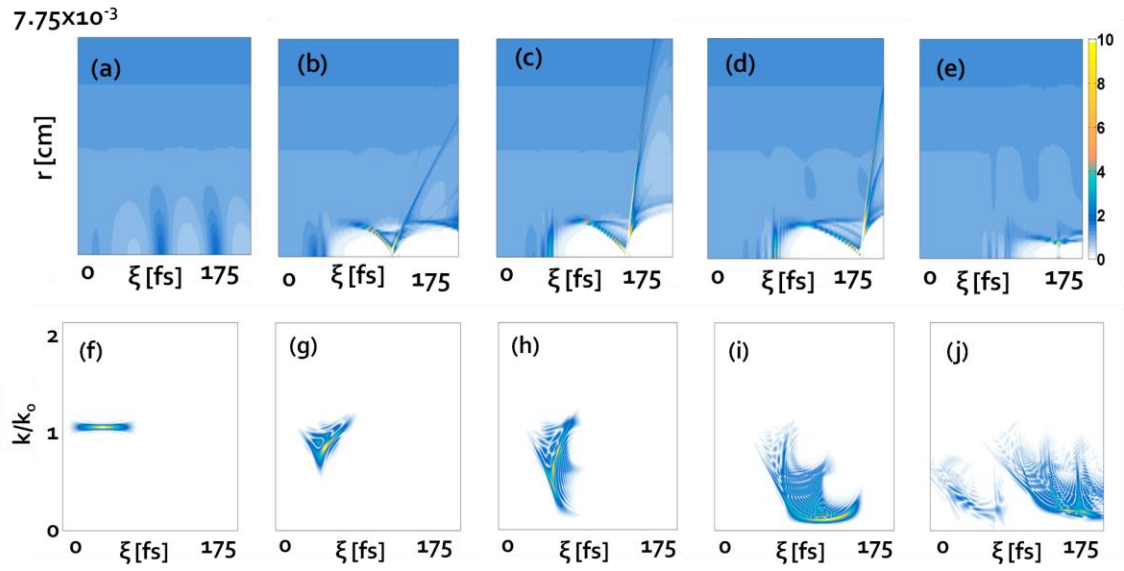


Figure 2.6 (a)-(e) Densities in the (r, ξ) frame at $z=0, 2.4, 3.6, 4.8$ and $8mm$ from left to right.
 (f)-(j) Wigner distributions as a function of (k, ξ) at $z=0, 2.4, 3.6, 4.8$ and $8mm$ from left to right.

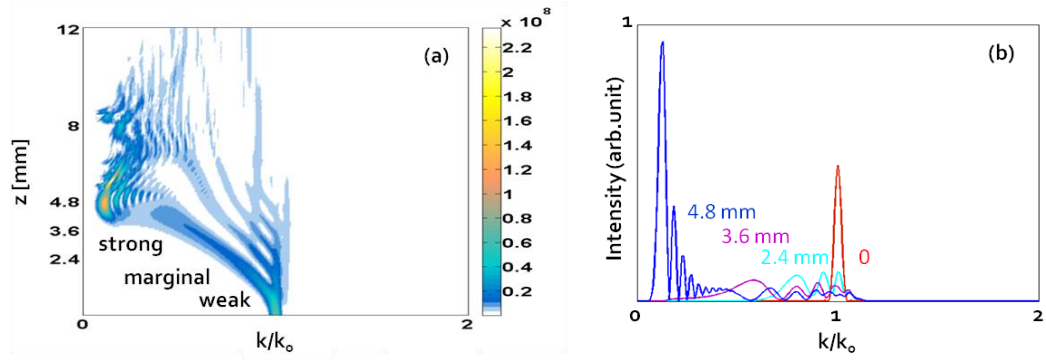


Figure 2.7 (a) Spectral intensity as a function of (z, k) for continuous distance $z=0-12mm$. (b) Spectral intensities at distances $z=0$ (red), 2.4 (light blue), 3.6 (purple) and 4.8mm (blue).

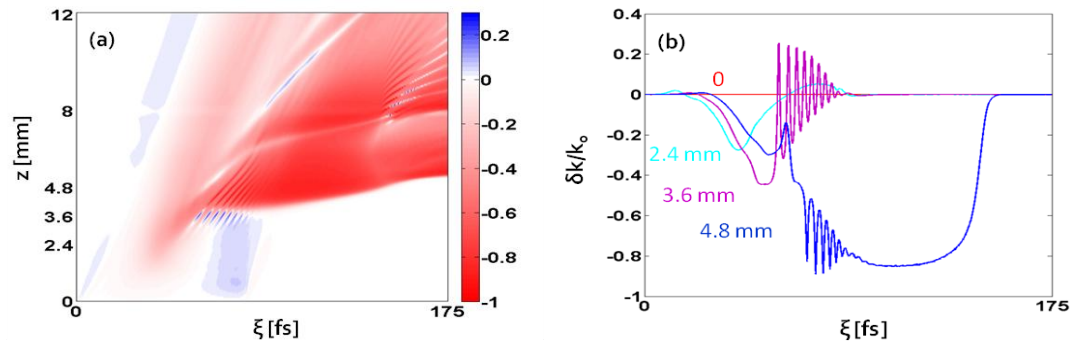


Figure 2.8 (a) Local frequency shift as a function of (z, ξ) for distance $z=0-12mm$. (b) Local frequency shifts as functions of ξ at distances $z=0$ (red), 2.4 (light blue), 3.6 (purple) and 4.8mm (blue).

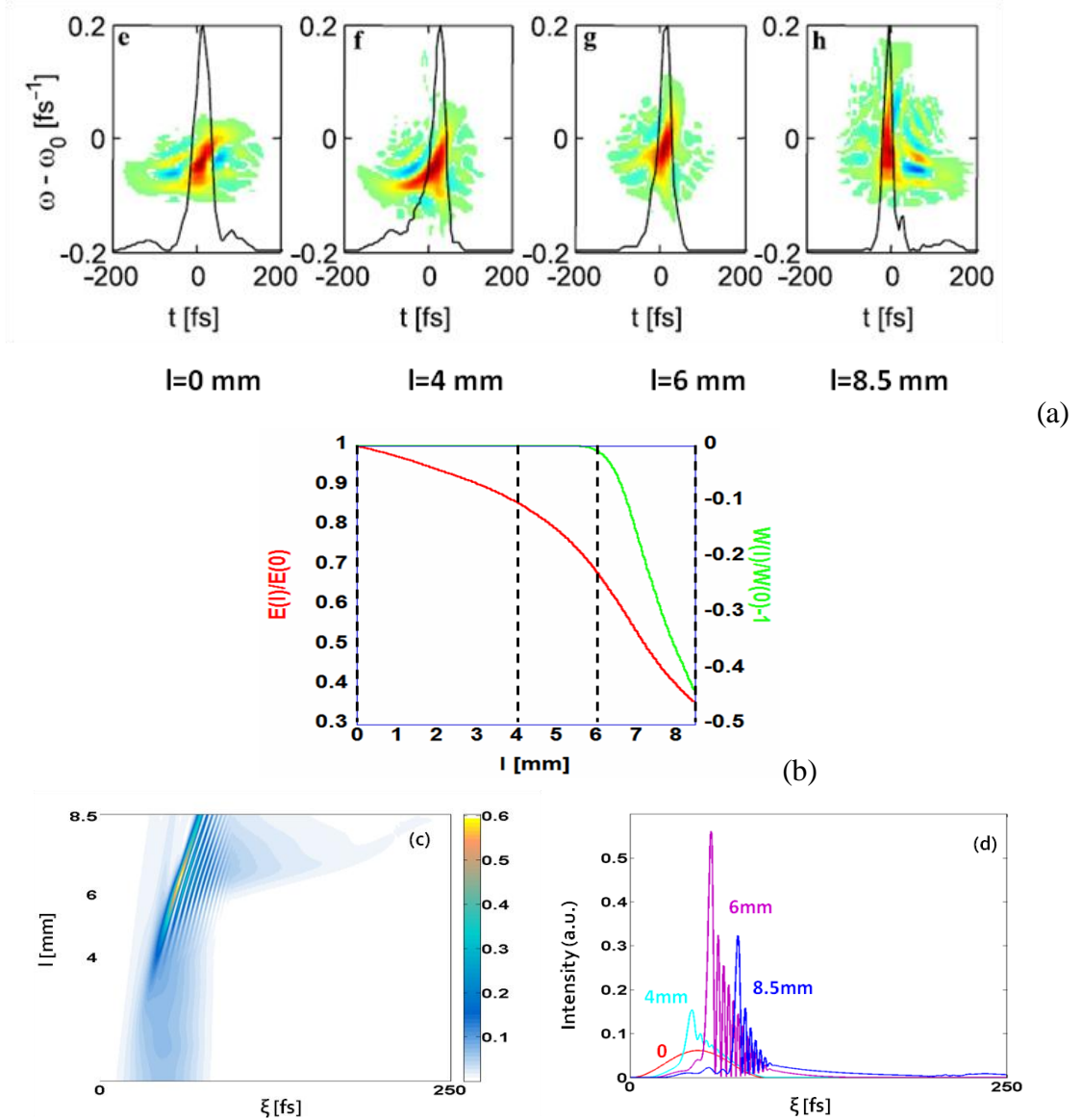


Figure 2.9 (a) Pulse profiles and the Wigner distributions at the background for four experimental cases: gas jet lengths $l=0$, 4, 6 and 8.5 mm from left to right. (b) Energy ratio (red, left axis) and relative action change (green, right axis) as functions jet length l from WAKE. (c) Pulse intensity as a function of (l, ξ) in continuous distance $l=0$ - 8.5 mm from WAKE. (d) Pulse profiles for four jet lengths $l=0$ (red), 4 (light blue), 6 (purple) and 8.5 mm (blue) from WAKE.

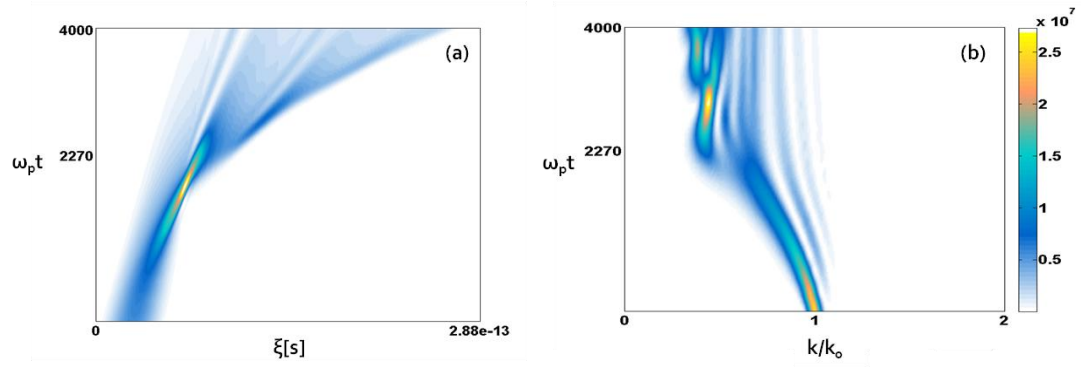


Figure 2.10 (a) is the pulse field intensity as a function of $(\omega_p t, \xi)$, averaged over r ; (b) is the spectrum intensity as a function of $(\omega_p t, k/k_0)$, integrated over r . $k_0 \Delta \xi = 0.14$, $\omega_p \Delta t = 0.2$ were applied, propagation time $\omega_p t = 4000$.

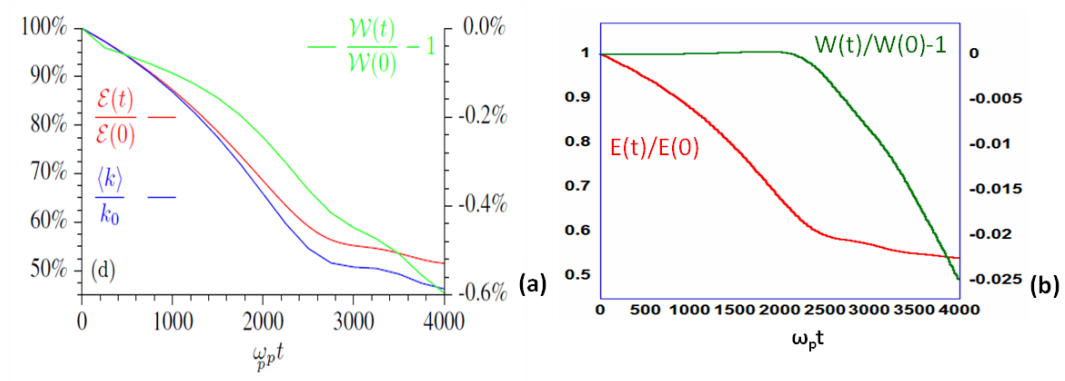


Figure 2.11 (a) Laser energy E (red, left axis), the mean wavenumber $\langle k \rangle$ computed from the first moment of the laser vector potential (blue, left axis), and the relative change in the wave action W (green, right axis) from the 1D explicit simulation. (b) Energy E (red, right axis) and action W (green, right axis) from the WAKE simulation. $k_0 \Delta \xi = 0.14$, $\omega_p \Delta t = 0.2$ were applied and propagation time $\omega_p t = 4000$.

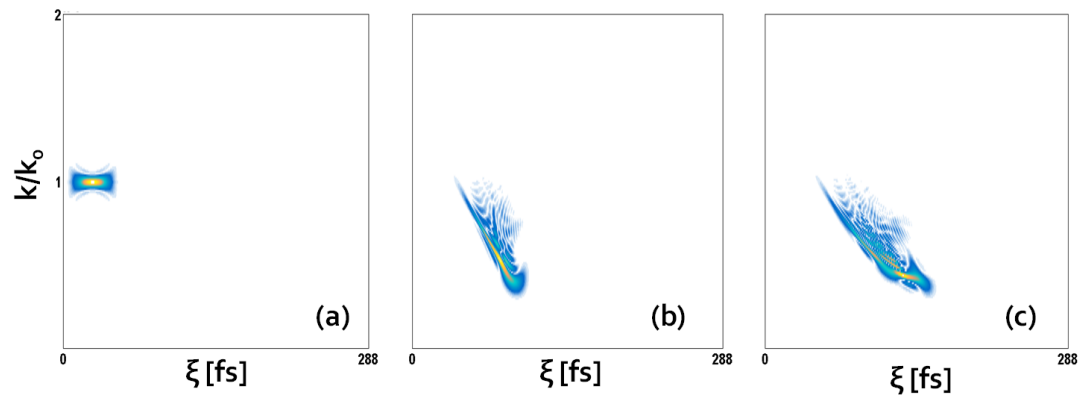


Figure 2.12 Wigner distributions as functions of $(k/k_0, \xi)$ at propagation time $\omega_p t = 0, 2270, 3000$ from left to right.

Chapter 3: Analysis of Conservation Laws and the Numerical Schemes in WAKE

3.1 Introduction

In LWFA (laser wake field accelerators), the laser pulse loses its energy to plasma waves that are generated by the laser pulse's ponderomotive force [25,26]. Accompanying this process the laser pulse experiences spectral broadening and red-shifting [43-46]. We simulate these phenomena using the quasistatic, enveloped laser-plasma simulation code, WAKE [26]. However, for red-shifts comparable to the laser central wavenumber, the validity of the paraxial equation used in WAKE comes into question [38]. We have successfully implemented a tenuous plasma full wave equation (FWE) in WAKE extending the modified paraxial equation (MPE) implemented before. We then compare solutions of the two equations for cases in which there is strong spectral shifting. We find that the enveloped equations are capable of simulating those regimes as long as spatial and temporal resolution is sufficient and as long as numerical damping is held to a sufficiently low level.

The organization of this chapter is as follows. Section 3.2 compares the tenuous plasma, full wave equation (FWE) and the modified paraxial equation (MPE) and their conservation laws. The advantage of FWE over MPE is described through dispersions and group velocities. In Sec. 3.3, the simulations using both FWE and MPE of the UMD parameters are presented and action decays are compared. Section 3.4 presents analysis of the numerical schemes in WAKE and how it affects numerical damping of action. Higher resolution in space and higher numerical fitting method produce more conserved action from simulations. Section 3.5 gives the conclusion of the chapter.

3.2 Full Wave Equation (FWE) and Modified Paraxial Equation (MPE)

Both the FWE and the MPE are equations for the transverse components of the laser vector potential \tilde{A}_\perp (cylindrical represented in a moving window coordinate $(r, \xi = ct - z, t)$ system) as described in Chap2. Each takes the form as Eq. (3.1) (same as (1.7)) and Eq. (3.2) (same as (1.8)) respectively,

$$\left[-\frac{\partial^2}{c^2 \partial t^2} + \frac{2}{c} \frac{\partial}{\partial t} \left(ik_0 - \frac{\partial}{\partial \xi} \right) + \nabla_\perp^2 \right] \hat{A}_\perp = \frac{4\pi q^2}{mc^2} \left\langle \frac{\bar{n}}{\gamma} \right\rangle \hat{A}_\perp, \quad (3.1)$$

for FWE, and

$$\left[\frac{2}{c} \frac{\partial}{\partial t} \left(ik_0 - \frac{\partial}{\partial \xi} \right) + \nabla_\perp^2 \right] \hat{A}_\perp = \frac{4\pi q^2}{mc^2} \left\langle \frac{\bar{n}}{\gamma} \right\rangle \hat{A}_\perp, \quad (3.2)$$

for MPE.

When it is appropriate to neglect the second order time derivative can be understood by considering the group velocity of plane waves in a uniform plasma as described by the two equations. The left-hand side of Eq. (3.1) is the d'Alembertian expressed in the moving window coordinates. The right hand side represents the electron current density. Its form relies on the approximate conservation of canonical momentum for electrons in the laser field. This approximation relies on the excursion of electrons being smaller than the spatial scale over which the vector potential varies. In this regard, for 2D planar simulation with laser electric field plane polarized in the ignorable direction the form of the electron current density is exact.

3.2.1 Numerical dispersion relations and laser pulse group velocities from FWE and MPE

The advantage of retaining the second order term is best seen by comparing the linear dispersion relation for the various models. The dispersion relation for a small amplitude plane wave propagating in plasma is given by Eq. (2.1)

$$\omega = \pm \sqrt{|c\vec{k}|^2 + \omega_p^2(t, z) / \gamma}, \quad (3.3)$$

where ω is the frequency, and \vec{k} the wavenumber. For positive k_z ($k_z = \hat{z} \cdot \vec{k}$), the plus and minus signs represent forward and backward propagating modes respectively. The numerical dispersion relation will depend on the manner in which Eq. (3.1) and (3.2) are converted to finite difference equations and the grid resolutions in ξ and t , $\Delta\xi$ and Δt . Our typical resolutions are $k_0\Delta\xi = 0.28$, $\omega_p\Delta t = 0.54$. Figure 3.1 compares the forward propagation mode dispersion relation given by Eq. (3.3), or full wave solver, with the numerical dispersion relation for our implementation of the FWE and the MPE which are to be described in Sec. 3.4. Here we have taken $\omega_p = 1.17 \times 10^{14} \text{ rad/s}$, $k_0 = 7.8 \times 10^4 \text{ rad/cm}$ and $k_\perp = 8 \times 10^2 \text{ rad/cm}$, corresponding to a plasma density of $4.3 \times 10^{18} \text{ cm}^{-3}$ and vacuum focal spot w_0 ($k_\perp \sim 2/w_0$) of $25 \mu\text{m}$.

The FWE dispersion agrees well with the theoretical curve for small wavenumber shifts, $|k/k_0| \leq 0.1$, and for larger shifts $|k/k_0| \simeq 0$ the discrepancy is less than 20%. Furthermore, the problematic divergence in the MPE dispersion as $|k/k_0| \rightarrow 0$ is eliminated in the FWE. In the current study, the primary advantage of FWE being accurately modeling the dispersion over a wide spectral range is particularly important as we are interested in the generation of long wavelength radiation, correspondingly to large shifts $|k/k_0| \simeq 0.1$.

Comparison of two numerical group velocities with theory for the same ω_p and k_\perp used in Fig. 3.1 is shown in Fig. 3.2. Figure 3.2 is based on Fig. 3.1, compares group velocities v_g as a function of normalized wavenumber k/k_0 from theory (black) and the MPE solver (red) and FWE solver (blue) with a resolution $k_0\Delta\xi = 0.28$ and a time step $\omega_p\Delta t = 0.54$. It can be seen that there is much faster drop of group velocity for MPE compared to the theory, and the discrepancy between the FWE and MPE becomes large for a large spectral red shift, eg., $\sim 0.95k_0$. The consequence is that the group velocity resulting from the FWE is larger than that of MPE. To

examine this in more detail, we have evolved a pulse with an initial redshift of $0.95k_0$ according to both the FWE and MPE solvers with the UMD laser-plasma system as shown in Table 3.1[34]. Figure 3.3 (a) and (b) show the intensity profile averaged over r as a function of propagation distance, z , and moving frame coordinate, ξ , resulting from the FWE and MPE solvers respectively. As expected, due to the reduced group velocity for red shifted light, both solvers show the laser pulse quickly slipping backward in the moving frame. Both are still, however, propagating forward in the lab frame. Also as expected, the FWE slips backwards more slowly.

3.2.2 Conservation laws of FWE and MPE

Both the MPE and the FWE have their own conserved quantity ‘action’, the constancy of which is demonstrate in Appendix 3.6,

$$I_{MPE} = \text{Re} \left\{ \int \frac{d^2 x_{\perp} d\xi}{2\pi c} \hat{A}^* (k_0 + i \frac{\partial}{\partial \xi}) \hat{A} \right\}, \quad (3.4)$$

and

$$I_{FWE} = \text{Re} \left\{ \int \frac{d^2 x_{\perp} d\xi}{2\pi c} \hat{A}^* (k_0 + i \frac{\partial}{\partial \xi} + i \frac{\partial}{c \partial t}) \hat{A} \right\}. \quad (3.5)$$

Field energy depletes as the pulse propagates, because it’s extracted to accelerate plasma electrons and to generate plasma wake fields [8,41,42]. For the MPE the relevant energy is given by

$$U_L = \int \frac{d^2 x_{\perp} d\xi}{2\pi} \left| (k_0 + i \frac{\partial}{\partial \xi}) \hat{A} \right|^2. \quad (3.6)$$

Examination of Eq. (3.6) reveals that U_L is twice the electric field energy associated with the laser pulse. When frequency shifts are small. The plasma contribution to pulse energy is also small, and the electric and magnetic field energies are equal. Thus U_L accurately represents the pulse energy for small shifts. It was shown in Ref. 26 that the rate of change of U_L equals the

negative of the rate at which the ponderomotive potential does work on the plasma in the quasistatic approximation. This is true even when shifts are large so we will use U_L to represent the laser pulse energy.

Comparing expressions for energy and action we see, for both models,

$$\langle k \rangle \sim \frac{U}{I}. \quad (3.7)$$

This implies that as pulse energy depletes, the averaged wavenumber also decreases. Thus the pulse depletion length z_{dp} becomes the estimate of the distance for large wavenumber shifts, $\Delta\lambda/\lambda \sim 1$.

3.3 Simulations and Comparison of FWE and MPE using UMD Parameters

We have simulated with FWE of the UMD laser-plasma system as shown in Table 3.1. Figure 3.4 (a) shows the false color images of the pulse intensity on axis as a function of ξ . Figure 3.4 (b) is the radially averaged pulse intensity as a function of (z, ξ) . The pulse starts from the Gaussian distribution and initially compresses and self-focuses [25, 28] between distance 0-5.5 mm and after it reaches its maximum compressed point at ~ 5.5 mm, it starts to decay. For these simulations a resolution $k_0\Delta\xi = 0.28$, and a time step $\omega_p\Delta t = 0.54$ were used.

As the pulse propagates, the spectrum is red-shifted as seen in Fig.3.5 where the false color images of the spectral intensity of $A_{\perp}(\xi, z)$ are plotted in the k-z plane. Figure 3.5 (a) is the spectrum from the FWE scheme, and Fig. 3.5 (b) is the spectrum from the MPE scheme. Both show that even though there is a large shift, the two schemes produced the similar spectra. Figure 3.5 (c) is the spectrum from Turbowave [65], for which 2D planar geometry was used showing a similar spectrum. Figure 3.5 (a), (b) and (c) all show that the spectra start from the central wave number k_0 and then are broadened and red-shifted as the distance increases. They each reach $\sim 80\%$ wave number shift at $z \simeq 8.0$ mm.

Figure 3.6 and 3.7 illustrate the process of pulse propagation and spectral broadening. Figure 3.6 shows false color images of the laser intensities in the r - ξ plane at different propagation distances, $z=0, 3.7, 5.5, 7.4$ and 8.6 mm. The pulse first self-focuses (b), and then compresses in time (c). After a period it begins to stretch in ξ (d) and then escapes from the simulation domain (e). The evolution of the local spectrum is illustrated in Fig. 3.7 where false color images of the Wigner functions [5,6] in the k - ξ plane are displayed at $r=0$ and the same set of z values as in Fig. 3.6. The initial pulse (a) is given a chirp (b). When cavitation occurs large red shifts appear (c). The stretching of the Wigner density reaches a minimum in k after which density escapes out of the back of the simulation domain (e).

Figure 3.8 illustrates the time evolution of the quadratic quantities action and energy defined in Eqs. (4-6) using FWE and MPE. We note that for the two schemes the corresponding quantities track each other. By the end of the simulation energy has depleted to about 30% of its initial value. Action, which should be conserved in both cases is constant until $z \simeq 8.0mm$ after which it drops precipitously. This drop occurs at a distance corresponding to the images in Fig. 3.6 (d) and Fig. 3.7 (d). The cause of this drop is the propagation of action backward out of the simulation domain that occurs when spectral components of the laser pulse have been red shifted to such an extent that their group velocity fall well below the speed of light.

3.4 Analysis of the Numerical Scheme in WAKE and Non-Conservation of Action

3.4.1. Numerical Scheme for MPE with Three-Point Fitting and Action Decay

The MPE Eq. (3.2) conserves wave action exactly. However, in the simulations of the previous section action is observed to decay. Therefore, this decay must be a result of the numerical implementation of Eq. (3.2). We now consider the dispersion and dissipation associated with the particular discrete numerical implementation of the modified paraxial equation. For this analysis we make the substitution $\nabla_{\perp}^2 \rightarrow -k_{\perp}^2$ and

$(4\pi q^2 / mc^2) \langle \bar{n} / \bar{\gamma} \rangle \rightarrow k_p^2$ in Eq. (3.2), and focus on the discretization of ξ and t derivatives.

The discrete equation is evaluated on a grid point in ξ and half way between two points on the grid in time t

$$\left[\frac{2}{c} \frac{\partial}{\partial t} \left(ik_0 - \frac{\partial}{\partial \xi} \right) \hat{A} \right]_{t+\Delta t/2, \xi} = \left[(k_p^2 + k_\perp^2) \hat{A} \right]_{t+\Delta t/2, \xi}, \quad (3.8)$$

where Δt is the numerical step size in time. The derivative in time is evaluated by simple differencing, $[\partial A / \partial t]_{t+\Delta t/2, \xi} = (A_{t+\Delta t, \xi} - A_{t, \xi}) / \Delta t$. The quantity $\hat{A}_{t+\Delta t/2, \xi}$ on the right is represented by the average $(\hat{A}_{t+\Delta t, \xi} + \hat{A}_{t, \xi}) / 2$. To evaluate the derivative with respect to ξ , we use a three point, one sided difference,

$$\left. \frac{\partial \hat{A}}{\partial \xi} \right|_{\xi} = \frac{1}{\Delta \xi} (1.5 \hat{A}_{\xi} - 2 \hat{A}_{\xi - \Delta \xi} + 0.5 \hat{A}_{\xi - 2 \Delta \xi}). \quad (3.9)$$

This amounts to fitting the three points to a parabola and evaluating the derivative at the point ξ . This differencing is chosen because it leads to a time advancement algorithm that is numerically stable, and it allows (3.10) to be solved for $A_{t+\Delta t, \xi}$ by sweeping in the direction of increasing ξ , thus preserving that no information propagates faster than the speed of light.

We now consider how Eq. (3.8) acts on a plane wave. In the lab frame coordinates a plane wave vector potential can be written $\tilde{A} = A_0 e^{ikz - i\omega t}$, where A_0 is the amplitude of the wave, and k and ω are the lab frame wavenumber and frequency. Upon transforming to laser frame coordinates, $\xi = ct - z$ and t , we have $\tilde{A} = A_0 e^{-ik\xi - i(\omega - ck)t} = \hat{A} e^{-i(k_0 + \delta k)\xi - i\delta\omega t}$. Thus, the lab frame frequency and wavenumber (ω, k) are related to the laser frame (envelope) quantities, $(\delta\omega, \delta k)$ via $k = k_0 + \delta k$, and $\delta\omega = \omega - ck$.

In the discrete case, the mappings that advance the plane wave in ξ and t are given by the following

$$\hat{A}_{t,\xi+\Delta\xi} = e^{-i\delta k\Delta\xi} \hat{A}_{t,\xi} \quad (3.10a)$$

$$\hat{A}_{t+\Delta t,\xi} = e^{-i\delta\omega\Delta t} \hat{A}_{t,\xi} \equiv \lambda \hat{A}_{t,\xi}, \quad (3.10b)$$

where we treat δk as the independent variable that determines $\delta\omega$, $\delta\omega = \delta\omega(\delta k)$, and we note that $\delta\omega$ will be a complex quantity. The quantity $\lambda = e^{-i\delta\omega\Delta t}$ determines the stability and dissipation in our numerical scheme. For instance, if $|\lambda| < 1$ ($|\lambda| > 1$), repeated applications of time advance algorithm, representing propagation over some time interval, will result in the decay (growth) of the wave amplitude. Application of the three point evaluation of the derivative defined in (3.9) yields,

$$\left. \frac{\partial \hat{A}}{\partial \xi} \right|_{\xi} = \frac{1}{\Delta\xi} \left(1.5 - 2e^{i\delta k\Delta\xi} + 0.5e^{i2\delta k\Delta\xi} \right) \hat{A}_{\xi} \equiv -i\delta\hat{k}\hat{A}_{\xi}. \quad (3.11)$$

The numerical wavenumber $\delta\hat{k} \equiv i(1.5 - 2e^{i\delta k\Delta\xi} + 0.5e^{i2\delta k\Delta\xi}) / \Delta\xi \equiv (\delta k_r + i\delta k_i)$ will have both a real and imaginary part. In the limit of small $\delta k\Delta\xi$, corresponding to high numerical resolution of the wavenumber shift, Eq. (3.11) can be Taylor expanded to provide expressions for δk_r and δk_i

$$\delta k_r = \delta k \left[1 + \frac{1}{3}(\delta k\Delta\xi)^2 + \dots \right], \quad (3.12a)$$

$$\delta k_i = \frac{\delta k}{4}(\delta k\Delta\xi)^3 + \dots \quad (3.12b)$$

From Eqs. (3.12a) and (3.12b) we see that as $\Delta\xi \rightarrow 0$, we recover the continuous limit of $\delta\hat{k} = \delta k_r = \delta k$. The imaginary part δk_i represents the numerical damping and is small in the $\Delta\xi \rightarrow 0$ limit. Further, it is seen from (3.12a) that our differencing in ξ is second order accurate as expected. In the Appendix 2 of this chapter we consider a four point fitting for Eq. (3.9) that can be used to reduce the numerical damping. Figures 3.9 (a) and (b) depict δk_r and

δk_i normalized by k_0 respectively for different $\Delta\xi$'s. The orange curves in both plots represent the case $k_0\Delta\xi = 0.56$, reds represent $k_0\Delta\xi = 0.28$, blues represent $k_0\Delta\xi = 0.14$, and blacks represent $k_0\Delta\xi = 0.07$. In Fig. 3.9 (a) a line of positive slope one would represent the continuous limit, while in Fig. 3.9 (b) the value would be zero everywhere. As the resolution increases, δk_r approaches δk , and δk_i approaches zero.

The numerical dispersion relation for $\lambda = e^{-i\delta\omega\Delta t}$ is obtained by substituting the relations $\partial\hat{A}/\partial\xi|_{\xi} = -i(\delta\hat{k})\hat{A}_{\xi}$ and $\partial\hat{A}/\partial t|_{t+\Delta t/2,\xi} = (\lambda-1)\hat{A}_{t,\xi}/\Delta t$ in Eq. (3.8). Upon normalizing and simplifying we find the numerical dispersion relation

$$\lambda = e^{-i\delta\omega\Delta t} = \frac{1 - i\Omega\Delta t / 2}{1 + i\Omega\Delta t / 2}, \quad (3.13)$$

where

$$\Omega = \frac{c(k_p^2 + k_{\perp}^2)}{2(k_0 + \delta\hat{k})}, \quad (3.14)$$

is the frequency shift (when $\delta\hat{k} = \delta k$) for the continuous equation. We note that in the limit $\Omega\Delta t \rightarrow 0$ the frequency shift for the discrete equation approaches that of the continuous equation, $\delta\omega \rightarrow \Omega$. Further, from (3.15) it follows that if $\delta k_i = 0$ then solutions are undamped, $|\lambda| = 1$. Further, when $\delta k_i > 0$, as it is for the three-point-fitting, $|\lambda| < 1$ so the algorithm is stable but dissipative.

Numerical damping of waves, and consequently damping of action, occurs due to nonzero δk_i . From Eqs. (3.13) and (3.14) we note that damping will maximize when $k_0 + \delta k_r \rightarrow 0$. In this case Ω is a negative imaginary number and $|\lambda| < 1$. To illustrate the effect of the numerical damping, we plot the simulation case in Sec. 2.3.3, which is the Shadwick et al.'s 1D regime simulation [41] in Fig 3.10. Figure 3.10 (a) is $|\lambda|^n$ as a function of $\delta k / k_0$ for different values

of $\Delta\xi$, where $n = 2 \times 10^4$ corresponding to $\omega_p t = 4000$ in Ref. 41. The other parameters are $1/k_0 c \Delta t = 0.25$, $k_p = 3.9 \times 10^3 \text{ cm}^{-1}$, and $k_\perp = 8 \times 10^2 \text{ cm}^{-1}$. For each value of $\Delta\xi$, $|\lambda|^n$ becomes significantly less than unity at some negative value of wavenumber shift δk . Thus, regardless of resolution, if the wavenumber shift is large enough, the numerical solution to Eq. (3.2) will be damped. However, for smaller values of $\Delta\xi$, the wavenumber shift required for sizable numerical damping becomes larger (more negative). Furthermore, for weak and marginal wavenumber shifts, $|\pm\delta k| < k_0$, smaller values of $\Delta\xi$ result in negligible damping. This is the case for both blue shift side (right) and red shift side (left). We further considered variations in time step Δt ; we found that the values of $|\lambda|^n$ don't vary significantly as long as $1/k_0 c \Delta t \gg (k_p^2 + k_\perp^2)/k_0^2$. Thus, the main factors controlling the decay of action in the simulations are a combination of the wavenumber shift and the finite resolution in ξ .

Figure 3.10 (b) shows action versus time from WAKE simulations of the Shadwick *et al.*'s 1D regime case in Sec.2.3.3. Two resolutions are considered, $k_0 \Delta\xi = 0.28$ (red) and $k_0 \Delta\xi = 0.14$ (blue). The higher resolution (blue) shows less damping consistent with $|\lambda|$ for $k_0 \Delta\xi = 0.28$ (red) and $k_0 \Delta\xi = 0.14$ (blue) cases respectively as shown in Fig. 3.10 (a). We infer from this that numerical damping leads to non-conservation of action. We note however, that decreasing the grid size by a factor of two does not double the time over which action is conserved. Rather, it appears that the time at which action conservation fails is determined by the time it takes to develop wavenumber shifts $\delta k > 0.5k_0$. Thus, with the given algorithm, and in particular, the three point fitting scheme, there is little benefit to reducing the grid size past $k_0 \Delta\xi = 0.14$.

3.4.2. Numerical Scheme for FWE with Higher-Order-Fitting and Action Decay

The previously used modified paraxial equation (MPE) results from neglecting the second order time derivative in Eq. (3.1). Here we retain the second derivative in the full wave equation (FWE) Eq. (3.1). Similar to MPE, each term in Eq. (3.1) is evaluated at each grid point in ξ and half way between grid points in t

$$\left[\frac{2}{c} \frac{\partial}{\partial t} \left(ik_0 - \frac{\partial}{\partial \xi} \right) \hat{A} \right]_{t+\Delta t/2, \xi} - \frac{1}{c^2} \left[\frac{\partial^2}{\partial t^2} \hat{A} \right]_{t+\Delta t/2, \xi} = \left[(k_p^2 + k_\perp^2) \hat{A} \right]_{t+\Delta t/2, \xi}. \quad (3.15)$$

The differencing for the first and second order time derivatives are evaluated by $[\partial A / \partial t]_{t+\Delta t/2, \xi} = (A_{t+\Delta t, \xi} - A_{t-\Delta t, \xi}) / 2\Delta t$ and $[\partial^2 A / \partial t^2]_{t+\Delta t/2, \xi} = (A_{t+\Delta t, \xi} - 2A_{t, \xi} + A_{t-\Delta t, \xi}) / \Delta t^2$ respectively, and the quantity $\hat{A}_{t+\Delta t/2, \xi}$ on the right of Eq. (3.15) is averaged $(\hat{A}_{t+\Delta t, \xi} + \hat{A}_{t-\Delta t, \xi}) / 2$. This choice of differencing scheme was motivated by its linear stability and dispersion accuracy. To evaluate the derivative with respect to ξ , a four-point, one sided differencing method is applied (see Appendix 2),

$$\left. \frac{\partial \hat{A}}{\partial \xi} \right|_\xi = \frac{1}{\Delta \xi} \left(\frac{5}{3} \hat{A}_\xi - \frac{5}{2} \hat{A}_{\xi-\Delta \xi} + \hat{A}_{\xi-2\Delta \xi} - \frac{1}{6} \hat{A}_{\xi-3\Delta \xi} \right). \quad (3.16)$$

Similar to three-point-fitting, the amount of dissipation is related to the numerical wave number $\hat{\delta k} \equiv -iA_{\perp \xi}^{-1} (\partial A_{\perp} / \partial \xi) |_\xi$, evaluated when $A_{\perp \xi}$ is a plane wave, $A_{\perp \xi} = \exp(i\delta k \xi)$. The wave number is complex $\hat{\delta k} = \delta k_r + i\delta k_i$ and the imaginary part is associated with dissipation. For the three-point method we have $\delta k_i = (\delta k \Delta \xi)^4 / (4\Delta \xi)$ while for the four point method we have $\delta k_i = (\delta k \Delta \xi)^6 / (9\Delta \xi)$.

We have considered the parameters in Table 3.1 and plotted Fig. 3.11 similar to Fig. 3.10. Figure. 3.11 (a) is the quantity $|A_N / A_0|^2$ for $N=554073$ steps of the FWE with several values of axial resolution $\delta k \Delta \xi$ versus wave number shift. This number of steps corresponds to a

propagation distance $z=12.3\text{mm}$. The other parameters are given in the figure caption. As can be seen, the wave becomes damped as the wave number shift increases or the resolution is lowered. The implications of this damping for our propagation studies are illustrated in Fig. 3.11 (b) where action is plotted versus propagation distance for two values of resolution. Initially action is well conserved but decays as wave number shifts become appreciable. The decay is greater when resolution is lower.

The benefits of using the four-point-fitting method are shown in Fig. 3.12. Figure 3.12 (a) compares $|A_N / A_0|^2$ as a function of wave number shift for the two different fitting methods and a particular axial resolution, $k_0\Delta\xi = 0.14$. The four-point method shows substantially less damping. The consequence of using the four-point method in a WAKE simulation of pulse propagation is shown in Fig. 3.12 (b), where action is plotted versus propagation distance. With four point fitting action remains constant until $z \simeq 8.0\text{mm}$ where it drops abruptly. Refining the mesh in ξ does not change the action curve.

We attribute the sharp drop in action occurring at $z \simeq 8.0\text{mm}$ in Fig. 3.12 (b) to convection of action out of the simulation domain. The simulation is carried out in a moving window frame moving at the speed of light c . The group velocity of the laser pulse slows down as the spectrum is red-shifted, and it drops rapidly when the wave number becomes comparable to k_p (Fig. 2.2). Portions of the pulse propagating with velocity below c will leave the simulation domain by moving to larger values of ξ . This process is visible in the nearly horizontal streaks of intensity for large ξ in Fig. 3.4 (b). It is also visible in Figs. 3.6 (e) and 3.7 (e), where intensity and Wigner density are seen a large value of ξ . The expressions for v_g in Chap. 2 indicate that v_g is determined by the spectral shift rate, i.e., the larger the spectral shift, the greater the rate at which action will leave the simulation domain.

We note from Fig. 3.8 that the abrupt drop in action occurs over a propagation distance of 8 mm. The portion of the pulse contributing to this drop needed to fall back in the moving window

by about 150fs. This implies a velocity difference $(c - v_g)/c = 5.3 \times 10^{-2}$, which is consistent with the slope of the intensity streak in Fig. 3.4 (b).

3.4.3. Conclusions of Numerical Schemes and Action Decay

Equation (3.1) and (3.2) are solved numerically, using finite difference representations of the derivatives described in Sec. 3.4.1 and 3.4.2. In our numerical routine values of A_{\perp} are defined on a regular grid in r , ξ and t . The terms in the equation are then expressed on the grid in r and ξ , and half way between two grid points in t in the case of the MPE ($\partial/\partial t$ term) and at the grid points in the case of the FWE ($\partial^2/\partial t^2$ term). Numerical dissipation enters the solution because the derivative in ξ is not centered on the grid in ξ . This allows the solution to be advanced in t by sweeping through ascending values of ξ .

The amount of dissipation is related to the numerical wave number $\delta\hat{k} \equiv -iA_{\perp\xi}^{-1}(\partial A_{\perp}/\partial\xi)|_{\xi}$, evaluated when $A_{\perp\xi}$ is a plane wave, $A_{\perp\xi} = \exp(i\delta k\xi)$. The wave number is complex $\delta\hat{k} = \delta\hat{k}_r + i\delta\hat{k}_i$ and the imaginary part is associated with dissipation. In the limit of small $\delta k\Delta\xi$, corresponding to high resolution or small wave number shift, the imaginary part is small. The effect of numerical dissipation can be studied by considering the linear evolution of plane wave amplitudes under the discretized wave equations. Specifically, we consider the ratio $A_N/A_0 = \hat{A}_{t_0+N\Delta t}/\hat{A}_{t_0}$ for a plane wave with longitudinal wave number $k = \delta k + k_0$ and transverse wave number k_{\perp} . In the absence of numerical dissipation $|A_N/A_0| = 1$.

3.5 Conclusions

We have implemented a full d'Alembertian in the laser field evolution equation in WAKE. The results that we find for pulse evolution, energy depletion, and spectral modification are

remarkably similar to those previously obtained with the modified paraxial equation. The accuracy of calculations is monitored by observing the time dependence of wave action. Numerical damping of action can be minimized by a combination of high resolution in ξ and higher order evaluation of ξ derivatives. Action does decay in the simulations, but due to convection out of the simulation domain, we conclude that WAKE is an accurate tool for studying energy depletion and spectral broadening in intense laser-plasma interactions.

3.6 Appendix 1: Conservation Laws

We are going to derive the conservation laws from the full envelope wave equation (FWE): the conservation of laser wave action and the conservation of particle and laser energy. Similar to the derivations from the modified paraxial equation (MPE) [26], we start from writing the radiant field in terms of an envelope modifying a plane wave travelling as the speed of light,

$$\tilde{A}_\perp = \hat{A}_\perp(\vec{x}_\perp, \xi, t)e^{-ik_0\xi} + c.c.. \quad (3.17)$$

The evolution of the envelope is determined by the full wave equation,

$$\left[-\frac{\partial^2}{c^2 \partial t^2} + \frac{2}{c} \frac{\partial}{\partial t} \left(ik_0 - \frac{\partial}{\partial \xi} \right) + \nabla_\perp^2 \right] \hat{A}_\perp = \frac{4\pi q^2}{mc^2} \left\langle \frac{\bar{n}}{\gamma} \right\rangle \hat{A}_\perp. \quad (3.18)$$

To derive the conservation of wave action we multiply Eq. (3.18) by \hat{A}_\perp^* , integrate over all volume, and subtract from that quantity its complex conjugate,

$$\frac{1}{c^2} \frac{d}{dt} \int d^3x \left[\hat{A}_\perp \cdot \frac{\partial \hat{A}_\perp^*}{\partial t} - \hat{A}_\perp^* \cdot \frac{\partial \hat{A}_\perp}{\partial t} \right] + \frac{2}{c} \frac{d}{dt} ik_0 \int d^3x |\hat{A}_\perp|^2 + \frac{2}{c} \int d^3x \left[\hat{A}_\perp \cdot \frac{\partial^2 \hat{A}_\perp^*}{\partial t \partial \xi} - \hat{A}_\perp^* \cdot \frac{\partial^2 \hat{A}_\perp}{\partial t \partial \xi} \right] = 0. \quad (3.19)$$

Here we assume that the laser amplitude vanishes at infinity so that boundary terms can be neglected. Using the identity,

$$\int d^3x \left[\hat{A}_\perp \cdot \frac{\partial^2 \hat{A}_\perp^*}{\partial t \partial \xi} - \hat{A}_\perp^* \cdot \frac{\partial^2 \hat{A}_\perp}{\partial t \partial \xi} \right] = \frac{1}{2} \frac{\partial}{\partial t} \int d^3x \left[\hat{A}_\perp \cdot \frac{\partial \hat{A}_\perp^*}{\partial \xi} - \hat{A}_\perp^* \cdot \frac{\partial \hat{A}_\perp}{\partial \xi} \right]. \quad (3.20)$$

To rewrite Eq. (3.19) as a conservation law,

$$\frac{d}{dt} \left\{ \frac{1}{c} \int d^3x \left[\hat{A}_\perp \cdot \frac{\partial \hat{A}_\perp^*}{\partial t} - \hat{A}_\perp^* \cdot \frac{\partial \hat{A}_\perp}{\partial t} \right] + 2ik_0 \int d^3x |\hat{A}_\perp|^2 + \int d^3x \left[\hat{A}_\perp \cdot \frac{\partial \hat{A}_\perp^*}{\partial \xi} - \hat{A}_\perp^* \cdot \frac{\partial \hat{A}_\perp}{\partial \xi} \right] \right\} = 0. \quad (3.21)$$

This is interpreted as the conservation of action Eq. (3.5),

$$I_{FWE} = \text{Re} \left\{ \int \frac{d^2x_\perp d\xi}{2\pi c} \hat{A}^* \left(k_0 + i \frac{\partial}{\partial \xi} + i \frac{\partial}{c \partial t} \right) \hat{A} \right\}, \quad (3.5)$$

where I_{FWE} is a conservative quantity.

While the form of action has been modified for FWE, the laser pulse energy which is the sum of the electric and magnetic energy stays the same as that of MPE,

$$U_L = \int \frac{d^2x_\perp d\xi}{2\pi} \left| \left(k_0 + i \frac{\partial}{\partial \xi} \right) \hat{A} \right|^2. \quad (3.6)$$

3.7 Appendix 2: Four-Point-Fitting Scheme

By using a four-point-fitting scheme as opposed to the three point fitting scheme presented in section VI δk_i and hence the numerical damping can be reduced. Similar to the three point fitting method, one can assume that the first derivative of \hat{A}_{j+3} can be approximated by the values of \hat{A}_{j+3} , \hat{A}_{j+2} , \hat{A}_{j+1} and \hat{A}_j (excluding boundaries) by fitting them on a curve as follows

$$\left. \frac{\partial \hat{A}}{\partial \xi} \right|_{j+3} = \frac{1}{\Delta \xi} \left(c_0 \hat{A}_{j+3} + c_1 \hat{A}_{j+2} + c_2 \hat{A}_{j+1} + c_3 \hat{A}_j \right), \quad (3.22a)$$

which upon using Eq. (3.10a) is simply:

$$\left. \frac{\partial \hat{A}}{\partial \xi} \right|_{j+3} = \frac{1}{\Delta \xi} \hat{A}_{j+3} \left(c_0 + c_1 e^{i\delta k \Delta \xi} + c_2 e^{i2\delta k \Delta \xi} + c_3 e^{i3\delta k \Delta \xi} \right). \quad (3.22b)$$

We define $\hat{\delta k} \equiv i(c_0 + c_1 e^{i\delta k \Delta \xi} + c_2 e^{i2\delta k \Delta \xi} + c_3 e^{i3\delta k \Delta \xi}) / \Delta \xi \equiv (\delta k_r + i\delta k_i)$ such that $\partial_\xi \hat{A}|_{j+3} = -i(\hat{\delta k}) \hat{A}|_{j+3}$ where δk_r and δk_i are real and imaginary components of the ‘numerical operator $\hat{\delta k}$ ’.

For a sufficiently resolved wavenumber shift, $\delta k \Delta \xi \ll 1$, and we can Taylor expand $\hat{\delta k}$ providing

$$\hat{\delta k} = \frac{i}{\Delta \xi} \left[f_0 + if_1(\delta k \Delta \xi) + f_2(\delta k \Delta \xi)^2 + if_3(\delta k \Delta \xi)^3 + f_4(\delta k \Delta \xi)^4 + \dots \right], \quad (3.23)$$

where the f_i are functions of the c_i . In order to be consistent with the continuous limit, we want $f_0 = 0$ the first order term to be equal to $-i\Delta \xi \delta k$ when $\Delta \xi \rightarrow 0$. In addition the even ordered terms should be as small as possible because they result in numerical damping. Our conditions are as follows:

$$\begin{aligned} f_0(c_0, c_1, c_2, c_3) &= 0 \\ f_1(c_1, c_2, c_3) &= -1 \\ f_2(c_1, c_2, c_3) &= 0 \\ f_4(c_1, c_2, c_3) &= \mu \end{aligned}, \quad (3.24)$$

where μ is a free parameter that we can use to specify one additional condition. Solving for the c_i and rewriting $\hat{\delta k}$ we have

$$\hat{\delta k} = \frac{i}{\Delta \xi} \left[\left(\frac{5}{3} - \frac{2}{3} \mu \right) - \left(\frac{5}{2} - 2\mu \right) e^{i\delta k \Delta \xi} + (1 - 2\mu) e^{i2\delta k \Delta \xi} - \frac{1}{6} (1 - 4\mu) e^{i3\delta k \Delta \xi} \right], \quad (3.25)$$

where for small $\delta k \Delta \xi$

$$\delta k_r = \delta k \left[1 + \frac{1}{6} (4\mu + 1) (\delta k \Delta \xi)^2 - \frac{1}{120} (100\mu - 11) (\delta k \Delta \xi)^4 + \dots \right], \quad (3.26a)$$

$$\delta k_i = \delta k \left[\mu (\delta k \Delta \xi)^3 - \frac{1}{18} (9\mu - 2) (\delta k \Delta \xi)^5 + \dots \right]. \quad (3.26b)$$

For the least numerical damping/growth δk_i should be as small as possible, setting $\mu = 0$ provides a δk_i of $O[(\delta k \Delta \xi)^6]$, providing

$$\delta k_r = \delta k \left[1 + \frac{1}{6} (\delta k \Delta \xi)^2 + \dots \right], \quad (3.27a)$$

$$\delta k_i = \frac{1}{9 \Delta \xi} (\delta k \Delta \xi)^6 + \dots \quad (3.27b)$$

The solution is still stable, and damping is considerably reduced compared with the three-point-fitting method, which we see by comparing Eqs. (3.27b) and (3.12b). In addition, the real part deviates less from δk comparing Eqs. (3.27a) and (3.12a).

Table 3.1 UMD laser-plasma system parameters.

Quantity	Value
U (J)	0.5
a_0	0.45
τ_P (fs)	60
w (μm)	25
n_0 (10^{18} cm^{-3})	4.3
Length (mm)	12.3

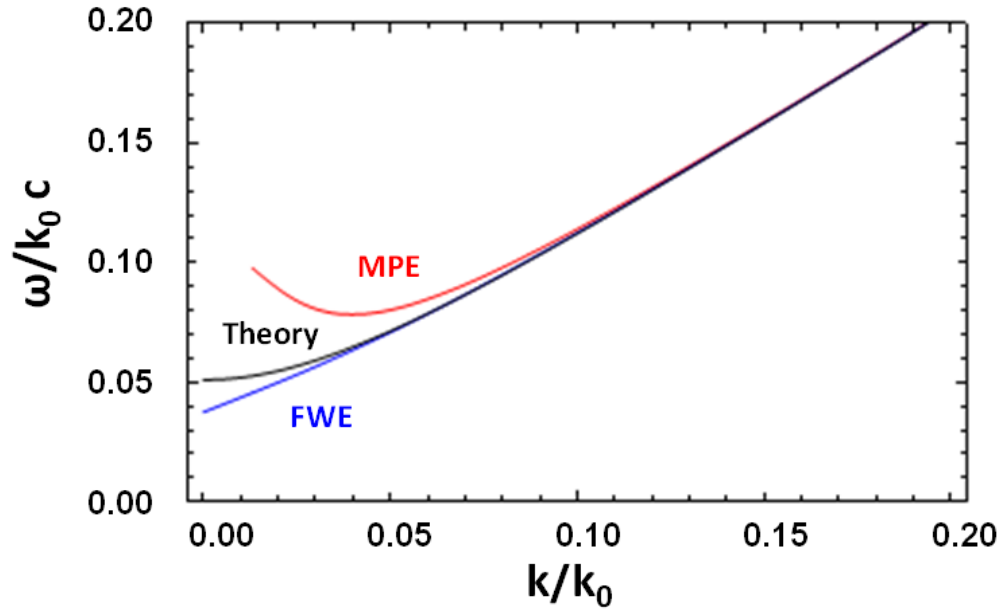


Figure 3.1 Normalized frequency, ω/k_0c , as a function of normalized wavenumber k/k_0 from theory (black) and the MPE solver (red) and FWE solver (blue) with a resolution $k_0\Delta\xi = 0.28$ and a time step $\omega_p\Delta t = 0.54$. Here we have taken $\omega_p = 1.17 \times 10^{14} \text{ rad/s}$, $k_0 = 7.8 \times 10^4 \text{ rad/cm}$ and $k_{\perp} = 8 \times 10^2 \text{ rad/cm}$.

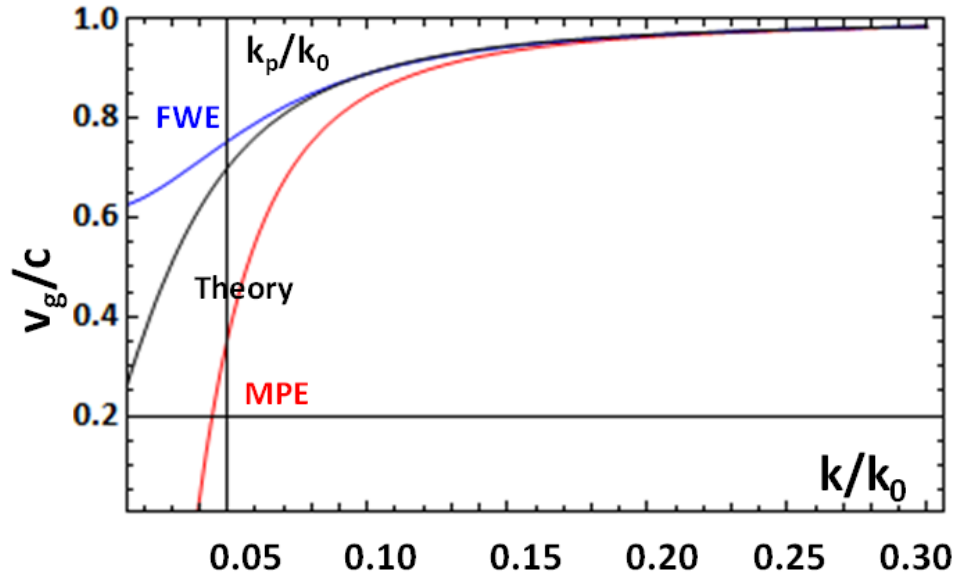


Figure 3.2 Comparison of group velocity v_g as a function of normalized wavenumber k/k_0 from theory (black) and the MPE solver (red) and FWE solver (blue) with a resolution resolution $k_0\Delta\xi = 0.28$ and a time step $\omega_p\Delta t = 0.54$. Here we have taken $\omega_p = 1.17 \times 10^{14}$ rad/s, $k_0 = 7.8 \times 10^4$ rad/cm and $k_\perp = 8 \times 10^2$ rad/cm.

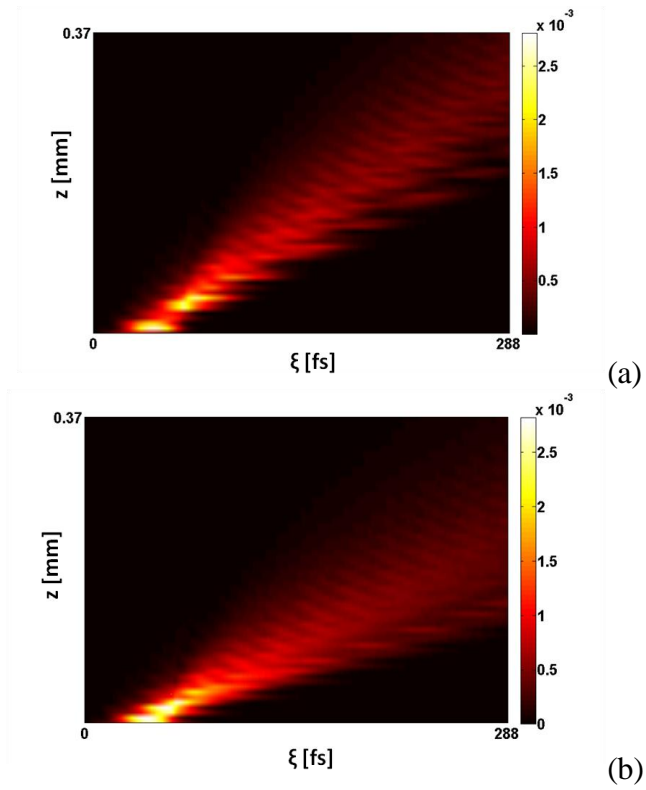
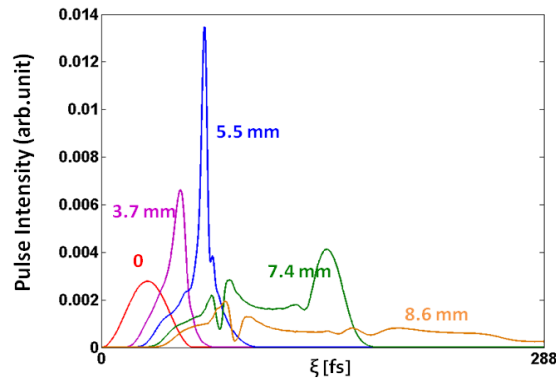
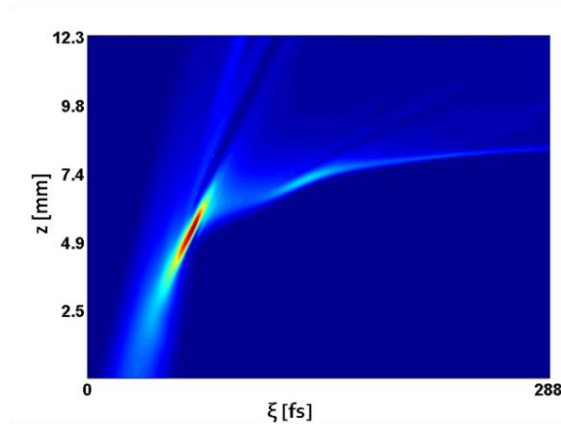


Figure 3.3 Radially averaged laser fields as a function of propagation time or distance z and ξ from FWE (a) and MPE (b) models respectively.



(a)



(b)

Figure 3.4 (a) Pulse intensities as functions of ξ at distances $z=0$ (red), 3.7 (purple), 5.5 (blue), 7.4 (green) and 8.6mm (orange). $k_0\Delta\xi = 0.14$ and $\omega_p\Delta t = 0.09$ were applied in WAKE; running time 1.5 hrs, 1 cpu. (b) Radially averaged pulse intensity profile as a function of (z, ξ) for continuous propagation distance $z=0-12.3$ mm.

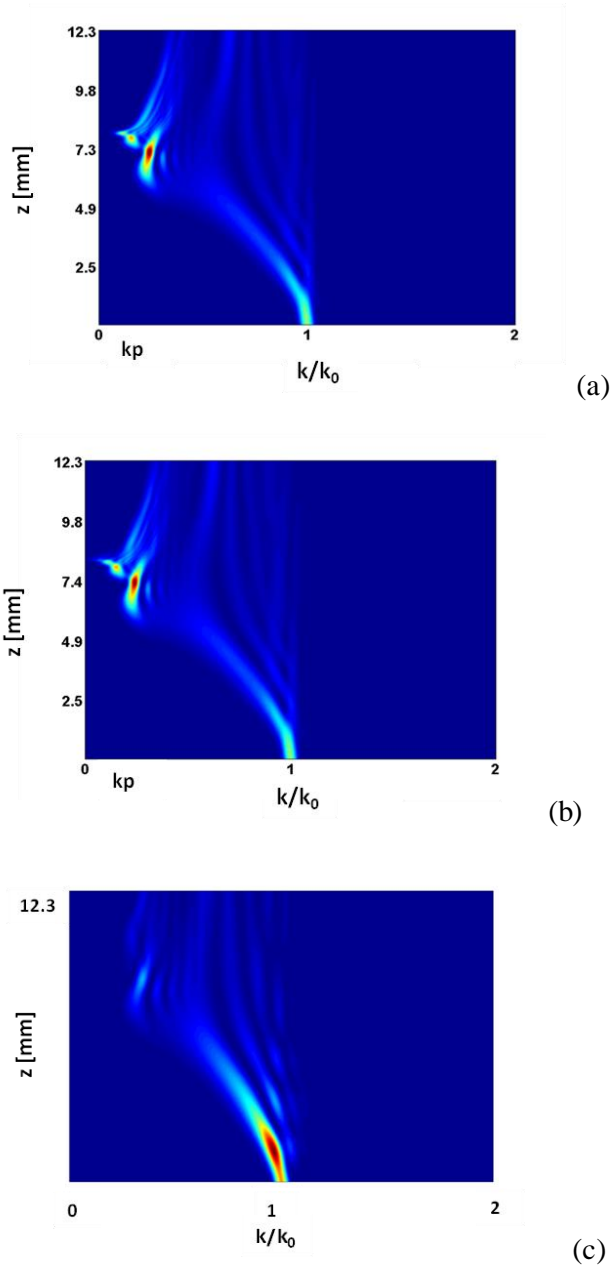


Figure 3.5 (a) Spectral intensity as a function of (z, k) for continuous distance $z=0-12.3$ mm from the full wave equation (FWE). (b) Spectral intensity from modified paraxial equation (MPE). (c) Spectral intensity Turbowave (2D planar geometry).

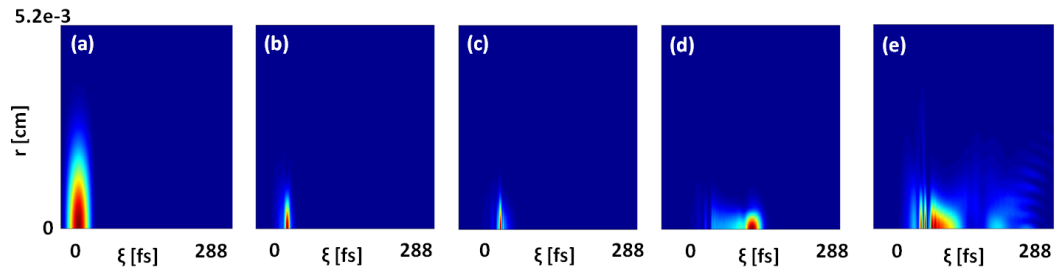


Figure 3.6 (a)-(e) Pulse profiles as a function of (r, ξ) at $z=0, 3.7, 5.5, 7.4$ and 8.6 mm. from left to right.

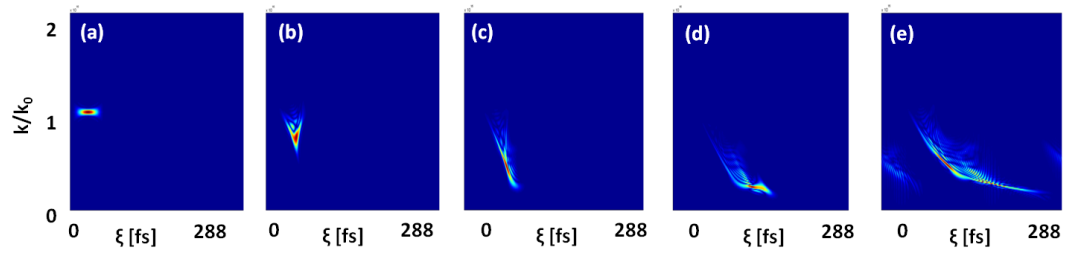


Figure 3.7 (a)-(e) Wigner distributions as a function of (k, ξ) at $z=0, 3.7, 5.5, 7.4$ and 8.6 mm. from left to right.

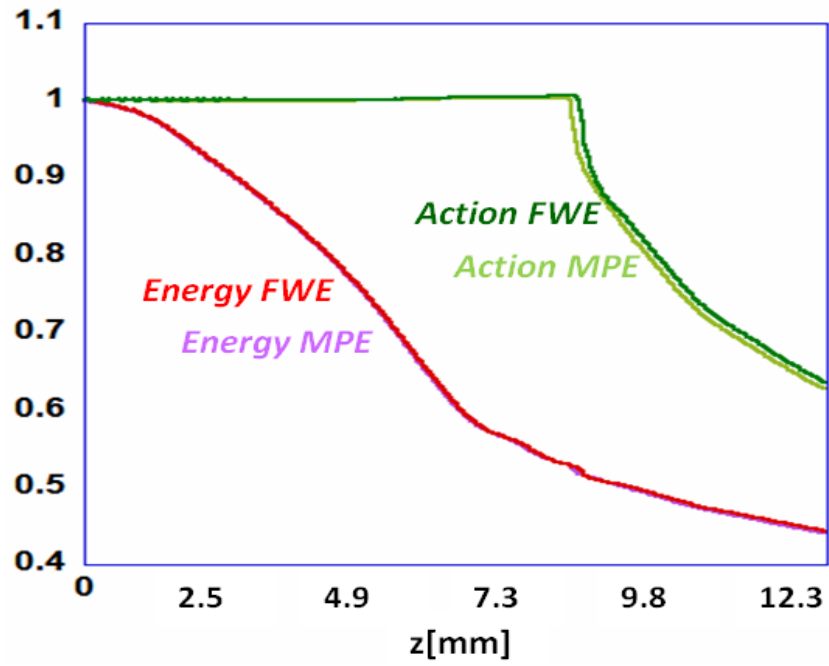


Figure 3.8 Energy (red for FWE, purple for MPE) and action (dark green for FWE and light green for MPE) as functions of propagation distance z .

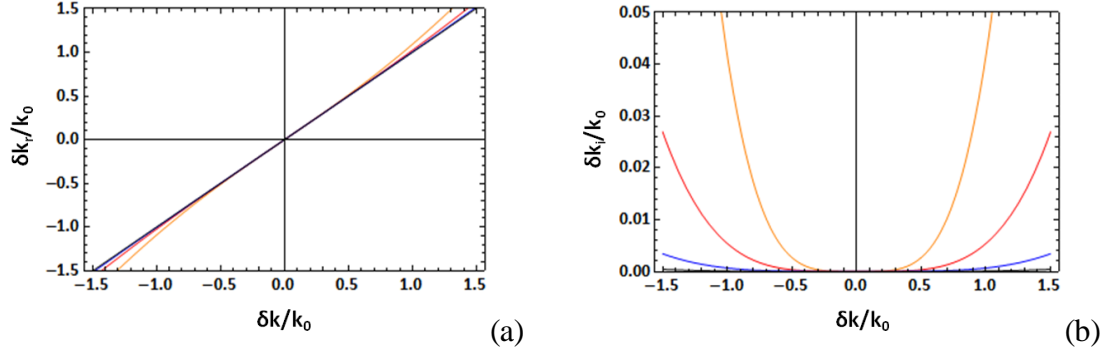


Figure 3.9 δk_r (a) and δk_i (b) of the ‘numerical operator’ $\hat{\delta k}$ as functions of $\delta k/k_0$ with 3-point fitting method in the MPE solver, for both red shifts $\delta k/k_0 < 0$ and blue shifts $\delta k/k_0 > 0$. The orange curves represent the case $k_0\Delta\xi = 0.56$, reds represent $k_0\Delta\xi = 0.28$, blues represent $k_0\Delta\xi = 0.14$, and blacks represent $k_0\Delta\xi = 0.07$.

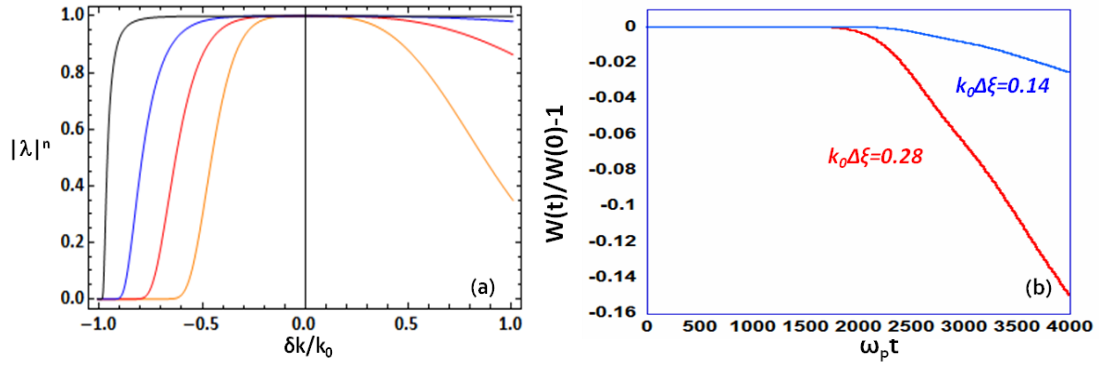


Figure 3.10 (a) $|\lambda|^n = |e^{-i\delta\omega\Delta t}|^n$ as a function of $\delta k/k_0$ with 3-point fitting method in the MPE solver. $1/k_0c\Delta t = 0.25$ and different $\Delta\xi$'s denoted by different colors for both red shift $\delta k/k_0 < 0$ and blue shift $\delta k/k_0 > 0$. The orange curve is for the $k_0\Delta\xi = 0.56$, red is $k_0\Delta\xi = 0.28$, blue is $k_0\Delta\xi = 0.14$, and black is $k_0\Delta\xi = 0.07$. (b) Action versus time with 3-point fitting method in the MPE solver produced by WAKE with $k_0\Delta\xi = 0.28$ (red) and $k_0\Delta\xi = 0.14$ (blue) simulating the Shadwick's 1D explicit simulation case.

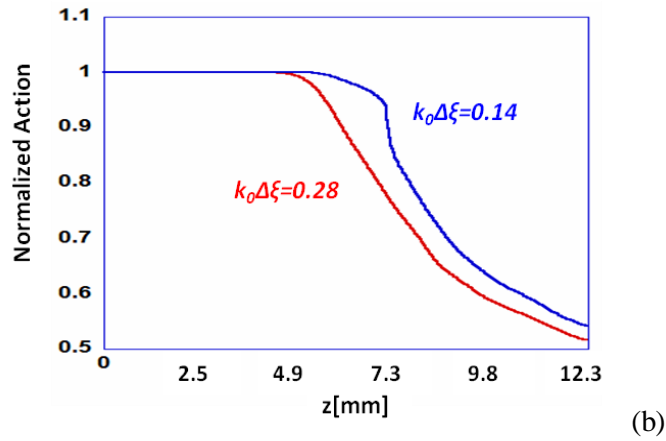
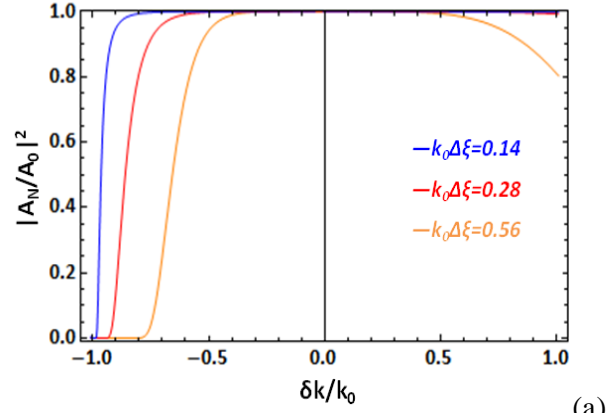
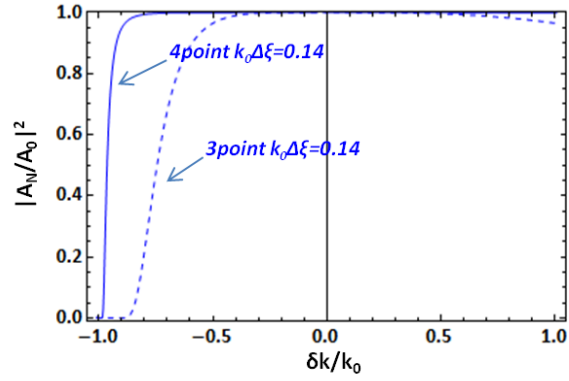
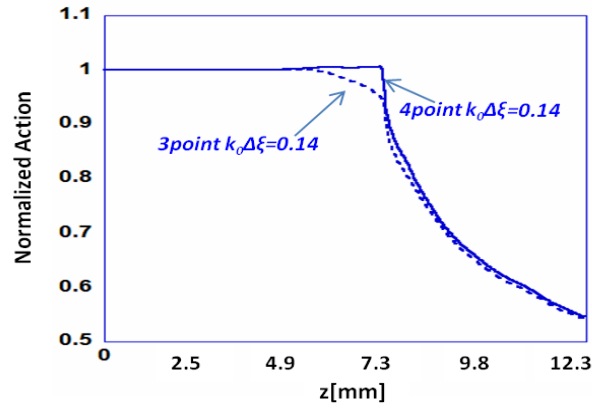


Figure 3.11 (a) $|A_N / A_0|^2$ as a function of $\delta k / k_0$ with 4-point fitting method in the FWE solver . $1 / k_0 c \Delta t = 0.028$ and different $\Delta \xi$'s denoted by different colors for both red shift $\delta k / k_0 < 0$ and blue shift $\delta k / k_0 > 0$. The orange curve is for the case $k_0 \Delta \xi = 0.56$, red is $k_0 \Delta \xi = 0.28$, blue is $k_0 \Delta \xi = 0.14$, and black is $k_0 \Delta \xi = 0.07$. (b) Action versus time with 4-point fitting method in the FWE solver produced by WAKE with $k_0 \Delta \xi = 0.28$ (red) and $k_0 \Delta \xi = 0.14$ (blue) simulating the UMD laser-plasma system.



(a)



(b)

Figure 3.12 (a) $|A_N / A_0|^2$ as a function of $\delta k / k_0$ with $1 / k_0 c \Delta t = 0.028$ and $k_0 \Delta \xi = 0.14$ for 3-point fitting method (dashed curve) and 4-point fitting method (solid curve). (b) Action versus time produced by WAKE with $k_0 \Delta \xi = 0.14$ for 3-point and 4-point fitting methods simulating the UMD laser-plasma system.

Chapter4: Pulsed Mid-infrared Radiation from Spectral Broadening in Laser Wakefield Simulations

4.1 Introduction

A short (<100 fs), intense ($>10^{17}$ W/cm²), optical laser pulse propagating through underdense ($n\sim 10^{18}$ /cm³) plasma ponderomotively excites plasma waves. Plasma electrons are pushed forward at the pulse front, repelled laterally in the body of the pulse, and converge on axis one plasma period later. As a result, the electron density increases at the front, decreases in the middle and can increase again at the back of the pulse. The density variations of the plasma wave provide a dynamic dielectric response that modifies the pulse spectrum [38,40-42]: the spectrum blue-shifts where the electron density is rising in time and red-shifts where the electron density is falling in time. For pulse durations commensurate with the plasma period, red-shifting dominates the spectral evolution and occurs where the body of the pulse sits in a region of falling electron density. The red-shifting can lead to a broadband spectrum extending well into the mid-infrared (MIR), wavelengths ranging from 3 to 7 microns, corresponding to 70-90% wavenumber shifting for a 800nm wavelength laser pulse, and whose properties are determined by those of the initial pulse and the plasma through which it propagates [47]. Because of its spectral proximity to the natural frequencies associated with molecular vibration, a tunable MIR source could be used to probe fundamental physical processes in liquids and materials or induce time-dependent structural changes in biological assemblies [47,48]. To this end, we investigate the parametric dependence of the conversion from optical to MIR energy in underdense plasma.

The extent of spectral shifting depends on the temporal gradient in the electron density and the distance over which the gradient is sustained [38,40-42,47]. The conversion to MIR thus relies critically on increasing and maintaining the ponderomotive force [24-26]. At low powers,

preformed plasma channels can provide radial confinement and maintain the ponderomotive force. At higher powers, the radial expulsion of electrons initially focuses the pulse and can result in a transient self-guiding structure: relativistic self-focusing and guiding [4,27-30]. Additionally, the local reduction in group velocity accompanying the red-shifting compresses the pulse [75,78-80]. Both nonlinear localization effects can enhance the ponderomotive force and consequently the electron density gradient. If the ponderomotive force is sufficient, complete cavitation of the electron density can occur and is often referred to as the ‘bubble regime’ [8-10].

Figure 4.1 illustrates the co-localization of the pulse and plasma wave. In the simulation a pulse with an initial wavelength of 800 nm, energy of 0.5 J, and duration of 30 fs is injected into a plasma of density $4.3 \times 10^{18} \text{ cm}^{-3}$. The top row display the laser pulse intensity and electron density as a function of radius r and moving frame coordinate $\xi = ct - z$, where c is the speed of light, initially and after 4.9 mm of propagation on the left and right respectively. At 4.9 mm the pulse has undergone significant transverse and temporal compression. The body of the pulse sits in a region where the electron density is falling in time and the region trailing the pulse is completely devoid of electrons. On the bottom row the corresponding Wigner distributions, representations of the local pulse spectrum, are plotted as a function of normalized wavenumber k/k_0 and ξ . The negative gradient in electron density along the pulse has resulted in the average pulse wavenumber dropping to nearly half its initial value, and the minimum wavenumber extending into the MIR.

The remainder of this chapter is organized as follows. Section 4.2 describes the ponderomotive guiding center, quasi-static plasma response model and the tenuous plasma, full wave equation (FWE) used in the simulations. In Sec. 4.3, the role of wave action conservation and pulse energy depletion in spectral shifting is discussed. Simulation results for pre-formed, fully ionized plasmas are presented in Sec. 4.4. In this section, we examine MIR generation for parameters relevant to the University of Maryland laser system, and examine the parametric

dependence of MIR energy on laser power, pulse length, and plasma density. Section 4.5 concludes the chapter with a summary of our results.

4.2 Plasma Response and Propagation Model

We adopt the ponderomotive guiding center, quasi-static, full wave equation model Eq. (4.1) (previously Eq. (1.7)) to describe the evolution of the plasma and laser pulse.

$$\left[\frac{2}{c} \frac{\partial}{\partial t} \left(ik_0 - \frac{\partial}{\partial \xi} \right) - \frac{1}{c^2} \frac{\partial^2}{\partial t^2} + \nabla_{\perp}^2 \right] \hat{A} = \frac{4\pi e^2}{m_e c^2} \left\langle \frac{\bar{n}_e}{\bar{\gamma}} \right\rangle \hat{A}, \quad (4.1)$$

where \bar{n}_e and $\bar{\gamma}$ are the average electron density and relativistic factor, e is the fundamental unit of charge, m_e is the electron mass, and the angular bracket signifies that an average over an ensemble of particles that stream through the plasma wake generated by the laser pulse is to be taken.

The model separates the electric and magnetic fields into fast and slow components. The fast evolution occurs on the time scale of the optical period, and the slow evolution on the time scale of the pulse duration or plasma period. The plasma electrons conserve canonical momentum in responding to the fast components, and respond on the slow time scale to both the slow components of the fields (the plasma wake) and the ponderomotive force associated with the laser pulse. The laser pulse envelope evolves on the slow time scale, responding to changes in the plasma density. On the fast time scale, the electric field is approximated as divergence free. The equations describing the separation of time scales are derived in Ref. 26 for the case of a slowly varying envelope description of the laser pulse. They have been updated in Chap.3 and are further expanded here to account for large shifts in the spectral content of the laser pulse.

We note that k_0 appearing in Eq. (4.1) is a reference wave number, and that the evolution of the vector potential \tilde{A}_{\perp} is unchanged by a transformation that shifts the value of k_0 and adds a wavenumber shift to the phase of the envelope. This is because the slowly varying plasma density

responds only to the magnitude of the envelope, \hat{A} . Thus, the validity of Eq. (4.1) does not require that the envelope be slowly varying on the scale of the initial wavelength, $|\partial\hat{A}/\partial\xi| \ll |k_0\hat{A}|$. However, the multiple time scale approach does require that the pulse envelope evolves slowly as it propagates $|(ik_0 - \partial/\partial\xi)\hat{A}| \gg |\partial\hat{A}/c\partial t|$. The advantage of retaining the second order time derivative and the numerical implementation of Eq. (4.1) are described in Chap.3.

4.3 Spectral Shifting in Tenuous Plasma

As a laser pulse propagates through plasma, it loses energy by exciting plasma waves [8,38,41,42, 81]. At the same time the laser pulse spectrum is modified. These processes are related to each other through the conservation of wave action. A consequence of the ponderomotive guiding center description of the plasma response is that the plasma current on the right hand side of Eq. (4.1) is proportional to, and in phase with, the vector potential. The rate of energy transferred to the electromagnetic wave can be calculated as the power the ponderomotive force does on the plasma current [81]. It follows from this that the action, as in Eq. (3.7),

$$I_L = \text{Re} \left\{ \int \frac{d^2x_\perp d\xi}{2\pi c} \hat{A}^* \left(k_0 + i \frac{\partial}{\partial\xi} + i \frac{\partial}{c\partial t} \right) \hat{A} \right\}, \quad (4.2)$$

is conserved [82]. We compare this quantity with twice the energy stored in the fast varying electric field, as in Eq. (3.8),

$$U_L = \int d^2x_\perp \int \frac{d\xi}{2\pi} \left| \left(k_0 + i \frac{\partial}{\partial\xi} \right) \hat{A}(\vec{x}_\perp, \xi, t) \right|^2 = \int d^2x_\perp \int dk k^2 |\bar{A}|^2, \quad (4.3)$$

representing the sum of the electric and magnetic field energies which are approximately equal.

The over bar denotes a Fourier transform with respect to ξ with the transform variable k ,

$$\bar{A}(\vec{x}_\perp, k, t) = \int d\xi \hat{A}(\vec{x}_\perp, \xi, t) e^{-ik\xi}. \quad (4.4)$$

A characteristic wavenumber, $\langle k \rangle$, can be defined and used to monitor spectral modification. In particular, we define an average wavenumber with respect to the spectral action density as

$$\langle k \rangle = \frac{\int d^2x_{\perp} \int dk k^2 |\bar{A}|^2}{\int d^2x_{\perp} \int dk k |\bar{A}|^2} \simeq \frac{U_L}{I}. \quad (4.5)$$

Equation (4.5) demonstrates that while the action is constant, the characteristic wavenumber must decrease in proportion to the pulse energy. An expression for the rate of energy depletion and accompanying spectral shifting can be derived when plasma waves are weakly excited. For an initial pulse envelope

$$\hat{A}(\vec{x}_{\perp}, \xi, t=0) = a_0 \sin(\pi\xi / 2c\tau) \exp(-r^2 / w^2) \quad (4.6)$$

defined on the interval $0 < \xi < 2c\tau$, where a_0 is the peak normalized vector potential of the laser field, w is the spot size, and τ the full width at half maximum (FWHM). The spectral shifting rate $\langle k \rangle^{-1} d\langle k \rangle / dz$ for linear plasma wave excitation is given by

$$\frac{1}{\langle k \rangle} \frac{d\langle k \rangle}{dz} = -\frac{1}{2\pi} \frac{1}{c\tau(k_0 w)^4} \left(\frac{P}{P_*} \right) \left[1 + \left(\frac{k_p w}{2} \right)^2 \right] \left[\frac{\sin(\omega_p \tau)}{1 - (\omega_p \tau / \pi)^2} \right]^2, \quad (4.7)$$

where $P[GW] \approx 21.5(a_0 w / \lambda)^2$, $P_* = 0.345 GW$, $\omega_p^2 = 4\pi e^2 n_e / m_e$, and $k_p = \omega_p / c$. The dependence of Eq. (4.7) on physical parameters can be explained as follows. By increasing the pulse power or decreasing the spot size, the work done by the laser pulse on the plasma increases through an enhanced ponderomotive force. For small pulse length, $\omega_p \tau < 1$, the shifting rate is proportional to pulse length as the ponderomotive force is active over an extended duration and performs more work on the plasma. At $\omega_p \tau \sim 2$, the spectral shifting rate is maximized due to the weak resonance associated with matching the pulse length to the plasma period. Increasing

the pulse length beyond $\omega_p \tau \sim 2$ provides additional pulse energy but weakens the longitudinal ponderomotive force, diminishing the shifting rate.

While Eq. (4.7) provides some qualitative insight on the parametric dependence of the shifting rate, its quantitative predictive capability is limited. Figure 4.2 shows the characteristic wavenumber as a function of distance for a 17 TW, 40 TW, and 60 TW, laser pulse propagating in a plasma channel with on axis density $4.3 \times 10^{18} \text{ cm}^{-3}$. The pulse was initialized with a wavelength of 800 nm, temporal FWHM of 30 fs, and a spot size of 25 μm matched to the plasma density's radial parabolic profile [83]. The reduced group velocity accompanying the red-shifting causes the radiation to slide backwards in the moving frame coordinate, ξ . Each curve terminates when the radiation reaches the simulation boundary in ξ of 288 fs. The rate of spectral red-shifting increases with power, but the wavenumber does not drop linearly with distance as predicted by Eq. (4.7). The inset displays a comparison of Eq. (4.7) with the simulation results for the initial stage of propagation. For the comparison, Eq. (4.7) has been corrected with the effective relativistic mass increase contributed by the electron quiver energy ($\omega_p \rightarrow \omega_p / [1 + 2a_0^2]^{1/4}$). For lower powers and short propagation distances, the linear theory matches the simulations well. The onset of pulse self-focusing and compression, and electron cavitation result in the deviation between theory and simulation for higher powers and longer propagation distances. Furthermore, as seen in Figs. 4.1 and 4.2, the characteristic wavenumber cannot diagnose the spectral range of the pulse. The characteristic wavenumber for the 17 TW pulse in Fig. 4.2 terminates at $\langle k \rangle / k_0 \sim 0.5$ corresponding to $\lambda \sim 1.6 \mu\text{m}$, while in Fig. 4.1 the spectral range for the same power extends below $k / k_0 \sim 0.2$, $\lambda \sim 4 \mu\text{m}$. These strongly shifted components of the pulse represent the MIR radiation, wavelengths from 3 to 7 μm .

4.4 Simulation Results

4.4.1. Observation of MIR

We first examine the conversion of spectral energy into the mid-IR for parameters relevant to the current laser-plasma capabilities at the University of Maryland. A laser pulse with an initial wavelength 800 nm, spot size 25 μm , temporal FWHM 30 fs and power 17 TW (normalized vector potential $a_0 = 0.45$), is injected into a plasma channel with an on axis electron density of $4.3 \times 10^{18} \text{ cm}^{-3}$ and propagates over a total distance of 12.3 mm. The corresponding critical power for self-focusing, $P_{cr} = 17(\omega/\omega_p)^2 \text{ GW}$, is 7 TW. In Fig. 4.3, the spectral energy density, the integrand of Eq. (4.3), is plotted as a function of normalized wavenumber, k/k_0 , at propagation distances of $z = 0, 2.46, 4.94$ and 7.9 mm, represented by the color red, grey, dark grey and black respectively. For reference, the pulse energy has dropped to 55% of the initial energy by 7.9 mm. The spectral density is broadened and red shifted as the pulse propagates. At 7.9 mm, the spectral intensity extends to wavelengths longer than $4.7 \mu\text{m}$ (red arrow).

The blue curve in Fig. 4.3 displays the spectral density at $z = 7.9$ mm when the pulse propagates through a uniform plasma (no pre-formed channel). In spite of surpassing the self-focusing condition, $P/P_{cr} = 2.4$, the pulse diffracts in the uniform plasma, limiting the spectral broadening and MIR energy. At 17 TW, the radial confinement provided by pre-formed channel maintains the pulse intensity over an extended distance, allowing additional spectral broadening and increasing the mid-IR energy.

Figure 4.4 displays the cumulative energy U_C [mJ] as a function of k/k_0 at distances of $z = 0, 2.46, 4.94$ and 7.9 mm in a plasma channel and at $z = 7.9$ mm in a uniform plasma demarcated by the colors red, grey, dark grey, black and blue respectively. The cumulative energy, the integral of the spectral energy density up to k , represents the energy contained in wavenumbers less than or equal to k . Wavelengths longer than $4.7 \mu\text{m}$ (red arrow) account for 15 mJ after 7.9 mm of propagation in the plasma channel (black) with a conversion efficiency from the initial pulse

energy of 2.9%. Without a preformed channel (blue), the conversion efficiency is zero for wavelengths longer than 2.5 μm .

Figure 4.5 (a) is the radially averaged intensity profile of the MIR pulse found by spectrally filtering in the range $0 < k < 0.2k_0$ as a function of ξ and z . The MIR pulse appears at a propagation distance near 7.9 mm consistent with Figs. 4.3 and 4.4 with a temporal FWHM of 30 fs or two cycles of 4.7 μm light. The MIR pulse gradually lengthens due to group velocity dispersion, and quickly falls back in ξ due to the smaller group velocities associated with the longer wavelengths. Although the MIR pulse moves backwards in the speed of light frame, it continues to propagate in the forward direction. Figures 4.5 (b) and (c) display the filtered MIR pulse as a function of r and ξ at $z = 7.9$ and 8.4 mm respectively. The pulse undergoes some diffractive spreading but remains mostly confined within the preformed channel. This is a result of the plasma channel guiding condition being independent of frequency. After the spectrally broadened pulse has left the channel, a long wave pass filter can be applied to extract the MIR radiation.

4.4.2. Parametric Dependence of MIR Energy Generation

Maximization of the MIR energy is essential for its use in applications. To this end, we now investigate the parametric dependence of energy conversion to MIR on initial pulse power, pulse duration, and plasma density. Because the spectral shifting rate depends on all of these parameters, all results are plotted at the distance where the characteristic wavenumber shift, Eq. (4.5), is maximized. All scalings are performed in a plasma channel with matched spot size of 25 μm unless otherwise state. The overall trend is that MIR efficiency increases with the ponderomotive force up to electron cavitation where the efficiency saturates.

The pulse power at fixed pulse length is varied through the laser pulse amplitude while the other parameters remain unchanged from Sec. 4.4.1. Figure 4.6 (a) shows the cumulative energy U_C [mJ] as a function of k/k_0 for initial powers of 40 TW, black line, and 17 TW, grey line,

with and without a channel, the solid and dashed lines respectively. The larger pulse powers clearly increase the energy content in the MIR range. As discussed above, the pre-formed channel keeps the 17 TW pulse radially confined extending the distance over which the pulse undergoes spectral broadening. At 40 TW, $P / P_{cr} = 5.7$, self-focusing ensures radially confinement of the pulse and the pre-formed channel is no longer required: the cumulative MIR energy resulting from channeled and non-channeled propagation is nearly identical.

Figure 4.6 (b) displays the conversion efficiency, the cumulative energy U_C divided by the initial laser pulse energy, as a function of initial laser pulse power for the wavelength ranges $\lambda \geq 6 \mu\text{m}$, $\lambda \geq 4 \mu\text{m}$ and $\lambda \geq 2 \mu\text{m}$. The efficiency exhibits a threshold behavior with power. The weak power dependence of efficiency above threshold results from relativistic mass increases to the electrons, nonlinear laser pulse evolution, and saturation of the index of refraction gradient through electron cavitation. The electron quiver momentum and consequently the effective mass increase with power. A larger ponderomotive force is required for the same displacement in electron density. As a result, the scaling of electron density gradient with pulse power weakens as power is increased: $\partial_{\xi} n_e \propto P$ for $a_0 \ll 1$ and $\partial_{\xi} n_e \propto P^{1/2}$ for $a_0 \gg 1$.

For the density considered, the critical power for self-focusing is $P_{cr} = 7 \text{ TW}$. The 17 TW and 40 TW pulses undergo stronger nonlinear self-focusing, which increases the ponderomotive force. In addition to transverse compression, spectral broadening of the pulses causes self-steepening or temporal compression. The group velocity decreases as the wavelength increases in a plasma, so that initial red-shifting at the front of the pulse causes pulse energy to coalesce at the back of the pulse. The enhanced amplitude and reduced pulse length both contribute to an increased ponderomotive force. As the pulse becomes radially and temporally localized, the ponderomotive force expels an increasing number of electrons. Eventually the ponderomotive force is large enough to expel all the electrons, cavitation. Further increasing the power causes

cavitation earlier in the pulse, but at the same time reduces the temporal region of the pulse that undergoes spectral broadening.

To examine the dependence on pulse length, we fix the pulse energy at 0.5 J. For comparison with the previous case, this can be considered a power scaling at fixed energy. As before the on-axis plasma density is $4.3 \times 10^{18} \text{ cm}^{-3}$ corresponding to a resonant FWHM $\tau_R = \pi / \omega_p = 27 \text{ fs}$. Figure 4.7 shows the conversion efficiency as a function of initial pulse length for the wavelength ranges: $\lambda \geq 6 \mu\text{m}$, $\lambda \geq 4 \mu\text{m}$ and $\lambda \geq 2 \mu\text{m}$. The conversion efficiency drops with increasing pulse length. As discussed above, for pulse durations longer than the resonant FWHM, the longitudinal ponderomotive force weakens with increasing pulse length. Additionally, the initial power is decreased as pulse length is increased: $P \sim 1 / \tau$. The drop in power weakens both components of the ponderomotive force. A reduced ponderomotive force provides less charge displacement, a smaller index gradient, and less spectral broadening. The dashed lines above and below the $\lambda \geq 2 \mu\text{m}$ curve illustrate the minor effect of adding a negative and positive chirp respectively. For each pulse duration, the chirp is calculated assuming a 30 fs bandwidth limited pulse.

We now consider the dependence of MIR generation on the on-axis plasma density. The laser power and temporal FWHM are fixed at 17 TW and 30 fs respectively. The resonant density, defined by $\omega_p = \pi / \tau$, is initially $3.4 \times 10^{18} \text{ cm}^{-3}$. Figure 4.8 shows the conversion efficiency as a function of plasma density for the wavelength ranges $\lambda \geq 6 \mu\text{m}$, $\lambda \geq 4 \mu\text{m}$ and $\lambda \geq 2 \mu\text{m}$. The critical power varies from 10 TW at $3 \times 10^{18} \text{ cm}^{-3}$ to 4.6 TW at $6.5 \times 10^{18} \text{ cm}^{-3}$. The increase in efficiency from $3 \times 10^{18} \text{ cm}^{-3}$ to $3.4 \times 10^{18} \text{ cm}^{-3}$ for $\lambda \geq 2 \mu\text{m}$ can be attributed to the enhanced plasma wave amplitude at the resonant density. As the density is increased, the drop in critical power provides additional self-focusing and an enhanced ponderomotive force, more charge displacement, and increased spectral broadening observable in the increased efficiency for $\lambda \geq 4 \mu\text{m}$ and $\lambda \geq 6 \mu\text{m}$.

As a final note we compare the cumulative energies resulting from the FWE and MPE solvers for a 30fs, 40 TW pulse propagating in a plasma channel with on axis density $4.3 \times 10^{18} \text{ cm}^{-3}$. Figure 4.9 shows the fractional difference in cumulative energies U_C resulting from the two approaches $((U_{\text{cFWE}} - U_{\text{cMPE}})/U_{\text{cFWE}})$. The discrepancy in the cumulative energy is largest where the discrepancy in the dispersion is also large: below $k/k_0 = .10$ (see Fig. 3.1 in Chap 3). The MPE over and under predicts the energy below and above $k/k_0 = .10$ respectively. At values of $k/k_0 > .2$, the dispersion for both solvers is accurate and the fractional difference plateaus at a value representing the difference in pulse energy lost.

4.5 Conclusions

We have investigated the generation of MIR radiation from spectral broadening of high intensity, ultrashort laser pulses propagating through tenuous plasma. The ponderomotive guiding center, quasi-static, full wave equation model was adopted to simulate the laser pulse and plasma evolution. The conversion of optical energy to the MIR was examined as a function of laser pulse power, pulse length, and plasma density. The predominant trend was for the conversion efficiency to increase with the ponderomotive force up to the point of electron cavitation where the efficiency saturated. The simulations show 1% conversion to MIR energy at wavelengths longer than 6 microns for laser powers greater than 20 TW.

4.6 Appendix: Scaling of the Characteristic Wavenumber Shift

It has been discussed in Sec. 4.3 that the change of the field energy U_L is equal to the rate at which the ponderomotive force $\vec{F}_p \sim -\vec{\nabla}V_p$ does work to the plasma current \vec{J} [81],

$$\frac{dU_L}{dt} = P_F, \quad (4.8)$$

where V_p is the ponderomotive potential taken the time average of the vector potential \vec{A} ,

$$V_p = \frac{mc^2}{2} \left\langle \left(\frac{qA^2}{mc^2} \right)^2 \right\rangle_T ; P_F \text{ can be defined as } P_F = \int d^3x \vec{F} \cdot \vec{J} / q . \text{ That gives}$$

$P_F = \int d^3x V_p \frac{\partial}{\partial t} \tilde{n}$, where \tilde{n} is the perturbed electron density. In the limit of a weak ponderomotive potential, \tilde{n} satisfies a 'linear inhomogeneous equation' [81],

$$\frac{\partial^2}{\partial t^2} \tilde{n} + \omega_p^2 \tilde{n} = \frac{n_0}{m} \nabla^2 V_p . \quad (4.9)$$

Pulse intensity also depends on \vec{A} ,

$$I = \frac{c}{4\pi} \left(\frac{\omega}{c} \right)^2 \langle \vec{A} \rangle_T = P_* 4 \left(\frac{\omega}{c} \right)^2 \left(\frac{V_p}{mc^2} \right), \quad (4.10)$$

where ω_0 is the central frequency and $P_* = \frac{c}{8\pi} \left(\frac{mc^2}{q} \right) = 0.345GW$. Note that I or V_p can be

written as the peak value times the spatial and temporal dependent terms,

$$\begin{aligned} I &= I_0 \sin^2(\pi t / 2\tau) \exp(-2r^2 / w^2) \\ &= P_* 4 \left(\frac{\omega_0}{c} \right)^2 \left(\frac{V_{p0}}{mc^2} \right) \sin^2(\pi t / 2\tau) \exp(-2r^2 / w^2) . \end{aligned} \quad (4.11)$$

Peak power can be obtained by integrating intensity over r,

$$P = \int_0^\infty 2\pi r dr I(r, t = \tau) = 2\pi P_* \left(\frac{V_{p0}}{mc^2} \right) \left(\frac{\omega_0 w}{c} \right)^2 . \quad (4.12)$$

Laser energy U_L can be obtained from integration over one pulse period,

$$\begin{aligned} U_L &= \int_0^T dt P = \int_0^\infty 2\pi r dr I(r, t = \tau) \int_0^{2\tau} dt \sin^2(\pi t / 2\tau) \\ &= P\tau = 2\pi P_* \left(\frac{V_{p0}}{mc^2} \right) \left(\frac{\omega_0 w}{c} \right)^2 \tau . \end{aligned} \quad (4.13)$$

On the other hand, it's shown from Ref. 81 Eq. (6) that the rate at which the ponderomotive force does work to the plasma waves is

$$P_F = P_* \frac{v_g}{c} \int 2\pi r dr \left[\frac{\omega_p^2}{v_g^2} \left| \frac{\omega_p \bar{V}_p}{mc^2} \right|^2 + \left| \nabla_{\perp} \frac{\omega_p \bar{V}_p}{mc^2} \right|^2 \right], \quad (4.14)$$

where v_g is the group velocity of the laser pulse and $\bar{V}_p = \bar{V}_p(r, \omega)$ is the Fourier component of the ponderomotive potential. Integrating over space gives

$$P_F = \pi P_* \frac{v_g}{c} \left| \frac{\omega_p \bar{V}_{p0}}{mc^2} \right|^2 \left[1 + \left(\frac{\omega_p w}{2v_g} \right)^2 \right], \quad (4.15)$$

where $\left| \frac{\omega_p \bar{V}_{p0}}{mc^2} \right|^2 = \left| \frac{V_{p0}}{mc^2} \right|^2 \left| \frac{\sin(\omega_p \tau)}{1 - (\omega_p \tau / \pi)^2} \right|^2$ is from the temporal dependence of pulse intensity Eq.

(4.11).

Scaling of the average spectral shifting rate can be derived from Eq. (4.5),

$$\frac{1}{\langle k \rangle} \frac{d \langle k \rangle}{dt} = \frac{1}{U_L} \frac{dU_L}{dt} = \frac{P_F}{U_L}, \quad (4.16)$$

where Eq. (4.8) has been applied. From Eq. (4.13), (4.15) and assume $v_g \sim c$, this yields Eq. (4.7)

$$\frac{1}{\langle k \rangle} \frac{d \langle k \rangle}{dz} = -\frac{1}{2\pi} \frac{1}{c\tau(k_0 w)^4} \left(\frac{P}{P_*} \right) \left[1 + \left(\frac{k_p w}{2} \right)^2 \right] \left[\frac{\sin(\omega_p \tau)}{1 - (\omega_p \tau / \pi)^2} \right]^2. \quad (4.7)$$

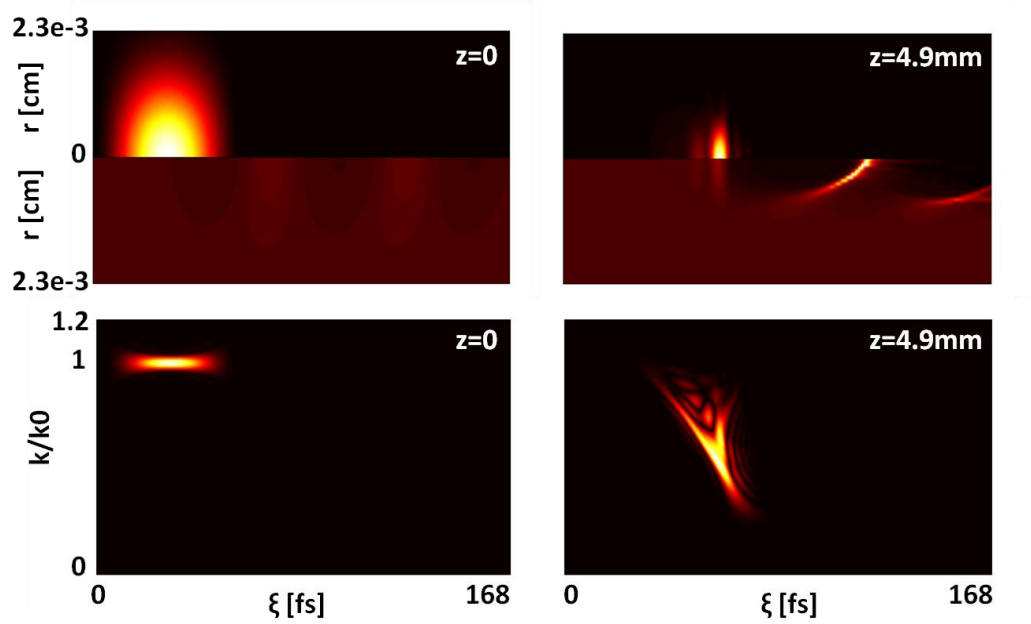


Figure 4.1 Top: laser intensity and electron density as functions of channel radius r and ξ at propagation distances of $z = 0.0$, left, and 4.9 mm, right. Bottom: Wigner distributions of the laser pulse as a function of normalized wavenumber and ξ at the same propagation distances.

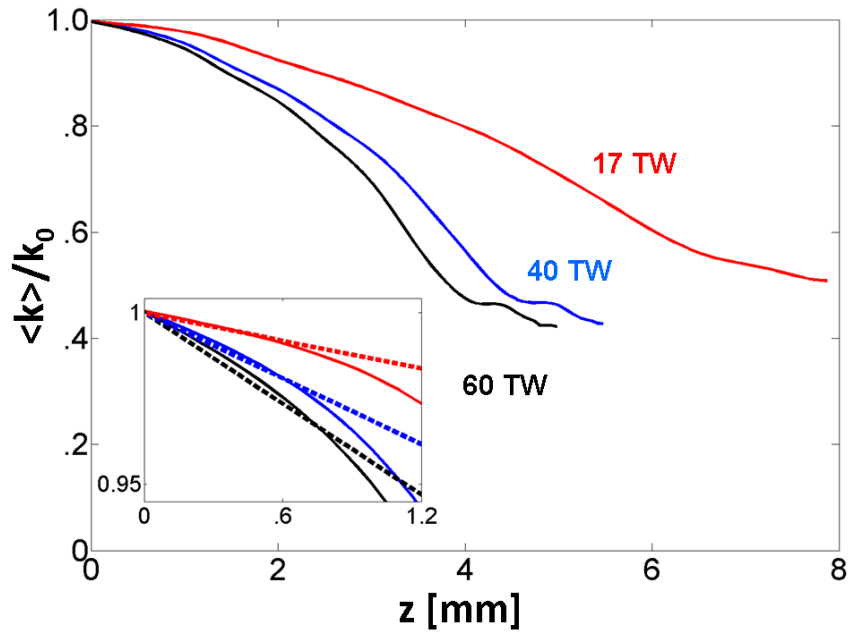


Figure 4.2 Characteristic wavenumber $\langle k \rangle / k_0$ as a function of distance z for initial pulse powers of 17, 40 and 60 TW, represented by red, blue and black respectively. The inset shows a comparison with linear theory (dashed lines) for each case.

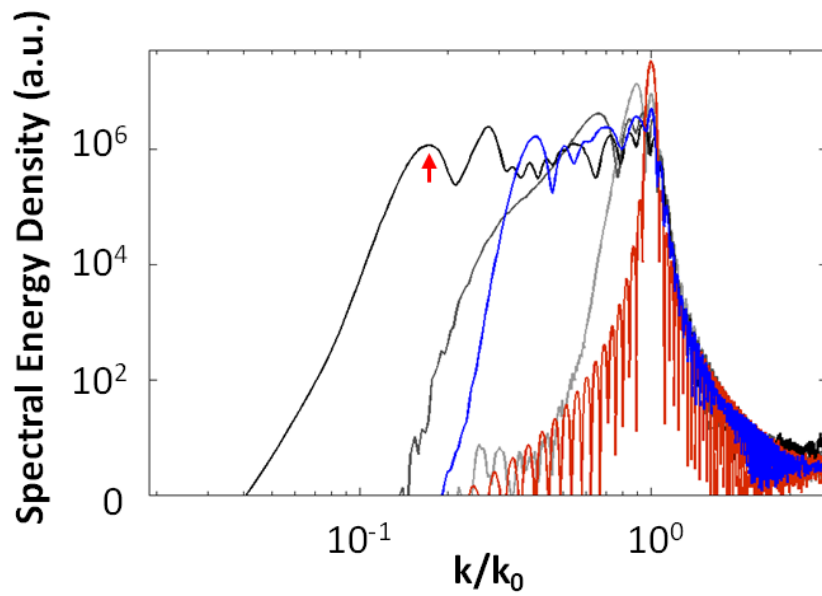


Figure 4.3 Spectral energy density of a pulse propagating in a plasma channel as a function of k/k_0 at distances $z=0, 2.5, 4.9$ and 7.9 mm, represented by the red, grey, dark grey and black lines respectively; spectral energy density for a pulse propagating through a uniform plasma (no channel) is represented by the blue curve. The red arrow indicates where $\lambda=4.7$ μm .

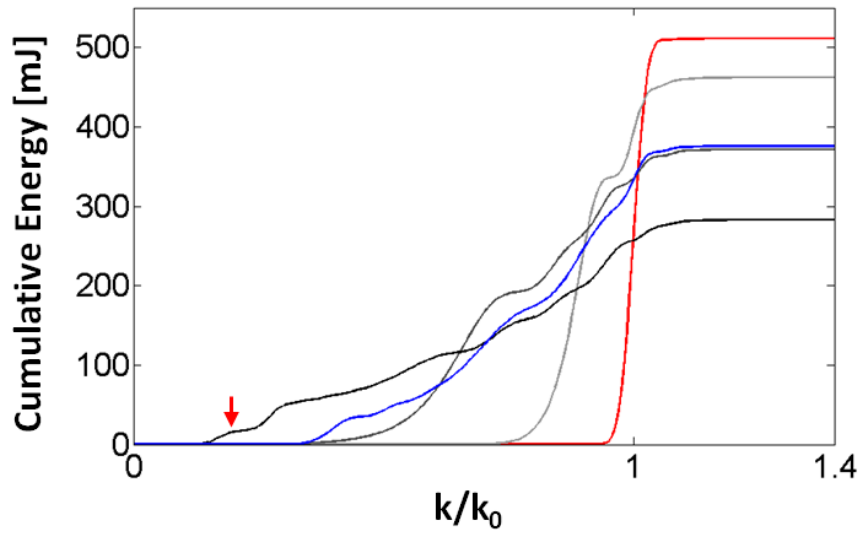


Figure 4.4 Cumulative energy as a function of k/k_0 at distances $z=0, 2.5, 4.9$ and 7.9 mm, represented by the red, grey, dark grey and black curves respectively; cumulative energy for the no channel case at $z=7.9$ mm represented by the blue curve . The red arrow indicates there are 15mJ of cumulative energy at $\lambda=4.7 \mu\text{m}$.

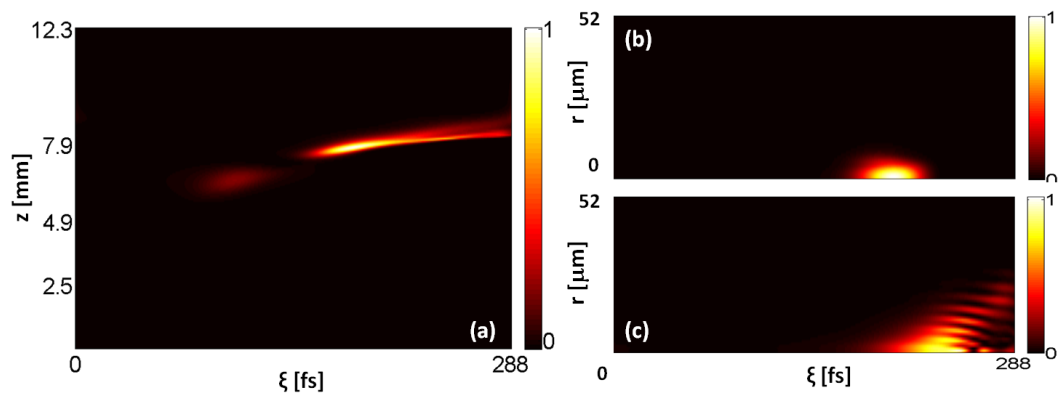


Figure 4.5 (a) Retrieved profile of the filtered mid-ir pulse ($0 < k < 0.2k_0$) radially averaged intensity as a function of (z, ξ) . (b)(c) Filtered mid-ir pulse ($0 < k < 0.2k_0$) as a function of (r, ξ) at distances $z = 7.9$ and 8.4 mm.

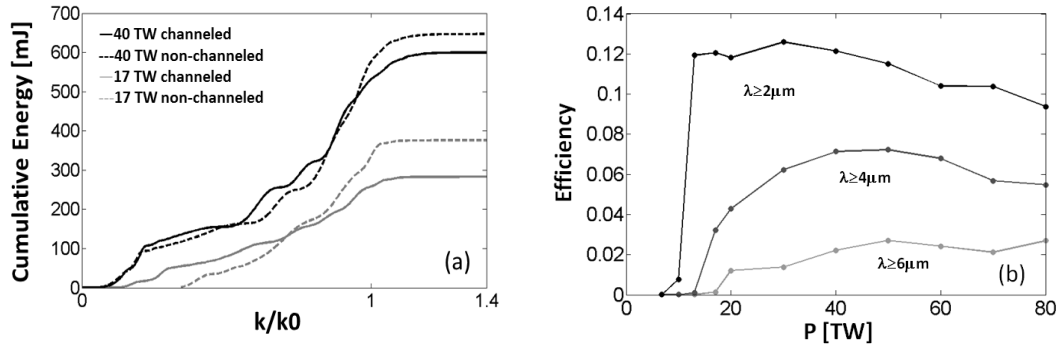


Figure 4.6 (a) Cumulative energy at largest characteristic wavenumber shift as a function of k/k_0 for initial powers $P = 40$ TW for the channeled (black, solid) and non-channeled (black, dashed) cases and 17 TW for the channeled (grey, solid) and non-channeled (grey, dashed) cases. (b) Mid-IR generation efficiency as a function of initial pulse power for $\lambda \geq 6 \mu\text{m}$, $\lambda \geq 4 \mu\text{m}$ and $\lambda \geq 2 \mu\text{m}$.

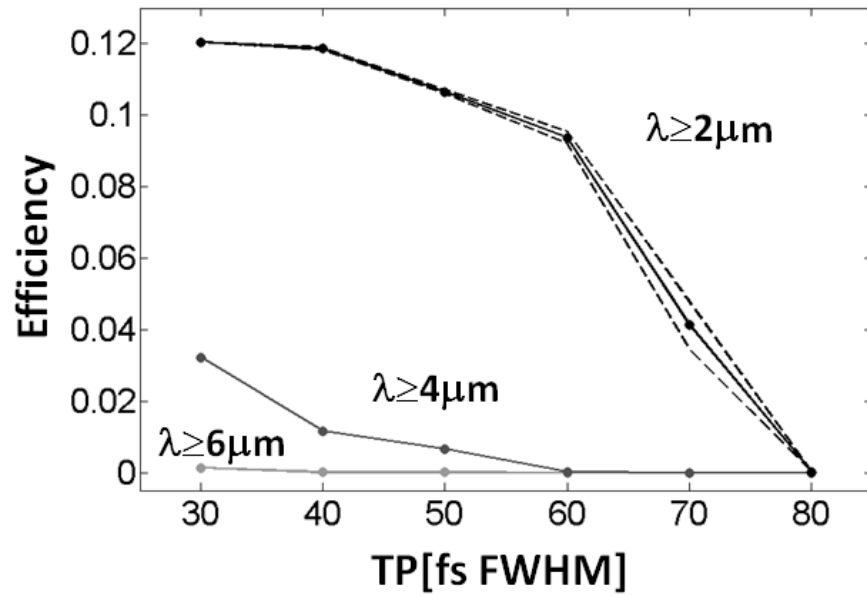


Figure 4.7 MIR conversion efficiency in the ranges $\lambda \geq 6\mu\text{m}$, $\lambda \geq 4\mu\text{m}$ and $\lambda \geq 2\mu\text{m}$ as a function of initial temporal FWHM. The upper and lower dashed lines show the effect of negative and positive chirp respectively.

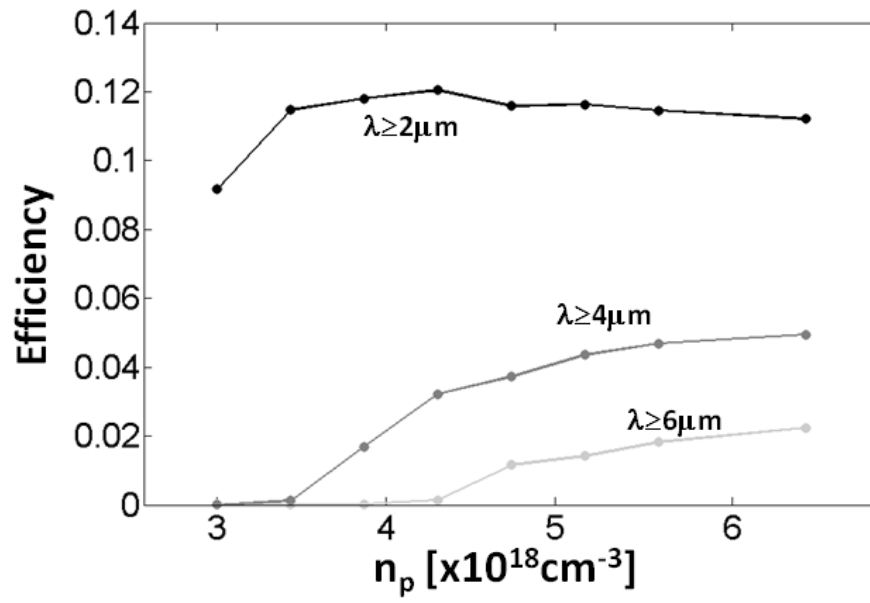


Figure 4.8 MIR conversion efficiency in the ranges $\lambda \geq 6 \mu\text{m}$, $\lambda \geq 4 \mu\text{m}$ and $\lambda \geq 2 \mu\text{m}$ as a function of on-axis plasma density.

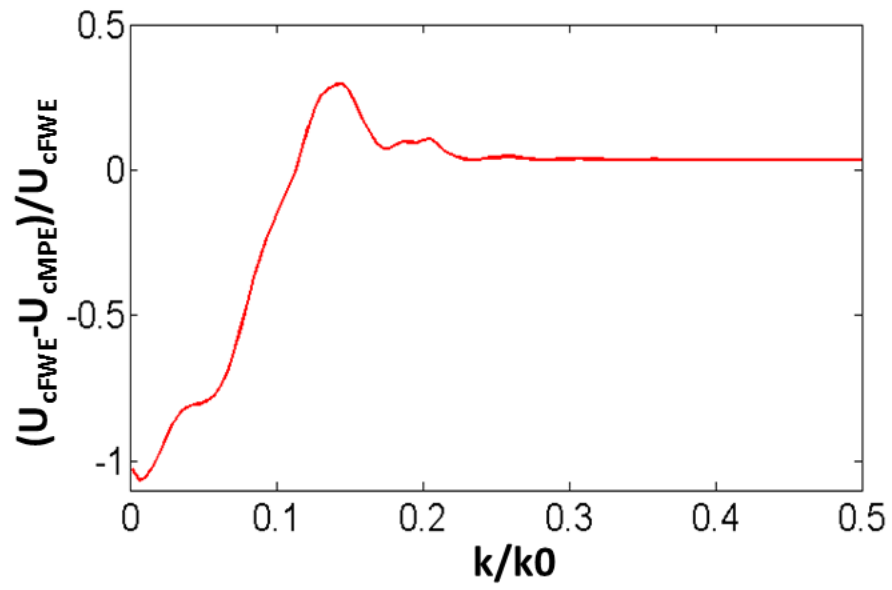


Figure 4.9 Fractional difference in cumulative energies resulting from FWE and MPE approaches $((U_{cFWE} - U_{cMPE}) / U_{cFWE})$ as a function of k/k_0 for a 30fs, 40 TW pulse propagating in a plasma channel.

Chapter5: Summaries

We have studied the spectral broadening of intense laser pulses propagating in plasma for parameters relevant to Laser Wake Field Acceleration. The studies were carried out using the two-dimensional simulation code WAKE, which makes a number of approximations that enable efficient calculation. Pulse evolution, energy depletion, conservation of action and spectral modification were closely investigated. Several measures of spectral diagnostics were considered including the Fourier spectrum, the rate of change of the envelope phase, and the Wigner function. Simulations of the 2006 LBNL experiments [18], the pulse compression experiments from Schreiber, *et al.* [75], and the explicit one dimensional simulations from Shadwick, *et al.* [41] were performed and compared. Results of the simulations verified that spectra were substantially modified for all three cases, and that the spectral changes and energy depletion were consistent with action conservation: for pulses causing complete cavitation, large wavenumber shifts $\delta k / k_0 = .80$ were observed for propagation to a distance where 40% -50% of the pulse energy is depleted. The extended paraxial equation (modified paraxial equation-MPE) conserves action up to this distance.

We have implemented a full time-space D'Alembertian in the laser field evolution equation (enveloped full wave equation-FWE) in WAKE. It has the following advantages: first, this solver has its own conserved action up till the distance where large wavenumber shift $\delta k / k_0 = .80$ happens; second, it has the advantage of better predicting the dispersion relation and eliminating the problematic divergence in the dispersion of the modified paraxial solver as wavenumber approaches zero, which is important especially when considering long wavelength generation.

Numerical analysis has been conducted through simulation results for parameters relevant to the current laser-plasma capabilities at the University of Maryland for both FWE and MPE

solvers. The results that we find for pulse evolution, energy depletion, and spectral modification are remarkably similar to those previously studied three cases from Ref. 18,41,75. The accuracy of calculation is monitored by observing the time dependence of wave action. When a large spectral shift $\delta k / k_0 = .80$ or complete cavitation occurs, action subsequently decays due to numerical damping and slowing down of the group velocities of the laser pulse, which propagates out of the simulation domain quickly. Numerical damping can be minimized by a combination of high resolution in ξ and higher order evaluation of ξ derivatives. Action does still decay after minimizing numerical damping, but due to convection out of the simulation domain, we conclude that WAKE is an accurate tool for studying energy depletion and spectral broadening in intense laser-plasma interactions.

Generation of MIR radiation from the process of spectral broadening of high intensity, ultrashort laser pulses propagating through tenuous plasmas has also been studied. The ponderomotive guiding center, quasi-static, full wave equation model was adopted to simulate the laser pulse and plasma evolution. The conversion of optical energy to the MIR was examined as a function of initial laser pulse power, pulse length, and plasma density. The predominant trend was for the conversion efficiency to increase with the ponderomotive force up to the point of electron cavitation where the efficiency saturated. The simulations show 2% conversion to MIR energy at wavelengths longer than 6 microns for laser powers greater than 20 TW.

Bibliography

- [1] T. Tajima and J. M. Dawson, *Phys. Rev. Lett.* 43, 267 (1979).
- [2] L. P. Gorbunov and V. I. Kirsanov, *Sov. Phys. JETP* 66, 290 (1987).
- [3] P. Sprangle, E. Esarey, A. Ting, and G. Joyce, *Appl. Phys. Lett.* 53, 2146 (1988).
- [4] E. Esarey, P. Sprangle, J. Krall, A. Ting, and G. Joyce, *Phys. Fluids B* 5, 2690 (1993).
- [5] W. P. Leemans, and E. Esarey, *Phys. Today* 62, 44 (2009).
- [6] C. B. Schroeder, E. Esarey, C. G. R. Geddes, C. Benedetti, and W. P. Leemans, *Phys. Rev. ST Accel. Beams* 13, 101301 (2010).
- [7] A. J. Gonsalves, et al., *Nature Physics* 7, 862–866 (2011).
- [8] W. Lu, M. Tzoufras, and C. Joshi, *Phys. Rev. ST Accel. Beams* 10, 061301 (2007).
- [9] A. Pukhov and J. Meyer-ter-vehn, *Appl. Phys. B* 74, 355 (2002).
- [10] I. Kostyukov, A. Pukhov, and S. Kiselev, *Phys. Plasmas* 11, 5256 (2004).
- [11] S. P. D. Mangles, C. D. Murphy, Z. Najmudin, A. G. R. Thomas, J. L. Collier, A. E. Dangor, E. J. Divall, P. S. Foster, J. G. Gallacher, C. J. Hooker, D. A. Jaroszynski, A. J. Langley, W. B. Mori, P. A. Norreys, F. S. Tsung, R. Viskup, B. R. Walton and K. Krushelnick, *Nature* 431, 535 (2004).
- [12] J. Faure, Y. Glinec, A. Pukhov, S. Kiselev, S. Gordienko, E. Lefebvre, J.-P. Rousseau, F. Burgy, and V. Malka, *Nature* 431, 541(2004).
- [13] C. G. R. Geddes, C. Toth, J. van Tilborg, E. Esarey, C. B. Schroeder, D. Bruhwiler, C. Nieter, J. Cary, and W. P. Leemans, *Nature* 431, 538 (2004).
- [14] B. Hidding, K.-U. Amthor, B. Liesfeld, H. Schwöere, S. Karsch, M. Geissler, L. Veisz, K. Schmid, J. G. Gallacher, S. P. Jamison, D. Jaroszynski, G. Pretzler, and R. Sauerbrey, *Phys. Rev. Lett.* 96, 105004 (2006).
- [15] T. Hosokai, K. Kinoshita, T. Ohkubo, A. Maekawa, M. Uesaka, A. Zhidkov, A. Yamazaki, H. Kotaki, M. Kando, K. Nakajima, S. V. Bulanov, P. Tomassini, A. Giulietti, and D. Giulietti, *Phys. Rev. E* 73, 036407 (2006).
- [16] A. Maksimchuk, S. Reed, S. S. Bulanov, V. Chvykov, G. Kalintchenko, T. Matsuoka, C. McGuffey, G. Mourou, N. Naumova, J. Nees, P. Rousseau, V. Yanovsky, K. Krushelnick, N. H. Matlis, S. Kalmykov, G. Shvets, M. C. Downer, C. R. Vane, J. R. Beene, D. Stracener, and D. R. Schultz, *Phys. Plasmas* 15, 056703 (2008).

- [17] J. Osterhoff, A. Popp, Zs. Major, B. Marx, T. P. Rowlands-Rees, M. Fuchs, M. Geissler, R. Hürlein, B. Hidding, S. Becker, E. A. Peralta, U. Schramm, F. Grüner, D. Habs, F. Krausz, S. M. Hooker, and S. Karsch, *Phys. Rev. Lett.* 101, 085002 (2008).
- [18] W. P. Leemans, B. Nagler, A. J. Gonsalves, C. Tóth, K. Nakamura, C. G. R. Geddes, E. Esarey, C. B. Schroeder, and S. M. Hooker, *Nature Physics* 2, 696 (2006).
- [19] K. Nakamura, B. Nagler, C. Tóth, C. G. R. Geddes, C. B. Schroeder, E. Esarey, W. P. Leemans, A. J. Gonsalves, and S. M. Hooker, *Phys. Plasmas* 14, 056708 (2007).
- [20] X. Wang, R. Zgadzaj, N. Fazel, S. A. Yi, X. Zhang, W. Henderson, Y.-Y. Chang, R. Korzekwa, H.-E. Tsai, C.-H. Pai, Z. Li, H. Quevedo, G. Dyer, E. Gaul, M. Martinez, A. Bernstein, T. Borger, M. Spinks, M. Donovan, S. Y. Kalmykov, V. Khudik, G. Shvets, T. Ditmire and M. C. Downer, “Petawatt-laser-driven wakefield acceleration of electrons to 2 GeV in 1017cm-3 plasma”, *AIP Conf. Proc.* 1507, 341(2012).
<http://arxiv.org/ftp/arxiv/papers/1307/1307.4159.pdf>.
- [21] A. J. Gonsalves, K. Nakamura, C. Lin, D. Panasencko, S. Shiraishi, T. Sokollik, C. Benedetti, C. B. Schroeder, C. G. R. Geddes, J. van Tilborg, J. Osterhoff, E. Esarey, Cs. Tóth, and W. P. Leemans, “Injection and Staging for Laser Plasma Accelerators”, *AIP Conf. Proc.* 1507, 67 (2012).
- [22] http://cilexsaclay.fr/en/Phocea/Vie_des_labos/Ast/ast_service.php?id_unit=18.
- [23] <http://www.lbl.gov/Community/BELLA/>.
- [24] W. L. Kruer, *The Physics of Laser Plasma Interactions* (Addison-Wesley, Redwood City, Cal. 1988), p. 39.
- [25] E. Esarey, C. B. Schroeder, and W. P. Leemans, *Review of Modern Physics* 81 (2009).
- [26] P. Mora, T. M. Antonsen, *Phys. Plasmas* 4, 217 (1997).
- [27] J. E. Ralph, K. A. Marsh, A. E. Pak, W. Lu, C. E. Clayton, F. Fang, W. B. Mori, and C. Joshi, *Phys. Rev. Lett* 102, 175003 (2009).
- [28] G. Sun, E. Ott, Y. C. Lee, and P. Guzdar, *Phys. Fluids* 30 (2), 526 (1987).
- [29] T. Kurki-Suonio, P. J. Morrison, and T. Tajima, *Phys. Rev. A* 40, 3230 (1989).
- [30] B. Hafizi, A. Ting, P. Sprangle, and R. F. Hubbard, *Phys. Rev. E* 62, 4120 (2000).
- [31] D. J. Spence, A. Butler, and S. M. Hooker, *J. Opt. Soc. Am. B* 20, 138 (2003).
- [32] C.G. Durfee and H. M. Milchberg, *Phys. Rev. Lett.* 71, 2049 (1993).
- [33] H. M. Milchberg, T. R. Clark, C. G. Durfee, T. M. Antonsen, and P. Mora, *Phys. Plasmas* 3, 2149 (1996).
- [34] S. J. Yoon, A. J. Goers, G. Hine, J. Magill, and H. M. Milchberg, *Optics Express* 21, 15878 (2013).

- [35] D. Strickland and G. Mourou, *Opt. Commun.* 56, 219 (1985).
- [36] http://en.wikipedia.org/wiki/Chirped_pulse_amplification#cite_note-3.
- [37] N.C. Pathak, G. Bussolino, C.A. Cecchetti, A. Giulietti, D. Giulietti, P. Köster, T. Levato, L. Labate, L.A. Gizzi, *Nuclear Instruments and Methods in Physics Research A* 680, 103 (2012).
- [38] W. Zhu, J. P. Palastro, and T. M. Antonsen, *Phys. Plasmas* 19, 033105 (2012).
- [39] C. D. Decker, W. B. Mori, and T. Katsouleas, *Phys. Rev. E* 50, R3338 (1994).
- [40] P. Sprangle, E. Esarey, and A. Ting, *Phys. Rev. A* 41, 4463 (1990).
- [41] B. A. Shadwick, C. B. Schroeder, and E. Esarey, *Phys. Plasmas* 16, 056704 (2009).
- [42] M. Tzoufras, Ph.D. Thesis, UCLA, 2008.
- [43] C. G. R. Geddes, C. Tóth, J. van Tilborg, E. Esarey, C. B. Schroeder, D. Bruhwiler, C. Nieter, J. Cary, and W. P. Leemans, *Phys. Plasmas* 12, 056709 (2005).
- [44] J. Faure, Y. Glinec, G. Gallot, and V. Malka, *Phys. Plasmas* 13, 056706 (2006).
- [45] C. D. Murphy, R. Trines, J. Vieira, A.J.W.Reitsma, R.Bingham, J.L.Collier, E.J.Divall, P.S.Foster, C.J.Hooker, A.J.Langley, P.A.Norreys, R.A.Fonseca, F.Fiuza, L.O.Silva, J.T.Mendonca, W.B.Mori, J.G.Gallacher, R.Viskup, D.A.Jaroszynski, S.P.D.Mangles, A.G.R.Thomas, K.Krushelnick, Z.Najmudin, *Phys. Plasmas* 13, 033108 (2006).
- [46] T. P. Rowlands-Rees, C. Kamperidis, S. Kneip, A. J. Gonsalves, S. P. D. Mangles, J. G. Gallacher, E. Brunetti, T. Ibbotson, C. D. Murphy, P. S. Foster, M. J. Streeter, F. Budde, P. A. Norreys, D. A. Jaroszynski, K. Krushelnick, Z. Najmudin, and S. M. Hooker, *Phys. Rev. Lett.* 100, 105005 (2008).
- [47] C.-H. Pai, Y.-Y. Chang, L.-C. Ha, Z.-H. Xie, M.-W. Lin, J.-M., Lin, Y.-M. Chen, G. Tsaur, H.-H. Chu, S.-H. Chen, J.-Y. Lin, J. Wang, and S.-Y. Chen, *Phys. Rev. A* 82, 063804 (2010).
- [48] R. M. Hochstrasser, *Proc. Natl. Acad. Sci. USA* 104, 14190 (2007).
- [49] C. K. Birdsall, A. B. Langdon, *Plasma Physics via Computer Simulation* (McGraw-Hill 1985).
- [50] John M. Dawson, *Rev. Mod. Phys.* 55, 403–447 (1983).
- [51] C. A. Coverdale, C. B. Darrow, C. D. Decker, W. B. Mori, K. Tzeng, K. A. Marsh, C. E. Clayton, and C. Joshi, *Phys. Rev. Lett.* 74, 4659 (1995).
- [52] C. D. Decker, W. B. Mori, K. Tzeng, and T. Katsouleas, *Phys. Plasmas* 3, 2047 (1996).
- [53] S. V. Bulanov, I. N. Inovenkov, V. I. Kirsanov, N. M. Naumova, and A. S. Sakharov, *Phys. Fluids B* 4, 1935 (1992).
- [54] S. V. Bulanov, F. Pegoraro, and A. M. Pukhov, *Phys. Rev. Lett.* 74, 710 (1995).

- [55] C. Benedetti, A. Sgattoni, G. Turchetti, P. Londrillo, IEEE Transactions on Plasma Science, 36(4), 1790 (2008).
- [56] K.J. Bowers, B.J. Albright, L. Yin, B. Bergen, T.J.T. Kwan, Physics of Plasmas 15, 055703 (2008).
- [57] H. Burau, R. Widera, W. Hönig, G. Juckeland, A. Debus, T. Kluge, U. Schramm, T. E. Cowan, R. Sauerbrey, and M. Bussmann, IEEE Transactions on Plasma Science, 38(10), 2831 (2010).
- [58] Kong, Huang, Ren, Decyk, J. Comput. Phys. 230, 4 (2011).
- [59] P. Abreu, R. A. Fonseca, J. M. Pereira, and L. O. Silva, IEEE Transactions on Plasma Science, 39(2), 675 (2011).
- [60] R. A. Fonseca, L. O. Silva, F. S. Tsung, V. K. Decyk, W. Lu, C. Ren, W. B. Mori, S. Deng, S. Lee, T. Katsouleas, and J. C. Adam, *OSIRIS: A Three-Dimensional, Fully Relativistic Particle in Cell Code for Modeling Plasma Based Accelerators*, (Springer Berlin Heidelberg, 2002), pp. 342
- [61] R. G. Hemker, Ph.D. thesis, UCLA (2000).
- [62] K. Amyx, “GPU-Accelerated 3-D electromagnetic particle-in-cell implementations in VORPAL,” Proc. of the GPU Technology Conference, San Jose, California (2012); http://developer.download.nvidia.com/GTC/PDF/GTC2012/Posters/P0512_GPU_3D_EMPI_C_in_VORPAL_Amyx.pdf.
- [63] Francesco Rossi, Pasquale Londrillo, Andrea Sgattoni, Stefano Sinigardi, and Giorgio Turchetti, “Towards Robust Algorithms for Current Deposition and Dynamic Load-balancing in a GPU Particle In Cell Code”, AIP Conf. Proc. 1507, 184 (2012).
- [64] J.-L. Vay, C. G. R. Geddes, E. Esarey, C. B. Schroeder, W. P. Leemans, E. Cormier-Michel, and D. P. Grote, Phys. Plasmas 18, 123103 (2011).
- [65] D. F. Grodon, W. B. Mori, and T. M. Antonsen, IEEE Trans. Plasma Science 28, 1135 – 1143 (2000).
- [66] B. M. Cowan, D. L. Bruhwiler, E. Cormier-Michel, E. Esarey, C. G. R. Geddes, P. Messmer, K. M. Paul, J. Comput. Phys. 230, 61 (2011).
- [67] S. Morshed, Ph.D. thesis, University of Maryland College Park (2009).
- [68] C. Huang and V. K. Decyk and C. Ren and M. Zhou and W. Lu and W. B. Mori and J. H. Cooley and T. M. Antonsen and T. Katsouleas, J. Comput. Phys. 217 658 (2006).
- [69] M. Kolesik and J. V. Moloney, PHYSICAL REVIEW E 70, 036604 (2004).
- [70] R. W. Ziolkowski and J. B. Judkins, J. Opt. Soc. Am. B 10, 186 (1993).
- [71] K.S. Yee, IEEE Trans. Antennas Propagat. 14 302 (1966).

- [72] R. Courant, K. Friedrichs, H. Lewy, *Mathematische Annalen* (in German) 100 (1) 32–74 (1928).
- [73] R. Courant, K. Friedrichs, H. Lewy, *On the partial difference equations of mathematical physics*, AEC Research and Development Report, NYO-7689, (New York: AEC Computing and Applied Mathematics Centre – Courant Institute of Mathematical Sciences, September 1956), pp. V + 76.
- [74] Andrew D. Greenwood, Keith L. Cartwright, John W. Luginsland, Ernest A. Baca, *J. Comput. Phys.* 201 665 (2004).
- [75] J. Schreiber, C. Bellei, S.P.D. Mangles, C. Kamperidis, S. Kneip, S.R. Nagel, C.A.J. Palmer, P.P. Rajeev, M. J. V. Streeter, Z. Najmudin, *Phys. Rev. Lett.* 105, 235003 (2010).
- [76] <http://www.scarpaz.com/Attic/Documents/TheWignerDistribution.pdf>.
- [77] S. Mallat, *A Wavelet Tour of Signal Processing*, (Academic Press, London, 1998), pp. 104113.
- [78] F. S. Tsung, C. Ren, L. O. Silva, W. B. Mori, and T. Katsouleas, *Proc. Natl. Acad. Sci. USA* 99, 29 (2002).
- [79] J. Faure, Y. Glinec, J. J. Santos, F. Ewald, J.-P. Rousseau, S. Kiselev, A. Pukhov, T. Hosokai, and V. Malka, *Phys. Rev. Lett.* 95, 205003 (2005).
- [80] D. F. Gordon, B. Hafizi, R. F. Hubbard, J. R. Penano, P. Sprangle, and A. Ting, *Phys. Rev. Lett.* 90, 215001 (2003).
- [81] T. M. Antonsen, J. Palastro, and H. M. Milchberg, *Phys. Plasmas* 14, 033107 (2007).
- [82] W. Zhu, J. P. Palastro, and T. M. Antonsen, “Studies of spectral modification and extensions of the paraxial equation in laser wakefield simulations”, *AIP Conf. Proc.* 1507, 357-362 (2012).
- [83] T. R. Clark, and H. M. Milchberg, *Phys. Rev. E* 61, 1954 (2000).